

POLITECNICO DI TORINO

DEPARTMENT OF MECHANICAL AND AEROSPACE ENGINEERING

Master Degree in Biomedical Engineering



Innovative Oxygen Saturation Detection

Supervisor

Prof. Gabriella OLMO

Co-supervisor

Ing. Alessandro GUMIERO

Candidate

Annagrazia PEDICINI

ACADEMIC YEAR 2018-2019

Summary

The interest in wearable and portable devices is becoming increasingly important. Home-monitoring, and consequent reduction of hospitalization, is the most important telemedicine aim. In this context, pulse oximeter can be integrated in monitoring system, for peripheral oxygen saturation (SpO_2) measurement. It is composed of two LEDs (red and IR) and a photodetector, applied in transmittance or reflectance configuration on the finger, ear or forehead. The selected wavelengths allow to perceive the hemoglobin concentration in the peripheral circulation, because the large absorption of the deoxyhemoglobin (Hb) and oxyhemoglobin (HbO_2) molecules in the blood. The acquired signal is the photoplethysmographic signal (PPG), resulting from the light/tissue interaction. This thesis presents an innovative pulse oximeter, based on the utilization of one white LED and the multispectral sensor, the Rainbow, an ambient light sensor (ALS), sensitive to the visible spectrum. Particularly, the present work investigates two version of the Rainbow sensor, firstly the VD6281 and then the VD6282. This approach simplifies the hardware system. The possibility to utilized the green and red wavelengths for the SpO_2 measurement is analysed. Furthermore, the signal is less affected to motion artifact and to scattering effects of the surrounding tissues. The first step of the project is the mathematical model selection. The SpO_2 measurements are based on the Lambert Beer equation, because the absorption nature of the PPG signal. The effective molar extinction coefficients are found for the optical system, considering the real nature of the normalized spectral characteristics of the LED and the Rainbow. Subsequently, the PPG signal at the red and green λ are acquired and processed. The developed algorithm effectuates the peaks and minima detection for the determination of the R ratio between the alternate and continuous component of the signal, extracted by filtering operation. The R ratio is necessary for the determination of the SpO_2 . Than the final values of the SpO_2 are evaluated by comparing the Rainbow results with the Onyx pulse oximeter, used as reference for the present work. The SpO_2 is evaluate with the Lambert-Beer equation and the regression analysis. The Mean Relative Error (MRE) of the final Lambert Beer equation is relatively high for the SpO_2 assessment (i.e. MRE of about 10%). While, with the regression analysis the MRE is of about 1-2%, but the system result less sensitive to lower values of SpO_2 . Also the HR is evaluated considering the peaks detected from the red and green signals, with final MRE of about 5%.

Contents

Acronyms	v
I Background	1
Project Aim	2
1 Introduction	4
1.1 Telehealth and telemedicine	5
1.2 Oxygen transport in the body	7
1.2.1 Circulatory System	7
1.2.2 Respiratory System	9
1.2.3 Hemoglobin fundamentals	10
1.3 Photoplethysmography	12
1.3.1 Photoplethysmograph generalities	12
1.3.2 Photoplethysmography waveform	15
2 Pulse oximetry	19
2.1 Physical characteristics	19
2.2 Pulse oximeter physical principles	22
2.2.1 Lambert-Beer Law	22
2.2.2 Ratio of ratios	23
2.2.3 Peripheral oxygen saturation	25
2.3 Wavelength selection	27
2.3.1 Hemoglobin absorption properties	27
2.3.2 Skin absorbing properties	29
2.3.3 LEDs characteristics	31
2.4 Instrument calibration	32
2.4.1 Instrument calibration procedure	33
2.4.2 Calibration-free methodologies	34
2.5 Clinical applications	35

2.5.1	Perfusion Index	35
2.5.2	Pleth Variability Index	36
2.5.3	Respiration Rate	36
2.6	Pulse oximeter vs CO-oximeter	37
2.7	State of the art	39
2.7.1	Masimo Signal Extraction Technology - SET	40
2.7.2	Vyntus Walk Mobile Exercise Testing	42
2.7.3	Nonin: Onyx II 9560	43
2.7.4	Philips pulse oximeter	45
2.7.5	Garmin: Fenix 5/5S/5X Plus	46
2.7.6	Pulse oximeter on the market contest	46
II	Materials and Methods	48
3	Hardware System	49
3.1	STM32 Open Development Environment	50
3.2	Multispectral Sensors	52
3.2.1	VD6281	53
3.2.2	VD6282	54
3.3	Employed LEDs	54
3.3.1	LM231A-2323 Middle Power LED	55
3.3.2	VSMF4720-High Speed Infrared Emitting Diode	55
4	Experimental Setup	57
4.1	Oxygen Saturation Experiments	57
4.2	VD6281 Graphical User Interface	58
4.3	BT OnyxII9560 Client	59
5	Developed Algorithm	61
5.1	Pre-processing	64
5.2	Extinction Coefficient Identification	66
5.2.1	VD6282 extinction coefficients evaluation	71
5.3	Filter Design	72
5.4	Peaks and minima detection	77
5.5	Oxygen Saturation and Heart Rate estimation	82
5.6	VD6281 and VD6282 Calibration	83

III Results	86
6 Statistical Assessment	87
6.1 Regression analysis	87
6.2 Percentage error and the relative accuracy	88
6.3 Peaks and minimums validation	89
7 SpO₂ Measurements	90
7.1 Extinction Coefficients Interpolation	90
7.1.1 Normalized Spectral Intensity interpolation	91
7.1.2 Hemoglobin spectra interpolation	94
7.2 Offset Correction and Regression Analysis	96
7.2.1 Offset correction	97
7.2.2 Regression Analysis	102
8 HR Measurements	109
IV Conclusions & Future Works	114
Bibliography	118

Acronyms

6MWT	Six-Minute Walk Test
A	Unscattered Absorbance
AC	Alternating Component
ALS	Ambient Light Sensor
BPF	Band Pass Filter
BGA	Ball Grid Array
CO₂	Carbon Dioxide
COHb	Carboxyhemoglobin
CODP	Chronic Obstructive Pulmonary Disease
DC	Continuous Component
ECG	Electrocardiogram
FN	False Negative
FP	False Positive
FDA	Food and Drug Administration
FIR	Finite Impulse Response
GUI	Graphical User Interface
GPRS	General Packet Radio Service
GSM	Global System for Mobile
HF	High Frequency Power

HbO₂	Oxyhemoglobin
Hb	Deoxyhemoglobin
HRV	Heart Rate Variability
HSE	Hardware Security Module
IR	Infrared
IIR	Infinite Impulse Response
LF	Low Frequency Power
LPF	Low Pass Filter
MF	Median Frequency Power
metHb	Methemoglobin
O₂	Oxygen Molecules
PC	Personal Computer
PI	Perfusion Index
PO	Pulse Oximeter
PPG	Photoplethysmographic signal
PPV	Positive Predicted Value
PVI	Pleth Variability Index
pO₂	Partial oxygen pressure
R	Ratio of ratios
RR	Respiration Rate
SaO₂	Percutaneous oxygen saturation, CO-oximeter
SMPS	Switched-mode Power Supply
SMS	Short Messaging Service
SpO₂	Peripheral Oxygen Saturation, Pulse oximeter
STM32 ODE	STM32 Open Development Environment

T	Transmittance
tHb	Total hemoglobin
TN	True Negative
TP	True Positive

Part I

Background

Project Aim

The aim of this project is to examine the capability of the sensor **VD6281** to evaluate the SpO₂ and the HR, in real-time and non-invasively.

Nowadays, the SpO₂ evaluations are mostly employed by transmission pulse oximeter, photoplethysmography application that works with the red and the IR LEDs. Each LEDs emit a light beam that passes through the irradiated tissues, interacts with these latter and is partly absorbed. The residual transmitted rays are collected by a photodiode, opposite to the light beams direction. In this way, the PPG signal is obtained and it allows to estimate the SpO₂.

The measurements are essential in the clinical environment to trace oxygen losses, in case of severe cardiorespiratory diseases or to verify the anaesthetic efficacy. Commercial pulse oximeter are hand-held devices or probes applied to the finger, ear or forehead, utilized generally in the operating room and during the patients hospitalization. All these devices have the CE marking and are Food and Drug Administration (FDA) approved.

Most recent pulse oximeters are able to remotely send the SpO₂ values to tablets or smartphones, in real-time. In this way, the clinicians can immediately recognize dangerous situations.

Another important advancement could be to incorporate the SpO₂ estimation in wearable devices (e.g. smartwatch), as sleep monitoring parameter or to continuously monitor the blood oxygen concentration, during high altitude excursion. The data, indeed, is the only one not yet detected by wearable sensors, due to the not reliability of the estimated SpO₂ values. Specifically, the parameter is influenced by the motion artifact and it is difficult to incorporate on this type of devices, due to the transmission probes typology.

The present work wants to determine the possibility to obtain a reflective pulse oximeter, easy to incorporate in a smartwatch, using the sensor **VD6281**. In detail, this work is a preliminary study to understand if the measuries of SpO₂ with this new type of photodiode is trustworthy. The employed pulse oximeter is composed by the **VD6281** photodiode, provided by *STMicroelectronics*, and the white led **LM231A**. The innovation of this work is the utilization of a single LED to estimate the SpO₂, simplifying the hardware and the software necessary to design a typical pulse oximeter.

The VD6281 is an ambient light sensor, which accurately distinguishes the visible spectrum (RGB), the infrared and the UV wavelengths. In this manner, it can perceive wavelengths from 350 to 1050 nm. The white led covers the wavelengths of interest for the calculation of the SpO₂. The photodiode is characterized by 6 channels (red, green, blue, IR, UV and clear) that can be tracked contemporary. To maximize both the capabilities of the sensor and the absorbing properties of the tissues, the chosen wavelengths are green and red. Thus, the white LED can be used because it cover only the visible spectrum. The issues encountered in the work will be analysed and discussed throughout this report. The algorithm has been developed to estimate the value of the SpO₂ and the HR in real-time. As a final step, the *Rainbow PO* has been tested and compared with the *Onyx* device, i.e. transmittance finger pulse oximeter which uses red and infrared wavelengths.

Chapter 1

Introduction

At present, medical devices must fulfill essential requirements and are projected towards the very sophisticated technologies. In particular, the most important aspect is acquiring physiological parameters in *real-time* and *non-invasively*.

In this field, a very useful tool is *telemedicine*, which can connect health care with communication networks.

Quoting to Abo-Zahhad et al. [1]:

The term telemedicine refers to the utilization of telecommunication technology for medical diagnosis, treatment, and patient care.

Telemedicine systems can be classified on the basis of the available data:

- **real-time:** data are immediately accessible to the server, after the detection;
- **store-and-forward:** data are firstly collected and thereafter processed and made.

Thus, a telemedicine network is a remote monitoring system able to:

- acquire physiological parameters continuously or during the daily activity of the patient;
- inform the specialist, connected to the apparatus, about the health condition of the subject, especially in dangerous situations.

The network makes use of a set of wearable sensors, connected to each other by means of the *Wireless Body Area Network*: in this configuration, detectors may be incorporated in the clothes of the patients [1].

Therefore, it is not necessary for the patient to remain in the medical center, since these systems can be used at home, without the assistance of hospital staff [2].

For instance, the **peripheral oxygen saturation** is one of the parameters the sensors are able to detect.

This quantity can be measured by the pulse oximeter, a non-invasive device employed in ambulatory. For this purpose, the considered physical principles are the light absorption properties of the **oxyhemoglobin** and the **deoxyhemoglobin** in the blood flow. The percentage of oxygen dissolved in the blood is obtained from these interactions.

More accurate results can be acquired with an invasive approach: a blood sample is extracted from the patient, examined through a gas analyser and the value of the **percutaneous oxygen saturation** (SaO_2) is estimated. However, this is more troublesome than the investigation of SpO_2 , since it does not enable continuous monitoring and it is also more painful for the patient (blood samples are usually collected using catheters or needles). In the neonatal field, this process is even dangerous for the infants, who could suffer from blood losses. [3].

Elsharydah et al [4] highlight the relevance of monitoring dissolved gases. In fact, it is essential to keep track of:

- the gas exchange, mostly for critically ill patients;
- the anaesthesia release, associated to peripheral blood flow;
- cases of hypoxia or hypoxemia.

1.1 Telehealth and telemedicine

As mentioned by S. Palanivel Rajan [5], *Telehealth* encompasses a wide-ranging area of disciplines, it is a recent field of study and in rapid development.

Thanks to telecommunications, it is possible to transfer health parameters and notes about therapies among different medical centres, situated both in far or nearby places [6].

Telemedicine is a specific telehealth exploitation. The most benefit introduced by telemedicine is real time monitoring, as it is feasible to install sensors both on the patients' body and at home, which continuously keep track of their vital parameters. Consequently, the quality life of the patients with cronic disease (i.e. diabetes, cardiovascular disorders, respiratory pathology) is enhanced [7].

A major consequence is the considerable decrease of the hospitalisation rate, for the reason that it is not necessary for the patient to remain in the medical center.

In addition, telemedicine systems are commonly employed not only to keep fragile patients under observation, but also by healthy subject to sustain a healthful lifestyle.

There are distinctive features that a telemonitoring system must exhibit [8]:

- the utilised devices must be tiny and consume limited power;
- the implemented network must be low cost and should be as far as possible user friendly;

- the apparatus must have fundamental elements to permit wireless communication, e.g. bluetooth, Global System for Mobile (GSM), 3G, 4G and 5G.

Some of the quantities measured by a telemedicine network are SpO₂, Heart Rate (HR), Respiratory Rate (RR) and blood pressure.

Telemedicine becomes more and more indispensable nowadays in various clinical environments. Representative circumstances underlining the importance of telemedicine systems are reported below.

1. Wireless sensors and webcam inside the ambulances communicate the emergencies, providing to the clinicians in the hospitals with all vital parameters at once. In this case, the tools allow to identify potential severe injury without delay. Most advanced vehicles are equipped with live cam, remotely controlled by the doctor in the medical centre. In this way, it is possible to decrease the critical time to take decisions and to prepare the ambulatory for the incoming patients.
2. The home of the patients can be equipped by telemonitoring networks in which the patient is supervised remotely by the medical staff. The subject is provided with the *Wireless Body Area Network*, several sensors connected to each other to gather biological parameters and send alert messages to all involved people. For example, if a suspected HR is identified by the sensing elements, the system alerts the hospital. At first, a Short Messaging Service (SMS) will be created by the Microcontroller unit and it will enclose the unusual heart frequency interval and the Electrocardiogram (ECG). Finally, the physician will decide the actions to take for the patient health conditions.
3. The possibility to have a *teleconsult* among several disease specialists that can exchange data from the simplest signals, to complex images, to have a better feedback on the therapy.

Figure 1.1 represents the model realized by M. Abo-Zahhad et al. [1]. It is formed of 4 units:

1. **Mobile-care unit:** wearable biosensors are placed on the patients. They acquire physiological parameters, i.e. ECG, HR, SpO₂. A mobile care unit is equipped also with the processing module that computes the final data to send to the communication module.
2. **Data communication networks:** the system can work in *store-and-forward* or *real-time* mode. In the first case, data are transmitted to the remote server using internet. In the case of unusual values of the parameters, the real-time modality is activated and they are forwarded to the remote server, for example, by GSM/GPRS.

3. **Remote server & Management/monitoring units:** data are stored in the server that is available to caregivers and doctors, using the appropriate diagnostic application. At this point, the physician can decide to alert the patient family, the ambulance or the caregiver.

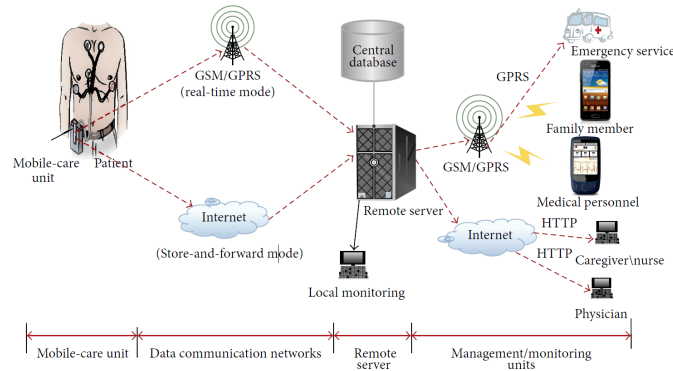
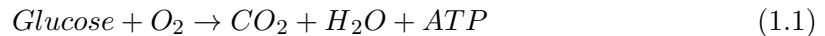


Figure 1.1: Example of telemedicine network [1].

1.2 Oxygen transport in the body

Oxygen (O_2) is a central constituent for cell survival, hence it is important to track the O_2 quantity in the tissues. The most common instrument for clinical application is the pulse oximeter, as it is non-invasive and easy to operate.

O_2 release and transport is controlled by respiratory and circulatory systems [9]. Oxygen molecules reach the cells for *cellular respiration*. This one initiates a series of chemical reactions leading to the breaking of glucose bonds. As reported by Clark in [9], the decomposition of these complex molecules generates energy in the form of **ATP** molecules, used for all metabolic reactions:



In the current chapter, circulatory and respiratory systems will be described.

1.2.1 Circulatory System

Cardiovascular system comprises the cardiac pump (i.e. heart) and the vascular conducts (i.e. blood vessels). The blood flow travels inside the vessels and is pumped throughout the body. Because of their transport function, heart and vessels are stated as *circulatory system*. The exchange among tissues of respiratory gases, nutrients, heat and so on is possible through the blood [10]. In figure 1.2, the pumping mechanism is described. This

process is carried out by the heart and leads to blood oxygenation and deoxygenation. It is possible to distinguish between [9, 11]:

1. **Pulmonary circulation:** in the right ventricle, deoxygenated blood is transported to the lungs through the pulmonary artery. In the lungs, the carbon dioxide (CO_2) is released to the pulmonary alveoli via the capillaries. At this point, blood is oxygenated because the O_2 molecules are released inside it.
2. **Systemic circulation:** the oxygenated blood goes back to the heart, in the left atrium through the pulmonary veins. The bloodstream proceeds to the left ventricle and it is ejected into the entire system, from the heart to the tissues. After the interaction between tissues and blood, this one is deoxygenated and comes back to the right atrium.

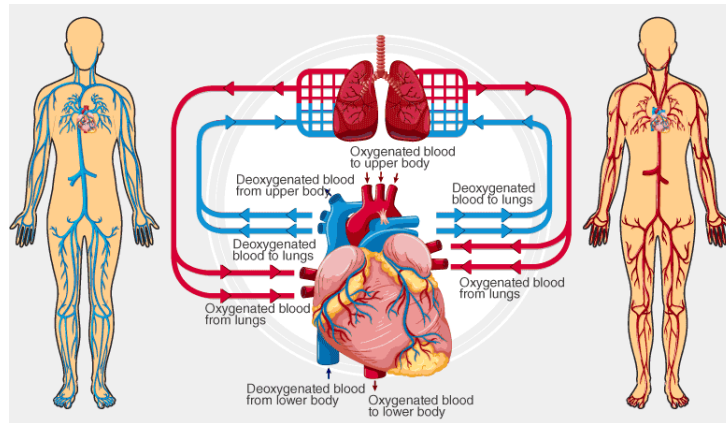


Figure 1.2: Circulatory Systems. The pulmonary system represented in blue, the systemic circulation represented in red [12].

Systemic and Pulmonary circulations are realized during the **cardiac cycle**, composed of a relaxation and a contraction phases, named **diastole** and **systole** respectively. During the two phases, first blood goes inside the atria and ventricles, then it leaves them at the end of the cycle. The cardiac cycle has a duration of about 0.8 s. Briefly, it is formed of the following consecutive steps:

- the *diastolic phase*, of about 0.4 s. Myocardium is relaxed, atrioventricular valves are open and blood enters spontaneously into the atria and ventricles;
- the *atrial systole*, of about 0.1 s. Atria empty out completely, pushing the blood to the ventricles still in diastolic phase;
- the *ventricular systole*, of about 0.3 s. Pressure level in the ventricles becomes very high and this leads to the ejection of blood into the aorta and the pulmonary artery.

During the ventricular systole, the atria are in diastole and at the end of the blood expulsion from the ventricles, the cardiac cycle begins again [13].

The HR is defined as the number of heartbeats per minute (bpm). The value of HR depends of several factors: age, air temperature, weight, individual conditions (i.e. at rest or in motion), possible cardiovascular diseases. However, the normal range of HR in adults is about 60 - 100 bpm depending on the physical condition of the subject, while for children (age 6 - 15) the normal range is about 70 - 100 bpm [14].

1.2.2 Respiratory System

The respiratory system allows the delivery of the O_2 to the whole body together with the expulsion of CO_2 . It is composed of: nasal duct, pharynx, larynx, trachea, bronchi and lungs [15].

The respiration process begins from the **nose**: the air is filtrated by cilia, then heated and humidified. Subsequently, the air goes into the **larynx** that is the common path to both the fluxes of air and food. In particular, the epiglottis blocks the passage of the food to the trachea. Afterwards, the air passes trough the **trachea**, made of a series of cartilage rings with the aim of filtering and transporting it. Trachea branches into two **bronchi**, each leading to the lungs. Bronchi also split to become **bronchioles**. Lastly, the bronchioles end in clusters defined **alveoli**, made of a very thin capillary tissue to facilitate the swap of gases.

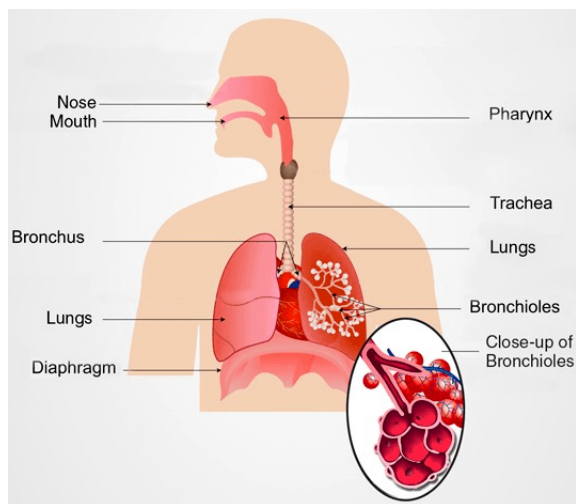


Figure 1.3: Respiratory system components [16].

The *ventilation process* is the diffusion principle whereby gases are transported. Due to the ventilation, O_2 molecules move from the area with higher pressure to the one with lower pressure. Ventilation begins with the respiratory neuron activation in the brain,

followed by the motoneurons activation in the spinal cord [9]. The electrical pathway of neurons activates the respiratory muscles: diaphragm and intercostal muscles.

The ventilation is a mechanical process that allows the continuous renewal of the air present in the lungs through the alternation of inhalations and exhalations [17]. Respiratory muscles are involved in two respiration phases [9, 15]:

1. while **inhaling**, the diaphragm contracts and intercostal muscles expands. Intrapleural pressure is negative. In this way, the air flux enters the lungs because the atmospheric pressure is higher than the internal one;
2. while **exhaling**, the intercostal muscles contracts and the diaphragm expands. Intrapleural pressure is positive. In this case, air flux leaves the lungs, considering that the pressure inside the chest is higher than the atmospheric one.

1.2.3 Hemoglobin fundamentals

As only a small part of O_2 can remain dissolved in the blood, these molecules are bound to several proteins called *breathing pigments*. They are able to lead oxygen in the blood flow and to release it in the cells [17].

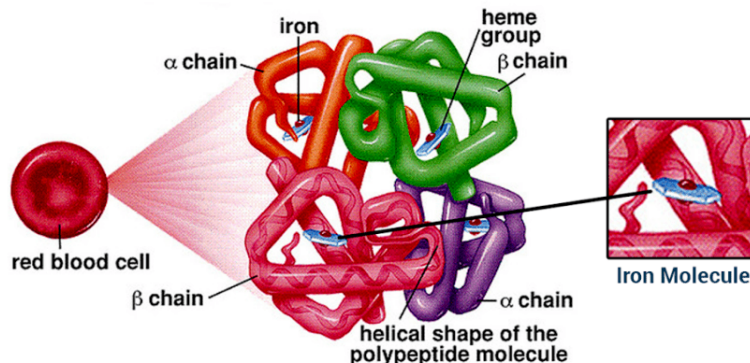


Figure 1.4: Hemoglobin structure and components [18].

Hemoglobin is formed by 4 chains of amino acids with 4 *heme groups* at the centre of each polypeptide chain [17]. The heme groups contain iron atoms capable to capture oxygen. When all heme groups are occupied, hemoglobin is defined as **saturated**.

Oxygen quantity in the blood is related to O_2 concentration, saturated hemoglobin and *cardiac output*. Cardiac output is the entire blood volume ejected in one minute by the circulatory system [19].

As reported from Konica Minolta Sensing [19], considering saturated hemoglobin, since

100 ml of blood includes about 15 g of hemoglobin, each gram of hemoglobin can contain 1,39 ml of oxygen. Thus, the quantity of oxygen in 100 ml of blood is about 20,4 ml.

Lastly, the tendency of oxygen to bind to the hemoglobin depends on its partial pressure [17]. In figure 1.5, dissociation curves are presented, which represent the relation between the partial oxygen pressure (pO_2) and the percentage of the saturated hemoglobin in the blood [9]. The factors influencing the shape of the curves are: pH, temperature and percentage of CO_2 in the blood. For example, pH increase, decrease of CO_2 percentage and temperature, leads to the dissociation curves moving on the left. This behavior improves the SpO_2 [9].

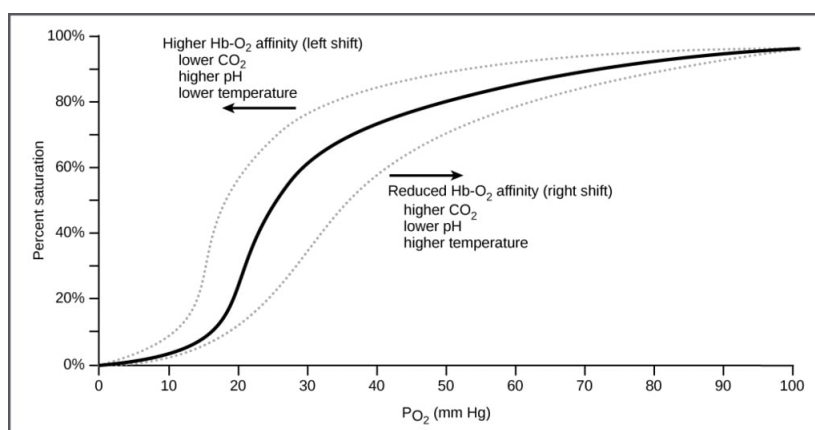


Figure 1.5: Oxyhemoglobin dissociation curves [20].

From figure 1.5, it can be understood that the lower the pO_2 is, the higher is the capability of hemoglobin to incorporate oxygen. The fetus dissociation curves are shifted to the left of the mother's ones [9].

To conclude, in addition to the measurement of SpO_2 , oxygen in the blood is also traced by calculating other indices [9]:

- Oxygen delivery index (DiO_2), to determine the oxygen quantity made available to the tissues. Normal values are approximately in the range $550 - 650 \frac{mL}{minm^2}$;
- Oxygen consumption, to evaluate the oxygen actually dispersed in the tissues. Normal values are about $115 - 165 \frac{mL}{minm^2}$, therefore the total amount of oxygen present in the tissue is not entirely used.

1.3 Photoplethysmography

Photoplethysmographic signal is collected by non-invasive optical procedure, since it is recorded in a certain area on the dermis. In the last decade, PPG signal has increasingly been taken under consideration given the simplicity and the non-invasiveness in the acquisition mode and the recent development of wearable and portable devices [21].

The term stems from the Greek "*plethysmos*", translated as "*get larger*". Indeed, PPG signal owns *specific morphological features*, depending on the signal collection area and the assessment accuracy, blood volume changes are perceived [22].

Photoplethysmographic signal is widely used by many health instruments on the market to estimate SpO₂, blood pressure, heart output, HR and RR. It is possible to recognize specific peripheral vascular diseases thanks to the latest processing methods.

In the current chapter, details about the PPG analysis system are provided, along with the morphological characteristics of the signal and the major clinical applications.

1.3.1 Photoplethysmograph generalities

A non-intrusive signal gathering system should be: affordable, dependable, secure, repeatable and easy to implement. The photoplethysmograph is comparable to an ideal signal picking system [23].

PPG signal was first discovered by Hertzman in the Department of Physiology at St. Louis University School of Medicine, St. Louis, MO.

Hertzman et al. analysed the extraction procedure to monitor the blood volume variations. They made use of a reflective photoplethysmograph on a finger to evaluate the variance of the blood quantity in the course of the Valsalva manoeuvre. Briefly, they examined the vasodilatory action, dividing the two PPG components (i.e. alternate and continuous) and underlined the main causes leading to low signal quality, i.e. the physical contact between the sensor and the skin [21].

A photoplethysmograph relies on the absorption optical principle of light, also known as Lambert-beer Law, reported in detail in paragraph 2.2.

The instrumentation consists of light sources (usually LEDs) and a photodetector, extremely precise at the involved wavelength. Conventionally, the light beam sensors are realized with photodetectors in silicon, but different types of sensors can also be employed, such as photocells and phototransistors [24].

The signal is created thanks to the interaction between the light generated by the LED and the tissues. If the emitted light is fired in the monitored skin area, its intensity is reduced as it is partly absorbed by the tissues. Specifically, the attenuation is modulated by the variations in blood volume, according to the cardiac cycle [23].

Consequently, the PPG signal correlates changes in light intensity with changes in blood volume inside the tissue area under observation [25].

Because of the suitable connection between light and peripheral blood flow, the device can be usually located on the finger, the forehead or the wrist. However, several researches have been realized to find out the site where the signal is better enhanced.

Clayton et al. [26] compared different types of probes (finger, nose, ear and forehead) and they established that in case of low perfusion, the forehead and the nose probes are suitable whereas in the same conditions, the ear and the finger ones can result in more elevated bias and lower accuracy.

Longmore et al. [27] investigated eight sampling sites (i.e. forehead, temple, rib cage, finger, tibia, wrist, lower back and back of neck) and made an estimation about the best position to calculate both the HR, the RR and the SpO₂ during conditions of inactivity and marching.

The conclusion of this study is that the finger is the most appropriate location to concurrently detect RR, HR and SpO₂, while the forehead is preferable to evaluate the last two parameters only.

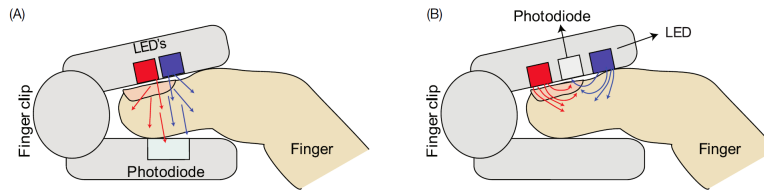


Figure 1.6: transmission (a) and reflective (b) PPG sensors [24].

In figure 1.6, two modalities of signal acquisition are schematized [24]:

- *transmission*. In this case the light is detected after the transmission through the tissue and the LEDs are on the opposite side of the photodetector. Currently, this system configuration is widely used by clinician. It is usually positioned on the subject's toe, finger or else earlobe.
- *Reflective*, where LEDs and photodetector are on the same side and they are lined up few millimeters apart. The photodetector gathers the back-diffused photons, after the interaction [28]. Due to the proximity between photodiode and LEDs, the reflective system can be implemented on any portion of the dermis. The locations of this type of probe are principally temple and forehead.

There are not substantial differences between the two acquiring methods. Optically, the problem that could arise is the uncertainty of the *path-length* of the light beams inside the

considered tissue, primarily in reflective configuration. It is correlated to the wavelengths imposed by the chosen LEDs. In fact, while in the transmissive modality the path-length is ideally the same, this cannot be verified for the reflective one [29].

Gemert van et al. [30] discovered that setting two similar wavelengths, the path-length of the light beam can be considered equal, even if it is not tabulated at the two wavelengths. This consideration is necessary to obtain the relationship that binds SpO_2 with extinction coefficients.

In either configurations, light travels through the tissues to a certain depth, interacting with them in a similar way.

There is a certain difference in signal amplitude depending on the area of the skin where the probes are placed [31].

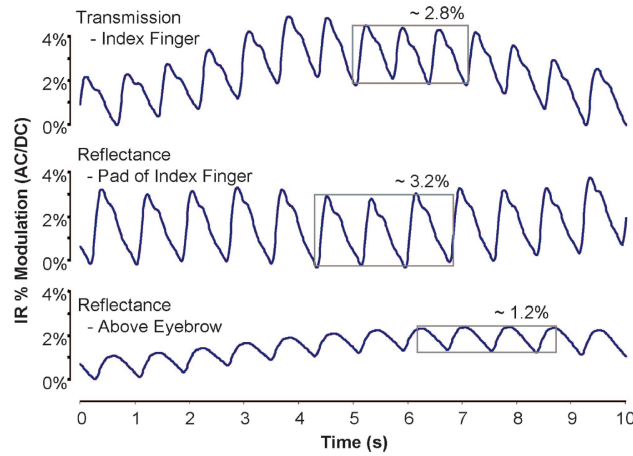


Figure 1.7: Analysis of PPG amplitudes, collecting the beams of light on different skin areas [31].

In figure 1.7, PPG signals have different amplitudes depending on the sampling site only, independently of the reciprocal orientation between LED and photodiode.

1.3.2 Photoplethysmography waveform

The pulsatile nature of the PPG signal is related to the cardiac cycle phases. The signal indeed varies as the HR. If it is correctly processed, details about peripheral circulation can be estimated.

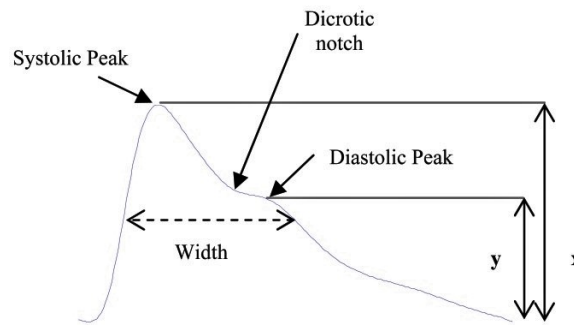


Figure 1.8: PPG signal characteristics [32].

In figure 1.8 the principal features of the signal are shown. The PPG signal follows the phases of the cardiac cycle:

- **anacrotic**, corresponding to the ventricular systole;
- **catacrotic**, corresponding to the ventricular diastole.

In the catacrotic phase, the **dicrotic notch** can be appreciated. It is always present in the signal of healthy subjects and denotes the good compliance of the arterial vessel.

The two main constituents extrapolated from the PPG signal are [21, 33]:

- **DC** component, the continuous component of the signal connected to low frequency elements, consisting of thermoregulation, pulsations of the nervous sympathetic system and respiratory frequency.
- **AC** component, the alternating component of the signal associated to the blood volume variation, during beat-to-beat heart rhythm. It is useful to analyse the efficiency of the cardiac pump and vascular compliance. The AC part is slightly overlapped to the DC component;

The alternating and continuous components of the PPG signal can be analyzed separately, obtaining detailed information about blood volume changes [23].

The signal is appropriately filtered, according to the component to be examined. Then it needs to be inverted and self-centered, before being represented on the screen of the device [22]. In both transmission and reflective acquisition modes, the PPG signal is reversed

due to the *inverse relation* between the blood volume and the intensity of light recorded on the sensor [25]. In this regard, the phases of the cardiac cycle need to be considered. In the course of the systolic phase the volume of blood increases. There are two consequences:

1. the inflow blood has a higher concentration of hemoglobin molecules and the amount of the absorbing light increases;
2. because of (1), the amount of light that reaches the sensor decreases.

In a similar way, during the diastolic phase the volume of blood decreases, the amount of hemoglobin in the blood is lower than in the previous case and the amount of light that reaches the sensor increases.

After signal reversal, the peak and minimum value of the PPG correspond correctly to the systolic peak (i.e. **anacrotic phase**) and the diastolic peak (i.e. **catacrotic phase**).

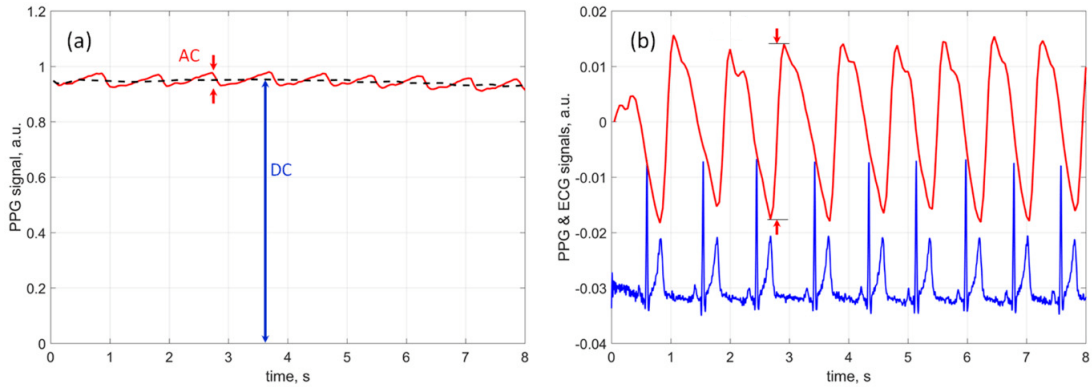


Figure 1.9: (a) PPG before the processing steps, in the non-inverted configuration (b) the processed PPG in the inverse configuration is represented in red ; the ECG waveform to compare the recurrence of the R wave with the PPG systolic peak is represented in blue [34].

In figure 1.9(b), the inverted PPG is illustrated together with the electrocardiogram signal, simultaneously recorded. It can be seen that the extracted alternating component varies like the HR, as it is synched to the R peak of the ECG [34].

The morphology of the signal is influenced by several factors [31, 23]:

1. **concentration** of the absorbing elements in the tissue under observation. It is correlated to the blood quantity in the site of interest that diminishes and rises periodically;
2. **distance** between LEDs and the photodetector and deepness of the pulsating vessel. The pulse width increases as the distance increases;

3. **spectrophotometric** properties of peripheral arterial blood at the specified wavelengths;
4. skin **temperature**;
5. **orientation** of the red blood cells in relation to the incident light beam;
6. **blood flow** at the site of interest, on which the concentration of hemoglobin depends and thus the saturation of oxygen in the blood;

The signal frequency band is between 0.04 Hz and 8 Hz, including information about the central nervous system control on the cardiovascular system. The signal spectrum can be divided into two different frequency bands: the low-frequency (LF), from 0.04 to 0.15 Hz and the high-frequency (HF), from 0.15 to 0.6 Hz [35]. The LF includes the median frequency band (MF), from 0.09 to 0.15 Hz.

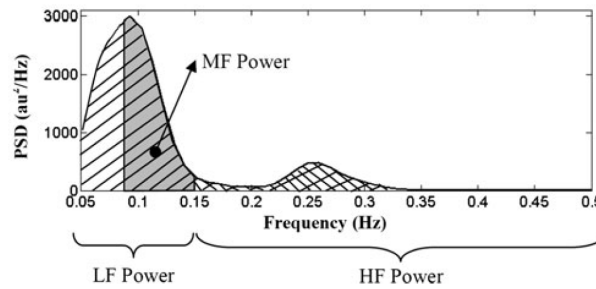


Figure 1.10: PPG power spectra frequency bands [35].

The LF power defines the peripheral circulation, regulated by the sympathetic and the parasympathetic systems, while the HF power contains information about the HR, controlled by the parasympathetic system at the respiration rate [35].

As explained above, the PPG signal consists of two components: the pulsatile component (i.e. AC) and the static component (i.e. DC) [22].

The alternating component has a frequency that depends on HR, typically equals to 1-2 Hz. Continuous component, on the other hand, has a much higher amplitude than the AC one. It is related to breathing and venous blood flow (regulated by the right atrial contraction).

Through adequate processing techniques, the single AC and DC components are obtained: the alternating component is extracted through a band-pass filter, with cut-off frequencies of about 0.1 Hz and 8 Hz, while the continuous component is extracted using a low-pass filter, with cut-off frequency of 0.01 Hz [22, 21].

PPG can be examined in time or frequency domain. In *time domain*, the estimated factors are the pulses characteristics (height, width, area and amplitude) and maximum

and minimum values. In *frequency domain*, the fast Fourier transform (i.e. the power spectrum of the signal) is calculated to attain time independence from the assumption that PPG is considered as the sum of sine and cosine [22].

Chapter 2

Pulse oximetry

Pulse oximetry is a particular clinical application of photoplethysmography. In this field, the pulse oximeter is the device employed by pulse oximetry, a non-invasive medical instrument used to acquire the percentage of the oxygen in the peripheral arterial blood, exploiting the absorbing and the transmission properties of hemoglobin molecules.

The pulse oximeter utilizes the PPG signal to estimate both the values of SpO₂ and the HR [21].

In the current chapter, the theory to correctly design pulse oximeter and clinical applications of this technology will be explained.

2.1 Physical characteristics

Chemically, oxygen saturation is indicated as the percentage of oxygenated hemoglobin with respect to the total one in arterial blood, also known as *functional oxygen saturation* [36, 37].

$$SpO_{2functional} = \frac{[HbO_2]}{[Hb] + [HbO_2]} \times 100\% \quad (2.1)$$

where, [Hb] and [HbO₂] are the concentrations of de- and oxi- hemoglobin, present in the peripheral bloodstream.

For healthy subjects, normal values of SpO₂ are in excess of 98-99%. Oxygen saturation less than 90% can denote critical respiratory conditions (known as hypoxemia), muscle fatigue, motor difficulties, mental decline and, in acute circumstances, they can lead to death [38, 39].

The SpO₂ can be also acquired by means of a non-invasive estimation, using the pulse oximeter.

The physical principle at the basis of pulse oximetry is the Lambert-Beer Law, optical principle defining the light-medium interactions.

Regarding the typical components of commercial pulse oximeter, two LEDs (i.e. red and

infrared) and a photodiode are usually used. As described in section 1.3.1, the photoplethysmograph, in this case the pulse oximeter, can be classified as transmissive and reflective. In both the modalities, LEDs alternately illuminate the detection area and then the photodiode collects the PPG signal, that incorporates the interactions among the light and the hemoglobin molecules in the blood flow. Moreover, within the site of interest and at the selected wavelengths, Hb and HbO₂ give an higher contribution on the absorption than of the closest substances.

As a consequence of the light-blood interactions, the PPG signal is thus acquired, along with the useful information associated to the incoming arterial bloodstream. Indeed, it carries a certain amount of hemoglobin, oxygenated and not, and in this way details about the oxygen concentration can be defined. [40].

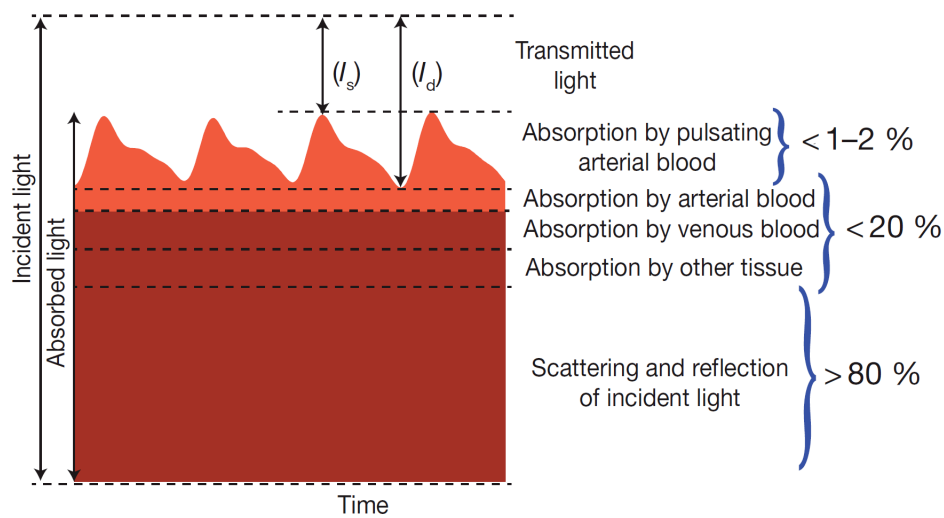


Figure 2.1: Signal characterization posterior to tissue interactions: percentages of different absorbing contributions [24].

The light intensity subsequent to the interaction varies as shown in figure 2.1, where I_s and I_d are the systolic and the diastolic peaks, respectively.

PPG continuous components are associated with tissue absorption, venous bloodstream and the continued fraction of the arterial bloodstream. The remaining portion of the arterial blood generates PPG pulsating components, which vary depending on the heart rate.

More specifically, during the left ventricular diastole, the greatest absorption contribution is given by tissues, skin pigments (e.g. melanin), bones and venous blood. During the ventricular systole, corresponding to the phase in which the blood is ejected from the left ventricle to all the peripheral tissues, the major absorption contribution is related to the flow of arterial blood that reaches the tissues [41].

Referring to figure 2.1, another important contribution is scattering, [41]. Specifically, the scattering occurs on:

- the red globule-plasma interface, evident mostly at the red wavelength (i.e. 660 nm). In this case, the scattering yields an extra of 50% on the absorption of the complete blood flow;
- tissue-bone interface, where the calibration results from the studies conducted on the finger probes are highly different from those conducted on the ear probes.

In view of the above mentioned reasons, the calibration process is required and it is achieved by comparing SpO_2 values, obtained with a pulse oximeter, with data acquired in vivo. However, clinical situation in which SpO_2 drops under 80% are very rare: in cases of extreme hypoxemia, actually, the accuracy of the PO decreases severely [41].

Commercial pulse oximeters are realized according to precise assumptions [42]:

1. pulse oximeter only reveals the presence of the HbO_2 and Hb in the blood. SpO_2 is related to the extinction coefficients of the two hemoglobin species, and the extinction coefficients in turn are related to the chosen wavelengths. Consequently, wavelengths should be properly fixed to maximize the absorption of oxygenated and deoxygenated hemoglobin. This condition occurs if the extinction coefficients are considerably different at the selected wavelength;
2. pulse oximeter exploits the pulsating nature of arterial blood. From the PPG signal, it is possible to distinguish the AC component of arterial blood and the DC component of venous blood. Therefore, the value of SpO_2 is calculated as the ratio between the two components, at the two chosen wavelengths;
3. in addition to selecting two suitable wavelengths values, it is necessary to choose the light beam intensity to direct on the site of interest. If this is adequate enough, the arterial component will be much more evident than the scattering effects due to the surrounding tissues.

2.2 Pulse oximeter physical principles

The functioning of the pulse oximeter is based on the Lambert Beer Law that allows to measure the intensity of the transmitted light, after the interaction with a medium [43]. From this theoretical model, the amount of light absorbed by the device is estimated. The principle is not valid for all the blood components, as it does not include the effects of scattering, that requires correction coefficients [44]. In the pulse oximeter application indeed, to obtain accurate results, a subsequent calibration of the instrument is necessary. Regarding sections **Ratio of ratios** and **SpO₂**, reporting the mathematical transformations of the Lambert-Beer Law, the reader is invited to consult Kennedy et al. as a reference [43].

2.2.1 Lambert-Beer Law

The Lambert-Beer Law provides the mathematical relation for calculating the amount of light transmitted through a medium under the following conditions:

- the photons interact with a homogeneous medium which contains an absorbent element;
- the light beam on the medium is monochromatic and the individual photons are parallel to each other;
- the incident light beam is equal to the sum of the amount of the transmitted light and the amount of absorbed light. Therefore, the effect of scattering in the medium is not taken into account.

Considering the previous assumptions, the amplitude of the incident ray (I_0) is attenuated when it enters into the matter, being partially absorbed. The amplitude decreases exponentially based on the travelled distance:

$$I = I_0 e^{-\epsilon(\lambda)cd} \quad (2.2)$$

Where, $\epsilon(\lambda)$ is the extinction coefficient ($L \text{ mmol}^{-1} \text{ cm}^{-1}$) of the absorbing substance inside the piece of irradiated matter, specific for the wavelength ray; c is the concentration of the absorbing substance (L); d is the path-length of the photon beam in the matter [44].

The parameter extrapolated from the Lambert-Beer Law are:

1. the transmittance,

$$T = \frac{I}{I_0} = e^{-\epsilon(\lambda)cd} \quad (2.3)$$

which is the ratio between the light intensity resulting from the transmission (I) and the initial light intensity (I_0);

2. the unscattered absorbance,

$$A = -\ln(T) = \epsilon(\lambda)cd \quad (2.4)$$

negative logarithm of (2.3). It represents the light quantity absorbed by the attenuating object inside the matter.

For $T = 1$ the medium is completely transparent to the incident light beam, which traverses the medium without any energy loss. On the other hand, for $T = 0$, the medium stops the passage of the photons and it completely absorbs them [31].

In case the medium comprises more absorbing substances, they are considered as N optical filters and T and A are calculated as:

$$T_{total} = T_1 \cdot T_2 \cdot T_3 \cdots T_N \quad (2.5)$$

$$A_{total} = \epsilon_1(\lambda)c_1d_1 + \epsilon_2(\lambda)c_2d_2 + \epsilon_3(\lambda)c_3d_3 + \cdots + \epsilon_N(\lambda)c_Nd_N \quad (2.6)$$

The quantity obtained from (2.5) is the total transmittance, equal to the product of the transmittance of each individual filter that contributes to the light attenuation [31].

The quantity obtained from (2.6) is the total absorbance, the sum of the individual absorbances [43].

2.2.2 Ratio of ratios

The relations employed by the pulse oximeter are based on the absorbance equation, deduced from the Lambert-Beer Law.

Since tissues are composed of different absorbent substances, the light can interact with each of them. Hence, the relation to consider is equation (2.6), underlining the presence of multiple materials, deemed as N optical filters [31].

The initial value of the light amplitude (I_0) cannot be determined in an accurate way. However, due to pulsating nature of arterial vessels, I_0 can be considered negligible. The path-length d of the light beam is regularly modified because the width of the vessels expand and shrink during the cardiac cycle.

The minimum value of the light intensity is the *baseline intensity* (I_B) and it is derived from (2.2).

$$I_B = I_0 e^{-\epsilon_B(\lambda)c_B d} \quad (2.7)$$

In equation (2.7), multiplying the extinction coefficient $\epsilon_B(\lambda)$ and the concentration of the

absorbent material c_B , the absorbance coefficient is obtained:

$$\alpha_B(\lambda) = \epsilon_B(\lambda)c_B \quad (2.8)$$

$\alpha_B(\lambda)$ is wavelength dependent, but this is an approximation, since the tissues are not homogeneous and the contribution of a single concentration is not present.

Considering (2.8), the I_B value is modified as:

$$I_B = I_0 e^{-\alpha_B(\lambda)d} \quad (2.9)$$

The intensity corresponding to the highest value of the pulsation is considered as the variation of the baseline value I_B . I_P is deduced by equation (2.9) and resulting as:

$$I_P = I_B e^{-\alpha_P(\lambda)\Delta d} = I_0 e^{-\alpha_B(\lambda)d - \alpha_P(\lambda)\Delta d} \quad (2.10)$$

By computing the ratio of I_P and I_B , the transmittance variation ΔT is obtained as:

$$\Delta T = \frac{I_P}{I_B} = \frac{I_0 e^{-\alpha_B(\lambda)d - \alpha_P(\lambda)\Delta d}}{I_0 e^{-\alpha_B(\lambda)d}} = e^{\alpha_P(\lambda)\Delta d} \quad (2.11)$$

As expressed above, the value of ΔT appears independent of the amplitude initial value I_0 , even though associated with the undetermined path-length Δd . Further calculations need to be made to eliminate the contribution of Δd .

The absorbance is estimated as the negative logarithm of the transmittance. To the right and left of the equation (2.11), the natural logarithm is indeed carried out as follows:

$$\Delta A = -\ln \Delta T = -\ln e^{\alpha_P(\lambda)\Delta d} = \alpha_P(\lambda)\Delta d \quad (2.12)$$

To eliminate the contribution of Δd , two different wavelengths are utilized to derive the absorbance values.

Pulse oximeter operates with red and IR wavelengths and the resulting ΔA values are:

$$\Delta A(\lambda_R) = \alpha_P(\lambda_R)\Delta d \quad (2.13)$$

$$\Delta A(\lambda_{IR}) = \alpha_P(\lambda_{IR})\Delta d \quad (2.14)$$

At this point, several considerations can be made about the path-lengths Δd , in view of the transmissive or the reflective pulse oximeter [29]. However, as explained in section 1.3.1, Δd values are approximately considered identical at the two wavelengths. In this manner, the subsequent equations can be considered valid for both configurations.

The path-length of transmitted light at the two wavelengths is assumed to be equal. The resulting ratio between the two absorbances variations is designated as ratio of ratios:

$$R = \frac{\Delta A(\lambda_R)}{\Delta A(\lambda_{IR})} = \frac{\alpha_P(\lambda_R)}{\alpha_P(\lambda_{IR})} \quad (2.15)$$

In equation (2.15), R is independent from the value of the initial light intensity and from its path-length inside the tissue. Utilizing the R value, the SpO_2 equation is found.

Considering the PPG signal, the transmittance variation is correlated to the AC component of the signal. In fact, the cardiac cycle causes a different concentration of the HbO_2 and Hb molecules in the blood. As a result, the alternated component changes regularly because the resulting interaction light/blood-flow are modified [45]. As R is the absorption ratio which in turn are the logarithm of transmittance, the ratio R can be rewritten as:

$$R = \frac{AC_R}{AC_{IR}} \quad (2.16)$$

The AC component is normalized with the respective DC component. Thus, the final R value returned by pulse oximeter is:

$$R = \frac{AC_R/DC_R}{AC_{IR}/DC_{IR}} \quad (2.17)$$

2.2.3 Peripheral oxygen saturation

As reported in paragraph 2.1, the value of SpO_2 referred to the functional hemoglobin concentrations is calculated using the equation 2.1, which relates the hemoglobin concentrations to the peripheral oxygen saturation as follow:

$$c_{HbO_2} = SpO_2(c_{HbO_2} + c_{Hb}), \quad (2.18)$$

$$c_{Hb} = (1 - SpO_2)(c_{HbO_2} + c_{Hb}) \quad (2.19)$$

Biological tissues are a mixture of absorbing materials. In this application the only ones taken into account are the two functional hemoglobin species (i.e. Hb and HbO_2). Consequently, the total absorbance is:

$$A_{total} = \epsilon_{HbO_2}(\lambda)c_{HbO_2}d + \epsilon_{Hb}(\lambda)c_{Hb}d \quad (2.20)$$

Substituting the values of concentrations in (2.18):

$$A_{tot} = [\epsilon_{HbO_2}(\lambda)SpO_2 + \epsilon_{Hb}(\lambda)(1 - SpO_2)](c_{HbO_2} + c_{Hb})d \quad (2.21)$$

With reference to the two wavelengths employed by the PO, the final values of the total

absorbance are:

$$A_{tot}(\lambda_r) = [\epsilon_{HbO_2}(\lambda_r)SpO_2 + \epsilon_{Hb}(\lambda_r)(1 - SpO_2)](c_{HbO_2} + c_{Hb})d \quad (2.22)$$

$$A_{tot}(\lambda_{IR}) = [\epsilon_{HbO_2}(\lambda_{IR})SpO_2 + \epsilon_{Hb}(\lambda_{IR})(1 - SpO_2)](c_{HbO_2} + c_{Hb})d \quad (2.23)$$

that become:

$$A_{tot}(\lambda_r) = [\epsilon_{Hb}(\lambda_r) + SpO_2(\epsilon_{HbO_2}(\lambda_r) - \epsilon_{Hb}(\lambda_r))](c_{HbO_2} + c_{Hb})d \quad (2.24)$$

$$A_{tot}(\lambda_{IR}) = [\epsilon_{Hb}(\lambda_{IR}) + SpO_2(\epsilon_{HbO_2}(\lambda_{IR}) - \epsilon_{Hb}(\lambda_{IR}))](c_{HbO_2} + c_{Hb})d \quad (2.25)$$

The R value is:

$$R = \frac{A_{tot}(\lambda_r)}{A_{tot}(\lambda_{IR})} = \frac{[\epsilon_{Hb}(\lambda_r) + SpO_2(\epsilon_{HbO_2}(\lambda_r) - \epsilon_{Hb}(\lambda_r))]}{[\epsilon_{Hb}(\lambda_{IR}) + SpO_2(\epsilon_{HbO_2}(\lambda_{IR}) - \epsilon_{Hb}(\lambda_{IR}))]} \quad (2.26)$$

Considering (2.26), the SpO₂ expression is obtained:

$$SpO_2 = \frac{\epsilon_{Hb}(\lambda_r) - \epsilon_{Hb}(\lambda_{IR})R}{\epsilon_{Hb}(\lambda_r) - \epsilon_{HbO_2}(\lambda_r) + R[\epsilon_{HbO_2}(\lambda_{IR}) - \epsilon_{Hb}(\lambda_{IR})]} \quad (2.27)$$

Finally, a pulse oximeter performs the following steps:

1. LEDs alternately emit two light beams on the tissue at two different wavelengths;
2. a photodetector, placed according to the transmissive or reflective configuration, receives the residual transmitted light, resulting from the interaction between the incident photons and the absorbing substances inside the irradiated tissue. Finally, two values of the attenuated light intensities are obtained and they are referred to the two wavelengths (i.e. red and IR);
3. the four intensities parameters are evaluated: $I_B(\lambda_R), I_B(\lambda_{IR}), I_P(\lambda_R), I_P(\lambda_{IR})$;
4. from the previous values, the transmittance parameters $\Delta T(\lambda_R), \Delta T(\lambda_{IR})$ are calculated and consequently $\Delta A(\lambda_R)$ and $\Delta A(\lambda_{IR})$ are derived;
5. the value of R is calculated;
6. finally, the peripheral oxygen saturation is estimated. It depends on both the extinction coefficients and the ratio of ratios, it is independent from the initial light intensity and the ray path-length inside the tissue.

2.3 Wavelength selection

Information about the concentration of the oxygen in the blood are determined by analyzing the arterial blood flow, which carries a certain amount of hemoglobin, oxygenated and not.

As discussed in paragraph 2.2, the SpO_2 is determined by the hemoglobin extinction coefficients, specifically Hb and HbO_2 . This molecule is the primary oxygen transport medium in the blood and it has peculiar optical properties. It results extremely performing to spectrometrics methodologies and it is used for the oxygen tracking.

While the *oximetry* exploits the optical properties of arterial blood and precisely the properties of the oxyhemoglobin contained in the complete bloodstream, the *pulse oximetry*, a particular methodology of oximetry, uses wavelengths in red and infrared to detect the percentage of Hb and HbO_2 in arterial blood [36].

To select the best two wavelengths, several observations need to be made [24]:

- Hb and HbO_2 may have good absorbing properties at the selected wavelengths;
- considering the hemoglobin absorption spectra, Hb and HbO_2 must have very different values of the extinction coefficients, at the same wavelength;
- the light beam emitted by LEDs must reach the depth corresponding to the arterial vessel position inside the detected area;
- absorption spectra in correspondence of the wavelengths must be relatively constant.

2.3.1 Hemoglobin absorption properties

The *sensitivity* to SpO_2 changes can be the parameter to consider to set the best wavelengths, in order to reach the highest sensitivity amplitude.

Mook et al. [46] conducted a study to find the appropriate wavelengths range, with a high sensitivity value at varying SpO_2 . They estimated the sensitivity, calculating the derivative of the total absorbance reported in (2.21) and obtaining:

$$\frac{dD_\lambda}{dSpO_2} = (\epsilon_{HbO_2}(\lambda) - \epsilon_{Hb}(\lambda))(c_{Hb} + c_{HbO_2})d \quad (2.28)$$

In figure 2.2, the resulting sensitivity is represented versus different wavelengths. The values are determined by setting the phantom thickness in order that the sensitivity middle point is equal for all the wavelengths (i.e. $D_{SpO_2=0.5} = 0.434$).

The maximum value of sensitivity is localized at 660 nm. This is because in the absorption spectra of the HbO_2 and the Hb at 660 nm, the amplitudes of the extinction coefficients are very different and both the hemoglobin species have a large absorption

capability, as can be seen in figure 2.3. Specifically, this is the first wavelength selected to the instrument.

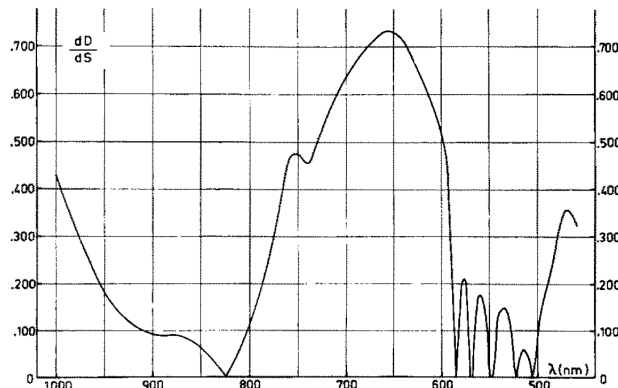


Figure 2.2: Sensitivity distribution of SpO_2 estimation according to varying of wavelengths [46].

Here, higher contribution in the absorption is given by Hb than HbO_2 [24].

Considering figure 2.2, points at 0 sensitivity are the **isosbestic points** in which Hb and HbO_2 have the same extinction coefficients and the same absorption.

In pulse oximetry, the second wavelength can also be selected at a point close to the isosbestic. This is because, in this way, the difference between the extinction coefficients is lower than the one at λ_1 and the contribution of the total hemoglobin concentration is compensated. Thus, the signal is unaffected by the blood variations [46, 47]. The second wavelength is chosen at 940 nm, near to the isosbestic point (i.e. $\lambda = 805nm$).

In this case, the highest absorption contribution at 940 nm is given by HbO_2 .

The rationale of setting red and infrared is clarified observing the value of the extinction coefficients at the selected λ , in the absorbing spectra of Hb and HbO_2 2.3: λ_1 is the point where the extinction coefficients of the two hemoglobin species are very different, while λ_2 is taken near to the isosbestic point.

Pulse oximetry employs this pair of optical sensors to produce *differential absorbance* measurements that permits to limit the noise of the measurements itself [48].

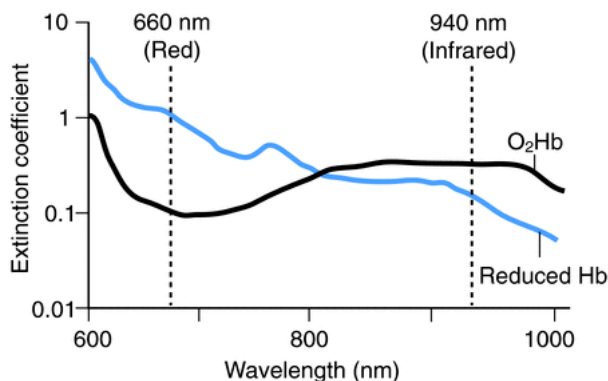


Figure 2.3: Hemoglobin extinction coefficients spectra. Hb indicated in blue and HbO₂ indicated in black. The reduced hemoglobin is localized at the red (660 nm), the oxygenated hemoglobin at the IR (940 nm) [49].

2.3.2 Skin absorbing properties

Opting for the red and IR wavelengths, the selection is additionally correlated to the absorption contribution of the other tissues and substances with which the light can interface. The interaction with other absorbing materials depends on the depth reached by the light beam.

As described in chapter 1.3.1, the most common position of probe can be the finger, the earlobe or the wrist. The result is that light enters in contact with the skin, tissue with specific optical properties that affect the final transmitted light intensity. The main encountered phenomena are absorbing and scattering, caused by the stratified configuration.

It is important to notice that the pulse oximeter wavelengths are included in the *skin optical window*, frequency band in which the cutaneous surrounding tissues absorb less light than the blood molecules. Then, an high penetration depth of the used radiation is guaranteed [48].

The visible skin areas are [50]:

- epidermis, with a thickness of 100 μm and not vascularized. It is composed of dead cell layers (i.e. non-living epidermis), where proteins and lipids are mainly present, with a low liquid quantity. This skin layer has another stratification (i.e. living epidermis) with high skin pigments concentration (e.g. melanin) that can cause scattering phenomena;
- the dermis, with a range of thickness of 1 - 4 mm, that encompasses capillary and peripheral arterial vessels. Dermis has the first vessels that constitutes the skin vascularisation. This cutaneous substrate includes the molecules with the greatest contribution to absorption in the visible spectrum (i.e. carotene, bilirubin and

hemoglobin);

- the subcutaneous fat has a width depending on the area under observation and it can be within 1 - 6 mm.

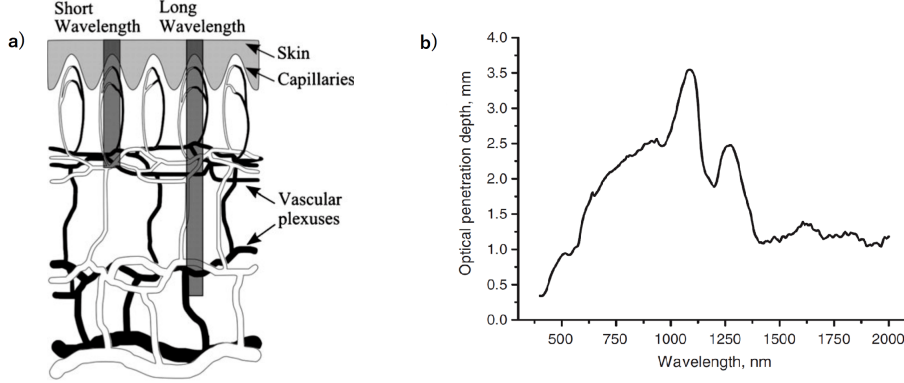


Figure 2.4: a) Structure of blood vessels in the skin, interacting with the light beam [51]; b) light diffusion depth of the wavelength changes in the optical range from 400 to 2000 nm [50].

Bashkatov et al. [50] analysed the optical properties of the cutaneous tissue. They estimated the depth at which the light penetrates into the several layers of the skin, in the wavelength interval from 400 to 2000 nm. The depth values were found on the basis of the scattering and absorption coefficients of the most absorbent dermis molecules (e.g. HbO₂ and Hb).

In figure 2.4 b), the optical path-depth δ is equal to:

$$\delta = \frac{1}{3\mu_a(\mu_a + \mu'_s)} \quad (2.29)$$

where μ_a and μ'_s are the absorbing and scattering coefficients respectively [50].

As shown in figure 2.4 a), for high wavelength values the light beam reaches the deepest arterial vessels in the dermis.

The pulse oximeter employs the wavelengths in the red and the near-infrared, thus it is possible to detect more information about saturation. Indeed, at these depths (i.e. 0.8 - 1.5 mm) arterial vessels present in the vascularized layer of the dermis are intercepted. Utilizing these λ values, the principal disadvantages are the high motion sensitivity and the scattering due to the surrounding tissues [24, 34, 51, 50, 52, 53].

Shorter wavelengths (e.g. green or orange) are interfaced with the superficial skin vessels. The signal is less influenced by the motion artifacts and the light is absorbed almost immediately by the more superficial vessels, suffering less from the scattering effect [51, 53]. In these conditions, the signal/noise ratio is incremented more than in the case

of longer wavelengths. However, the details derived from the signal are very limited as the light is promptly absorbed by the skin pigments and the water present in the most superficial layer.

Precisely, the contribution of the skin pigment (i.e. melanin) is relevant in the range of wavelengths higher than 600 nm, while the water absorbs mainly for λ values greater than 950 nm (i.e. far infrared and UV) [24].

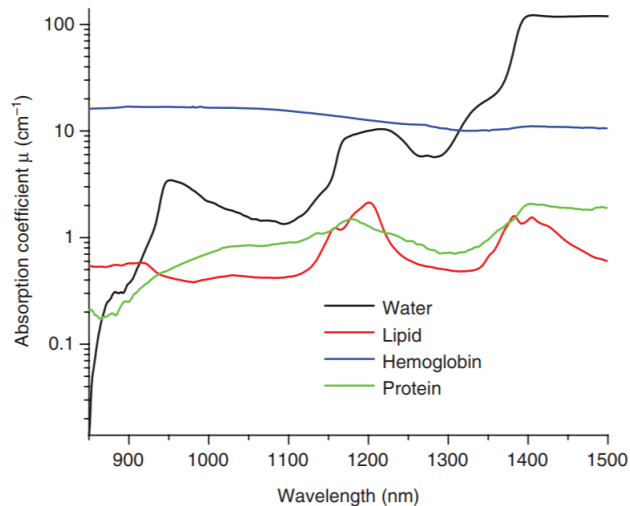


Figure 2.5: Absorption spectra of the more absorbent skin molecules [54].

The more general absorbing spectra to consider, comprehending all the skin absorbent coefficients curves, is depicted in figure 2.5.

2.3.3 LEDs characteristics

The last criterion for the wavelengths selection is based on the LEDs characteristics. The chosen λ are usually localized in correspondence of a flat portion of the hemoglobin absorption spectra. This is because the LEDs real characteristics are bell shaped and do not emit a monochromatic light beam.

If the absorption spectra is too fluctuating around the chosen wavelengths, the value of SpO_2 would be too much altered considering the variability of the resulting extinction coefficients, induced by the wavelengths comprised in the light beam.

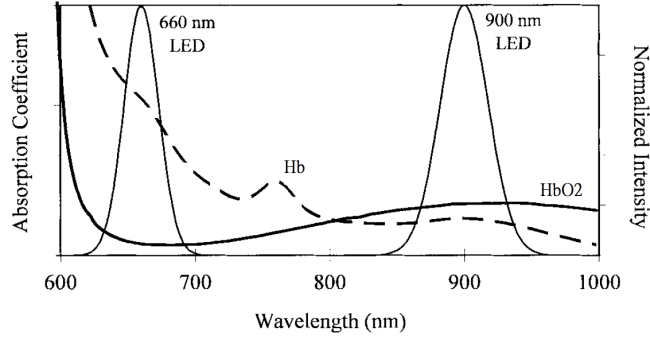


Figure 2.6: Hemoglobin absorption spectra and LEDs characteristics [55].

This concept will be detailed in the methodologies chapter, considering the study [56].

2.4 Instrument calibration

The SpO_2 formula is obtained considering that the path-length of the transmitted light is the same at the two wavelengths. Nevertheless, this assumption disregards the scattering contribution, which needs to be taken into account.

The scattering causes changing in the light trajectory (i.e. deflection) due to the multiple collisions with the surrounding particles [48]. The dispersion is more evident when light, of a certain wavelength, interacts with substances of comparable size (e.g. red cells with a diameter of $7 \mu m$ and the light beam at the IR wavelength, which is of the order of micrometers).

The scattering influences the final pulse oximeter measurements, resulting in their overestimation and reducing the instrument accuracy [57]. In Particular, the contribution of the light diffusion affects the absorbance relation, as expressed in the following:

$$A_{tot} = \epsilon(\lambda)cd + G \quad (2.30)$$

Where G is the loss coefficient due to scattering. It is not possible to estimate this coefficient as it depends on the substances interacting with the light beam and the reciprocal positioning of LEDs and photodetector [38].

In addition, the optical path-length increases, because the deflected light interacts with other substances (e.g. red blood cells). These substances deflect the light again and the final path-length to arrive to the photodetector is higher.

The (2.27) expression can be more correctly reformulated as:

$$SpO_2 = \frac{\epsilon_{Hb}(\lambda_r) - \epsilon_{Hb}(\lambda_{IR})R(d_{IR}/d_r)}{\epsilon_{Hb}(\lambda_r) - \epsilon_{HbO_2}(\lambda_r) + R(d_{IR}/d_r)[\epsilon_{HbO_2}(\lambda_{IR}) - \epsilon_{Hb}(\lambda_{IR})]} \quad (2.31)$$

where the ratio d_{IR}/d_r is not simplified, since in real conditions the optical paths are different. Thus, the two light beams interact differently with the skin: they reach different skin layers and cover different lengths [58].

The final saturation values cannot be derived directly from the Lambert-Beer Law, as the values of G and the d_{IR}/d_r ratio remain unknown. The more practical solution is the instrument calibration [59].

2.4.1 Instrument calibration procedure

The calibration procedure is realized considering the following steps:

1. the R value is determined as in (2.17), from the PPG signal collected on the subject skin;
2. concurrently, the measurements of the arterial oxygen saturation is estimated, using spectrophotometry analysis of the blood samples;
3. each R value, measured by the pulse oximeter, is associated to the corresponding empirical value of SaO_2 and they are together reported in a *look-up table* [60].

In this way, the relation between the R value and the SpO_2 measurements is experimentally determined.

The analytical expression, to obtain the final SpO_2 values, is derived by interpolating the relation between the R ratio and the SaO_2 from the CO-oximeter, as in figure below:

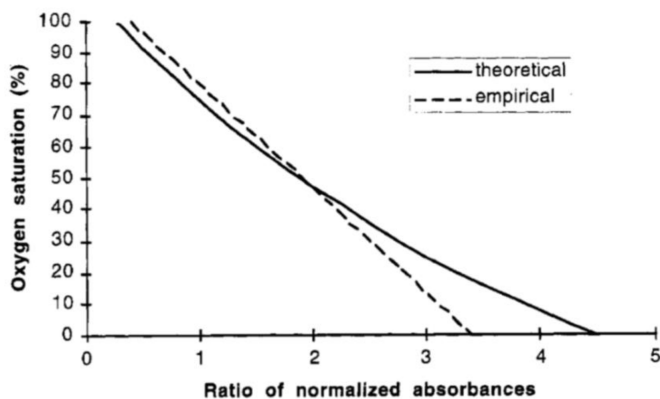


Figure 2.7: $R - \text{SpO}_2$ theoretical and empirical relation [61]

Based on the curves in figure 2.7, the SpO_2 formulas can be worked out as [57]:

$$SpO_2 = \frac{k_1 - k_2R}{k_3 + k_4R} \quad (2.32)$$

$$SpO_2 = k_1 - k_2R \quad (2.33)$$

$$SpO_2 = k_1 + k_2R + k_3R^2 \quad (2.34)$$

where the k_i coefficients are experimentally determined.

This is a first limit of the calibration procedure, since the values of the coefficients may vary, according to the subject health conditions.

A second issue is the deviation between the empirical and theoretical model, in correspondence of low saturation values. For ethical reasons, it is prohibited to make experimental measurements in strong hypoxia cases. Therefore, the accuracy of the pulse oximeter decreases significantly for saturation values below 80%, given the impossibility of collecting data under this percentage [59].

The accuracy of commercial pulse oximeters is about 2%, comparing SpO_2 and SaO_2 concurrently on healthy subjects. The accuracy is calculated considering the standard deviation (SD) resulting from the difference between SpO_2 and SaO_2 . This results in an expected error of about 3-4%, which is clinically acceptable [59].

2.4.2 Calibration-free methodologies

The calibration methodology turns out to be patient-dependent, in terms of placement of the sensors and tissue thickness. In order to avoid these issues, different calibration-free procedures have been developed [38, 62, 63].

Nitzan et al. [62] realized a pulse oximeter that does not need to be calibrated, composed of two LEDs at close wavelengths (both in the infrared range). This approach permits to implement the initial SpO_2 formula in (2.27), obtained from the Lambert-Beer Law. Since the pair of wavelengths is in the same optical interval, the light path can be considered equal and the scattering effects are constant, not contributing to the determination of the absorbance variations. Therefore, under these conditions the instrument does not require any calibration.

In the research, by Nitzan et al. the lower accuracy was mainly attributed to the limited reliability of the extinction coefficients in the literature and to the shape of the real LEDs characteristics, which brought to use optical fibers with the narrowest possible intensity spectrum.

2.5 Clinical applications

Pulse oximetry measurements are largely utilized in the healthcare field and are regularly adopted in clinics and hospitals nowadays. From the saturation measurement, it is possible to detect cardio-respiratory and sleep disorders.

Adopting this principle to build a medical device, the benefit is the non-direct contact between electrical components and the subject, making them definitely safe. In addition, the possibility to have electromagnetic interference is minimal [40].

The pulse oximeter has useful properties to track oxygenation during invasive procedures, intensive care and hospitalizations.

Conventional pulse oximeters measure SpO₂ and HR [36, 37], but other physiological parameters can be provided by the device, taking into account the waveform of the PPG signal. The most important parameters are briefly reported below.

2.5.1 Perfusion Index

The perfusion index (PI) is estimated as the percentage ratio of the PPG signal alternating component and the corresponding continuous component, at the IR wavelength [33]:

$$PI = \frac{AC_{IR}}{DC_{IR}} \times 100\% \quad (2.35)$$

The perfusion Index is useful because [33, 64]:

1. it is an excellent quality index to understand the suitability of the position in the detection area for the specific subject;
2. it permits to evaluate the total time interval required to peripheral capillary refill;
3. it allows to appraise the level of peripheral perfusion. PI indeed evaluates the amount of peripheral arterial blood flow (i.e. pulsating component) compared to the respective non-pulsatile component.

The PI range is within 0.02% and 20%. Considering higher or lower values of the PI, the heart impulse strength can be determined [33]:

- if the value of the PI is low, the power of the heart impulse will be scarce, as the blood-flow reaching the peripheral tissues. This case denotes vasoconstriction;
- if the value of the PI is high, the heart pulse will be more powerful and the blood-flow quantity reaching the peripheral tissues will be elevated. This case is correlated to vasodilatation.

At present, Masimo [65] is the most reliable device, that applies 5 different highly specific and sensitive signal processing algorithms to compute the PI [33].

The effectiveness of therapeutic interventions is one of the information detected using the PI.

There are external factors that can influence the PI values (e.g. temperature at the site of skin measurement) and factors correlated to the influence on the arterial blood flow (e.g. states of anxiety, injection of anesthesia) [33].

Nowadays, this parameter is under-used for home monitoring, when patients are not in severe health conditions. It is fundamental in hospitals, mostly with severely ill patients and to trace the event of anesthetic failure [64].

2.5.2 Pleth Variability Index

Pleth Variability Index (PVI) represents the variation of PI, considering the duration of one respiratory cycles.

During the breathing cycle, the PPG signal presents variations, expressed by the PVI. Physiologically it is possible to understand vascular tone, blood volume (e.g. higher values indicate hypovolemia) and intrathoracic pressure [66]. The PVI is calculated as the PI variations, in a constant time interval [33]:

$$PVI = \frac{PI_{max} - PI_{min}}{PI_{max}} \times 100\% \quad (2.36)$$

Where, PI_{max} is the PI highest value and PI_{min} is the lowest one.

The respiratory cycle is characterized by the momentary reduction of the volume output, that occurs following an inspiration since the venous blood cannot return to the heart [33].

Clinicians can regularly and non-invasively consider this parameter to monitor the stability of the intrathoracic pressure and intravascular fluid volume [33].

2.5.3 Respiration Rate

Respiration rate is an indicator of possible respiratory dysfunction, able to trace the respiratory conditions.

Serious respiratory dysfunction (e.g. breathing infections, depression and respiratory failure) can be predicted observing changes in the RR index [67]. The RR influences the PPG waveform form, in particular[67]:

1. the DC component, as the venous blood volume varies during the inspiration and the expiration;

2. the AC component amplitude, as the modifications in the intrathoracic pressure can modify the cardiac activity.

Addison et al. [67] used the PPG signal inside the algorithm to extract from it information about the Respiration Rate.

2.6 Pulse oximeter vs CO-oximeter

Physical conditions associated to the percentage of oxygen in tissues and blood can be classified as follows [57]:

1. **hypoxia** is a serious condition: oxygen in tissues is insufficient and this leads to cellular death;
2. **hypoxemia** indicates scarce amount of oxygen in the blood. It is worth mentioning that hypoxemia does not provoke hypoxia;
3. **hyperoxia** identifies high concentration of oxygen in the bloodstream.

Pulse oximeters can recognize only the hypoxia and hypoxemia conditions, i.e. values of SpO₂ as low as 80%. Given the toxic nature of the free radicals, hyperoxia state is dangerous as well [57]. If accurate values of SpO₂ are required, e.g. to detect hypoxemia, the pulse oximeter cannot be used as the only monitoring instrument [42].

The value of SpO₂ is directly correlated to the one of the SaO₂.

Trustworthy values of oxygen saturation are provided by the **CO-oximeter**, which invasively analyses blood samples.

Hemoglobin species are classified into two groups:

- **functional hemoglobins**, able to reversibly incorporating oxygen molecules. Functional hemoglobins are Hb e HbO₂;
- **dysfunctional hemoglobins**, which do not combine with oxygen molecules reversibly. Dysfunctional hemoglobin are Methemoglobin (metHb), Carboxyhemoglobin (COHb) and Sulphemoglobin.

The percentages of the oxygen saturation are defined as functional and fractional SpO₂. The functional SpO₂ is estimated as the concentration of HbO₂ considering only the functional hemoglobins (i.e. SpO₂ estimates by pulse oximeter). However, the fractional SpO₂ considers the entire variety of hemoglobin concentrations and it is determined as [68]:

$$SpO_{2fractional} = \frac{[HbO_2]}{[tHb]} \times 100\% \quad (2.37)$$

where $[\text{HbO}_2]$ is the oxyhemoglobin concentration and $[\text{tHb}]$ is the sum of the all hemoglobin concentrations present in the blood-flow.

CO-oximeter invasively collects blood samples by means of a small probe and then evaluates the saturation, analyzing in-vitro spectrometer exams [68].

Additionally, the procedures to collect the samples must be performed rigorously [69]:

- blood is inserted in a heparinized and air-free syringe;
- it must be fine-merged;
- the air bubbles must be eliminated;
- the final form must be allocated on ice.

To distinguish the results of pulse oximeter from the ones of CO-oximeter, oxygen saturation is mentioned as percutaneous oxygen saturation [19].

Examining their absorption spectra, the single hemoglobin species respond to the light in different and specific manners.

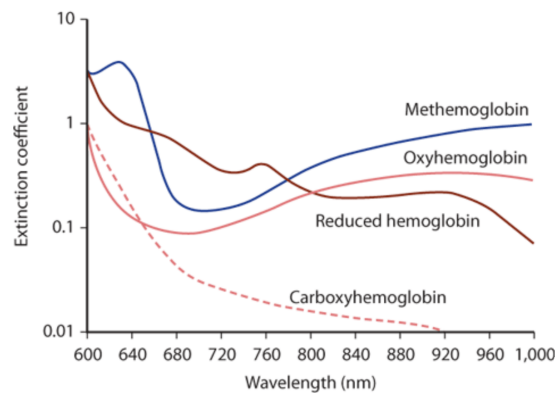


Figure 2.8: Total hemoglobin absorption spectra (600-1000nm)[70]

CO-oximeter employs inspection on the sample considering a certain range of wavelengths (within 475 nm and 600 nm) and applying the Lambert-Beer Law [68, 69]. Total hemoglobin (tHb) is first determined and MetHb, COHb, HbO₂ and Hb are obtained from tHb. The system is not sensitive to sulfhemoglobin, but reading CO-oximeter's output, it can be deduced (resulting in false high value of MetHb) [68].

If the SpO₂ returns ratios below 80%, results are not trustworthy. In such case, the use of CO-oximeter is necessary to verify a possible desaturation. The CO-oximeter is utilized after the exposure on toxic atmosphere or substances, whenever there is a clear difference between the partial pressure of oxygen in the blood and the output of the pulse oximeter [69].

The pulse oximeter is greatly recognized in the medical field, because of its affordability and the feature to continuously monitor physiological parameters, unlike the CO-oximeter which does not provide neither of the previous properties.

In conclusion, the CO-oximeter is used when the patient's physical conditions are not traceable with the PO.

2.7 State of the art

Nowadays, commercial pulse oximeters are clinically oriented, mainly for monitoring serious cardio-respiratory diseases (COPD).

The most common device models are the hand-held and the finger pulse oximeters, that are identical devices only differing in the design. These devices are in transmission mode and use the red and the IR LEDs.

Hand-held model presents a portable monitor, where the SpO₂ and the HR values are displayed. It can be coupled with different probe types (e.g. finger clips and earlobe clips). This pulse oximeter model is more exploited in the clinical environment.

Finger pulse oximeters are composed by clips, applicable directly to the fingers. There is also a wrist model, remotely connected to a finger clip to detect the signal and to estimate the SpO₂ values. In these cases, patients can utilize the devices as home monitoring tools.



Figure 2.9: A) hand-held pulse oximeter [71] B) finger pulse oximeter [72] C) wrist pulse oximeter [73].

In figure 2.9 C), probes can also be applicable on the earlobe.

All the PO have the CE certification, which allows to establish the ranges of reading accuracy and resolution.

SpO₂ sensors can be mounted inside wearable watches, but the measurement becomes very unreliable because they are heavily affected by motion artifact. Consequently, the resulting estimations are not clinically trustworthy.

Most of the pulse oximeters on the market are synchronized with applications compatible to smartphones and tablets, increasingly moving towards the telemonitoring field.

2.7.1 Masimo Signal Extraction Technology - SET

Masimo SET is the most established technology, able to follow the low perfusion cases and the ones affected by motion artifacts. The PPG signal is analysed by four parallel algorithms, to improve the SpO_2 and HR estimations.

Considering the blood oxygen saturation in the absence of movement, the arterial component is the only one associated to the PPG alternating component.

However, in movement conditions the venous components or the tissues motion can be erroneously attributed to the arterial pulsation.

SET technology simultaneously examines both the arterial alternating component and the noise source (e.g. venous signal and respiratory components of the signal).

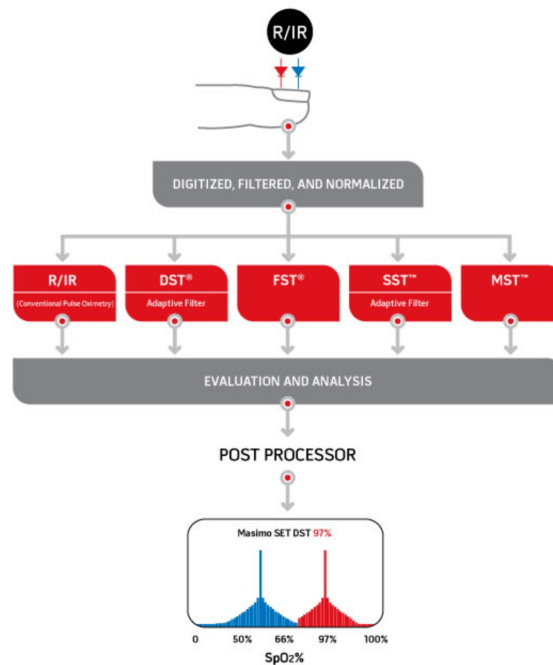


Figure 2.10: SET technology passages representation [65].

As shown in the histogram in figure 2.9, the venous signal is attributed to lower SpO_2 values (blue) than the ones of the arterial signal (red). The algorithms distinguish the two contributions and eliminate noise, using adaptive filters. This improves the accuracy of SpO_2 and HR measurements, even during motion [65].

Masimo SET devices are the only pulse oximeters that can provide continuous measurements of PI and PVI as well as SpO_2 and HR, difficult to calculate accurately.

MightySat Rx fingertip pulse oximeter



Figure 2.11: MightySat Rx fingertip pulse oximeter [65].

The MightySat Rx pulse oximeter by Masimo [72] is a fingertip device able to calculate SpO₂, HR, PI, PVI and RR. The PPG signal is clearly reported on the monitor, followed by the signal quality index (SIQ), representative of the SpO₂ reliability and shown with a digital level line reported on the signal.

MightySat is used in hospital but also as home-monitoring tool (e.g. to trace workout, diet and sleep). It is sensitive to low perfusion conditions and can correctly estimate the parameters, also during motion.

Shah et al. [74] compared three devices (i.e. Masimo Radical, Nellcor N-600 and Datex-Ohmeda TruSat) to evaluate that with the highest SpO₂ sensitivity and specificity, during the motion (simulated and not) and low perfusion conditions (desaturation level about 75%). Masimo device turned out to be the best pulse oximeter, with the best values of sensitivity (100% and 95%) and specificity (93% and 97%).

The device can be synchronized with smartphone and tablet, using an application compatible to both iOS and Android, since it is equipped with a Bluetooth low energy interface. The application can alert in case of emergency and also displays the PPG signal.

	SpO ₂ (%)	HR (bpm)	PI (%)	RR (rpm)	PVI (%)
Visualization Range	0-100	25-240	0.02-20	4-70	0-100
Resolution	1	1	-	1	1

Table 2.1: Visualization range and resolution [65].

Accuracy	ACC Range	Motion	No Motion	Low Perfusion
SpO2 (%)	70-100	3	2	2
HR (bpm)	25-240	5	3	3

Table 2.2: MithySat Accuracy [65].

In the reported tables, the visualization range, the device resolution and the accuracy are reported, evaluated considering the A_{RMS} . It is a statistical calculation based on the difference between the device measurements and the reference measurements. The device has the CE mark and is not yet available in the United States.

2.7.2 Vyntus Walk Mobile Exercise Testing

Vyntus pulse oximeter monitors the SpO₂ level and evaluates the respiratory function during the *six-minute walking test* (6MWT), performed in clinical or hospital environment [75]. Patient executes an exercise in which walks for 6 minutes, in order to evaluate the Chronic Obstructive Pulmonary Disease (CODP) and heart disorders severity. During the walk, several parameters are calculated, among which of these is the peripheral oxygen saturation.



Figure 2.12: Vyntus Walk Mobile Exercise Testing [75].

Vyntus pulse oximeter consists of a wearable watch, displaying the heart rate and the oxygen saturation level. It is connected to a transmission sensor that can be a finger, a forehead and an ear probe type.

Specifically, if the probe is changed, the system accuracy changes. From the data-sheet, the accuracy values are different using the soft sensors (i.e. small, medium, large) or the flex ones (i.e. for adult, child, infant).

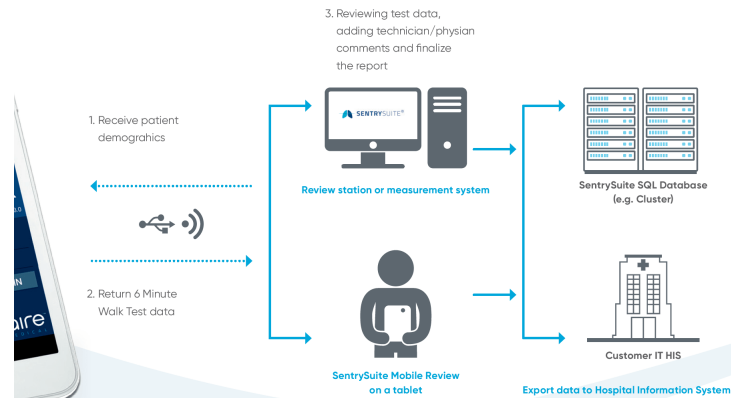


Figure 2.13: Representation of communication among the system components [75].

During the test, data are simultaneously transmitted to a tablet via wi-fi or Bluetooth. The communication is mediated by the application, installed on the remote system, by means of which the clinician can visualize the patient progresses in real-time. Finally, the doctor can send the collected parameters to the central database (i.e. SentrySuite). In figure 2.13 the communication among device - tablet - specialist and the database station is reported.

Other parameters can be manually written in the App (i.e. arterial pressure value, oxygen supply, perceived effort index and bode index).

2.7.3 Nonin: Onyx II 9560

The Nonin Onyx II 9560 pulse oximeter [76] is a small, light and portable finger pulse oximeter.



Figure 2.14: Onyx II 9560 [76].

It is a transmission device, with the red and the IR LEDs and has a size suitable for both adults and children, with different fingers thickness.

Onyx II is largely employed in hospitals or long-term care and qualified nursing facilities, for emergency services and for home-monitoring.

The device can recognize COPD and cardiac pathology (e.g. congestive heart failure, CHF),

since the 27% of the patients suffer from both conditions.

It is an FDA approved device and has the airworthiness approval for use in military aircraft.

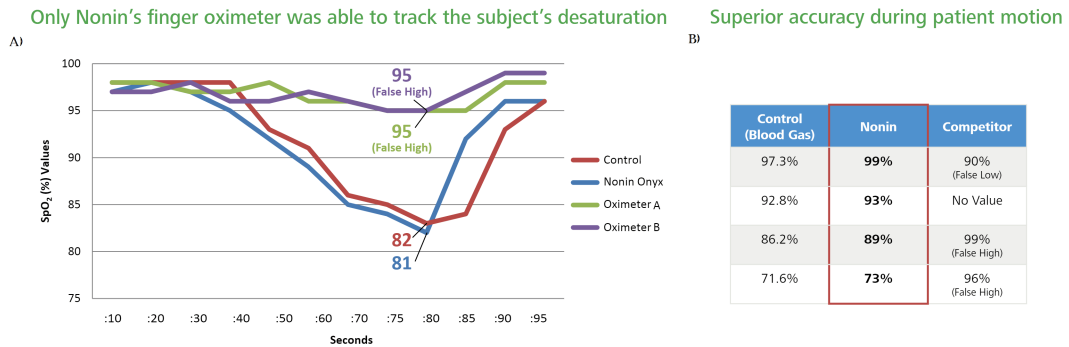


Figure 2.15: Comparative evaluation of different commercial PO [76].

The implemented technology is the PureSat, based on the adaptive filtering and applied peak-to-peak on the PPG signal. Thanks to the sophisticated algorithm, Onyx II is sensitive to low saturation values and it is not altered by the motion artifact.

In figure 2.15, the Onyx performance is compared with that of other pulse oximeters, under critical measurement conditions. Considering the graph 2.15 A) Onyx 9960 is the only device sensitive to the lowest saturation level. Then, the SpO_2 percentage returns to 96% after the detected 82%. The other tested devices estimate SpO_2 modifications only of 3%.

In table 2.15 B), Nonin pulse oximeter correctly detects the movement, differently from the other tools that detect false lower and higher values, because of the motion artifacts.

Additionally, Onyx can calculate the SpO_2 values, independently of the skin pigmentation and communicates the data via Bluetooth, in real time.

In tables 2.3 and 2.4 the visualization interval and the accuracy of the PO are reported .

	SpO2 (%)	HR (bpm)
Visualization Range	0-100	18-321

Table 2.3: Visualization range [76].

Accuracy (digit)	ACC Range	Normal Condition	Low Perfusion
SpO ₂	70-100 %	3	2
HR	20 - 250 bpm	3	3

Table 2.4: Onyx II 9960 Accuracy [76].

2.7.4 Philips pulse oximeter

Philips design four pulse oximeters models (i.e. 3 hand-held and 1 wrist) [77].



Figure 2.16: From left: 1) GO₂ Pulse Oximeter, 2) 920M Plus hand-held Oximeter, 3) 920M hand-held Oximeter and 4) WristOx2 Wrist-worn Pulse Oximeter [77].

WristOx2 pulse oximeter [78] is a wrist-worn model, employed for home, clinical and ambulatory monitoring. It is minimally irritating and estimates the SpO₂ specially during the night, as sleep monitoring. The device can communicate via Bluetooth for the data transmission and it does not have volatile memory.

The 920M pulse oximeter is an hand-held model, easy to use for both the patient and the healthcare provider. In contrast to the first model, it can record the signal and estimates the parameters for 72-hour. Depending on the patient (adult or child), the model of the measurement probe should be chosen as on the finger or on the earlobe.

2.7.5 Garmin: Fenix 5/5S/5X Plus



Figure 2.17: Fenix 5X Plus [79].

Wearable devices properly calculate physiological parameters, useful for sport purpose (e.g. HR) [80]. Garmin company has realized a new smart-watch that estimates the oxygen saturation. The specification is that the calculated SpO_2 has no diagnostic significance and provides only health indications.

The smart-watch is composed of two green LEDs, used for the estimation of all the other parameters, and the red and the IR ones that in reflection mode compute the SpO_2 .

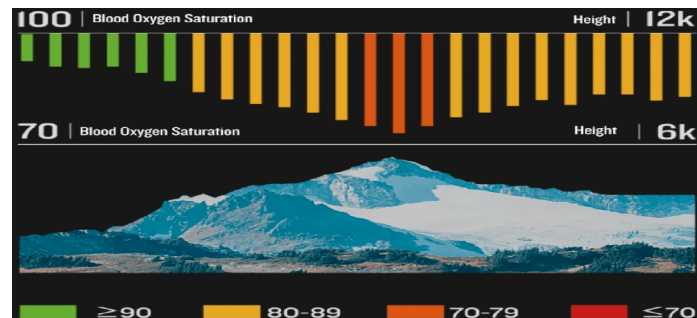


Figure 2.18: Representation of the SpO_2 box diagram on the Fenix 5X Plus display [80]

Real-time evaluation of the SpO_2 is informative about the altitude effect on the body, especially during high altitude excursions. Associating these measurements with the HR, the effectiveness of physical activity is improved. Other contributions are given for the sleep monitoring, to keep track of the sleep phases.

2.7.6 Pulse oximeter on the market contest

Several statistical studies evaluated the economical investments in the biomedical technologies field, especially aimed to pulse oximeters [81].

An expenditure of \$1.8 billion was calculated in 2018, with an annual growth of 6.8% in the purchase of the pulse oximeters by specialized hospital and home monitoring facilities.

The sanitary budget necessary to sustain illness cardio-respiratory diseases (e.g. COPD) is elevated and \$25 billions of dollars have been estimated for the treatment of the pathology. The annual request for telemonitoring pulse oximeters, to permit the patient-clinician-centre communication, will increase.

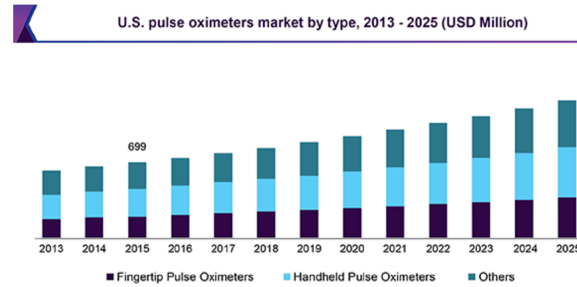


Figure 2.19: The global pulse oximeter market trend (from 2013 to 2025) [81]

In figure 2.19, annual trends are reported, providing the pulse oximeter market until the 2025 and considering all the PO types (i.e. finger, hand-held and other).

From the 2014 to the 2018, different companies enhanced their interest to the telemedicine.

Masimo developed a pulse oximeter compatible to iOS and Android communication platform (e.g. tablet and smartphone), attained the CE marker in the 2015 and the acceptance by the FDA.

CareFusion Corp obtained the Vital Sign from the GE Healthcare in the United States for a total investment of \$ 500 millions of dollars.

Philips joined the Xhale Assurance, Inc. and realized the pulse oximeters, described in part in the paragraph 2.7.4, accurate to distinguish low oxygen perfusion, difficult estimation to perceive for the pulse oximeters.

Initially, the best selling devices were the hand-held types, as largely employed in the operating room. Finger types, on the other hand, are becoming more and more popular in the world market, due to their non-invasiveness and being very practical, especially for the analysis of newborns.

American Academy of pediatrics considers pulse oximeter an essential tool for the early diagnosis of cardio-respiratory diseases. The early detection of CODP diseases, indeed, can avoid the onset of aggravations in the following hours of life, detecting complications already in the first weeks of life.

The PO market is in large developing in North America, followed by Europe. Further growth in the purchase of these instruments is expected in Asia Pacific.

Part II

Materials and Methods

Chapter 3

Hardware System

In the present work, the employed hardware is composed of:

- the STM32 Open Development Environment (STM32 ODE), that includes the STM32 Nucleo expansion board, where the sensor is integrated;
- the multispectral sensors, i.e. VD6281 and VD6282;
- the white and the infrared LEDs.

In this project two versions of the STM32 ODE were utilized.

The first one comprised the VD6281 and the white LED. While, the second version consisted of the VD6282, along with the white and IR LEDs.

In figure 3.1 the final developed system is reported.



Figure 3.1: Final system hardware.

The acquisitions were done with both the boards, and only the second version considered also the IR PPG signal.

The final system was a prototype of a reflective pulse oximeter. The aim is to understand the capability of the spectrometers to correctly evaluate the HR and the SpO₂, together with good algorithm performances.

In the present chapter, the system components will be briefly described.

3.1 STM32 Open Development Environment

The STM32 ODE boards allow the devices prototyping, thanks to their adaptability and simplicity. The system uses the STM32 32-bit microcontroller family and can be connect to other ST components (i.e. STM32 Nucleo Expansion Boards, STM32 Nucleo development boards, STM32Cube software, STM32Cube expansion software and STM32 ODE Function Packs). The STM32 ODE and the expansion boards facilitate the prototyping, accelerating the innovative devices developing.

The most important features of the STM32 ODE system are:

1. STM32 microcontroller in LQFP64 package;
2. 1 user LED shared with Arduino™;
3. 1 user and 1 reset push-buttons;
4. 32.768 kHz crystal oscillator;
5. the mass storage, the Virtual COM port and the debug port, present on-board;
6. the board connectors:
 - external Switched-Mode Power Supply (SMPS) experimentation dedicated connector;
 - Micro-AB or Mini-AB USB connector for ST-LINK;
 - MIPI debug connector;
7. external SMPS to generate V_{core} logic supply;
8. 24MHz Hardware Security Module (HSM).

There are different ST32 ODE, based on the microcontroller type. The STM32 ODE considered in the present work is the **NUCLEO-F401RE**, where the **STM32F401RE** microcontroller is integrated.

The **NUCLEO-F401RE** was coupled with the STM32 Nucleo Expansion Board where

the VD6282 is present.

In figures 3.2 and 3.3, the used STM32 ODE and the Nucleo Expansion Board are reported.

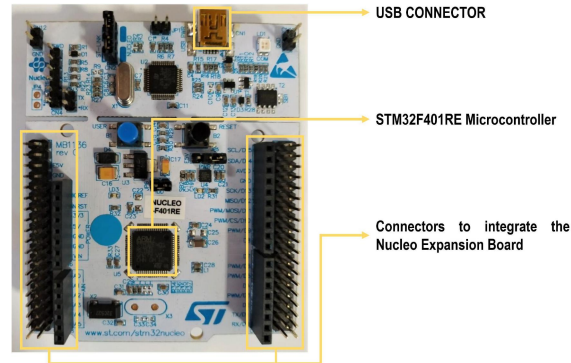


Figure 3.2: STM 32 ODE.

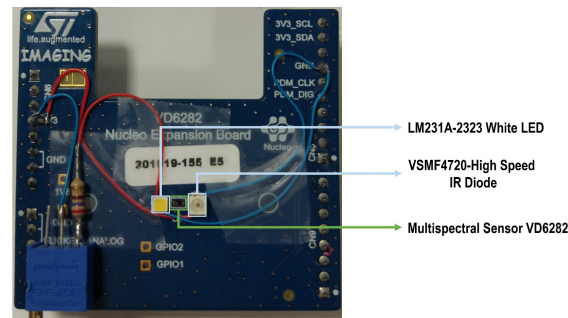


Figure 3.3: Nucleo Expansion Board.

The power supply provided by the Nucleo Expansion Board is of 3.3V. It sustains the conditioning circuit mounted to activate the LEDs.

It is composed of:

- a resistance of 260 Ω and a trimmer regulated at 400 Ω , connected to the white LED;
- a resistance of 240 Ω , connected to the IR LEDs.

The simple developed conditioning circuit is reported below:

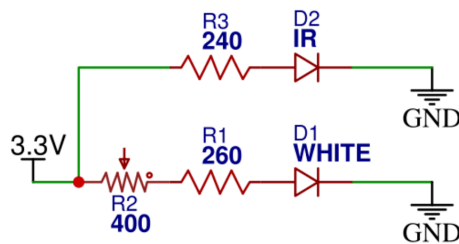


Figure 3.4: Conditioning circuit mounted on the Nucleo Expansion Board.

3.2 Multispectral Sensors

The Multispectral sensors VD6281 and VD6282 are Ambient Light Sensors, realized by STMicroelectronics.

These kind of sensors are typically present in mobile phones, tablet, smartwatches or notebooks to automatically regulate the display brightness, based on the perceived ambient light. In this way, in case of darker environment, the light of the device monitor is not excessively intense and in illuminated open spaces, it is not extremely low.

The sensors used in this work are the smallest ALS presents on the market (1.83 x 1.0 x 0.55 mm). They perceive the surrounding light thanks to their high-end interferometric filters, with an accurate spectral response, and convert the captured light information.

The two version of the photodetector are organized with an optical Ball Grid Array (BGA), constituted of a 6-balls package, as shown in figure 3.5.

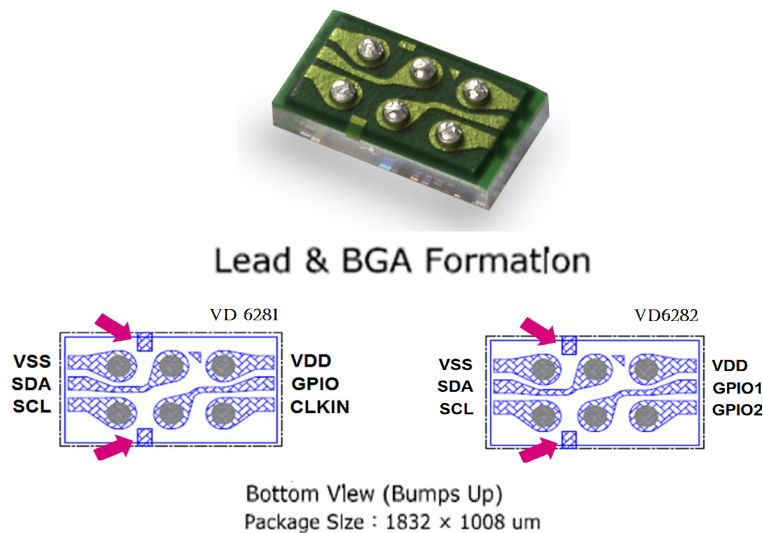


Figure 3.5: Visual anti-rotation mark.

The main sensor features, equal in the two versions of the Rainbow multispectral sensors, are:

- **ADC type:** 24 bit (16 bit+8bit, to obtain high accuracy under low light);
- **analog gain:** programmable gains for high-dynamic range (i.e. 66x, 50x, 33x, 25x, 16x, 10x, 7.1x, 5x, 3.33x, 2.5x, 1.67x, 1.25x, 1x, 0.83x, 0.71x.);
- **exposure time:** parameter that regulates the channels opening, to detect the light. Each incoming light photon is perceived with an integration time step size of about 1.6 ms. The exposure time can be set from 1.6ms to 1.6s.

The analog gain can be set at each channel, independently of the others.

The lower the exposure time value, the lower the number of counts perceived by the sensor. Higher values of the exposure time maintain the channel sufficiently open to perceive enough light photons samples.

Finally, the sensor can be easily applied for mobile applications due to:

- the power supply of 1.8V (it can vary from 1.8V to 1.95V);
- a current of 450 μA of active consumption;
- range of the operating temperature from -30 to 85 °C;
- optical module with thin glass (6-ball BGA).

In the next sections, the main characteristics of the sensor will be reported.

3.2.1 VD6281

The VD6281 is the first version of ALS developed by ST. It is composed by 6 colour channels that can perceive the light in parallel and independently from the other channels. The 6 channel are:

- the UV-A channel, at 350nm;
- the blue channel, at 460nm;
- the green channel, at 555nm
- the red channel, at 620nm;
- the IR channel, at 850nm;
- clear channel, that includes all the above wavelengths;

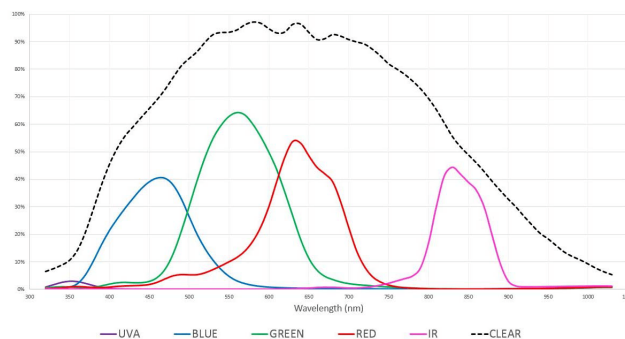


Figure 3.6: VD6281 normalized spectral response, A-GAIN = 50, EXTIME = 250 ms.

It is sensitive to the red, green and blue wavelengths (RGB), to the near infrared wavelength and to the ultra-violet (UV) wavelength. Specifically, its spectral response is reported in figure 3.6.

High-end interferometric filters are included inside the photodiode, with a fast response for the white-balance and it can perceive ambient or artificial light using the UV channel. Each channel includes a 24 bit ADC that allows to collect the colour very rapidly (i.e. less than 1 video frame, <30ms).

3.2.2 VD6282

The VD6282 is the upgraded version of the VD6281. It presents the same characteristics in terms of the design and the fast capability to detect the surrounding light. Differentially from the VD6281, it is composed of 5 channel:

- the blue channel, at 460nm;
- the green channel, at 555nm;
- the red channel, at 620nm;
- the IR channel, at 820nm;
- clear channel, that includes all the above wavelengths;

The spectral responses of the five channels are reported below:

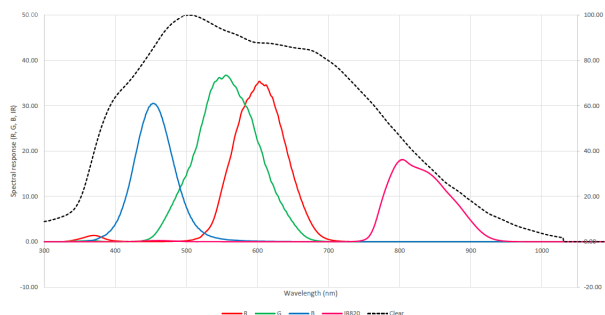


Figure 3.7: VD6282 Spectral Response.

3.3 Employed LEDs

In the present work, a white LED and an IR LED were chosen for the following reasons:

1. the white LED, to understand the performances of the VD6281, and after the ones of the VD6282. Specifically, considering the Rainbow red and green spectral responses, the capability to estimate the SpO₂ and the HR are evaluated;

2. the IR LED, to determine the same data, considering the typical pulse oximeter wavelengths, the IR and the red.

In the present section, the spectral characteristics of the white and IR LEDs are reported.

3.3.1 LM231A-2323 Middle Power LED

The main features of the white LED are:

- dimension : 2.3 x 2.3 x 0.7 mm;
- forward current : $I_F = 150mA$;
- peak pulsed forward current: $I_{FA} = 300mA$,
- operating temperature range: -40 to 100 °C
- LED junction temperature: $T_j = 100$ °C
- beam angle: 120°

The relative emission intensity is reported in the following figure:

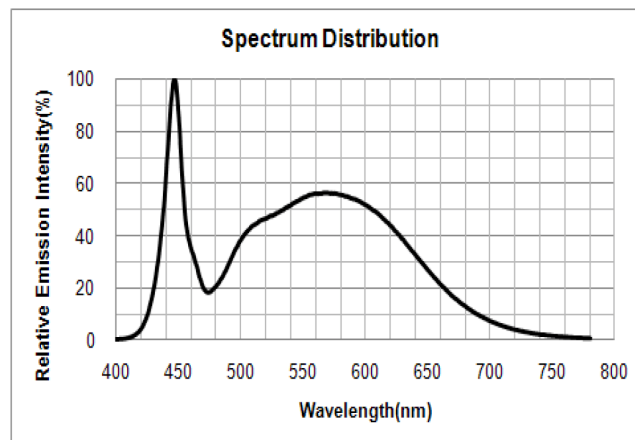


Figure 3.8: White LED spectral distribution.

As showed in figure 3.8, the LED has a good response at the green (i.e. 495-570 nm) and red (i.e. 620-750 nm) wavelengths.

3.3.2 VSMF4720-High Speed Infrared Emitting Diode

The main characteristics of the selected LED are:

- package type: surface mount;

- dimensions (L x W x H in mm): 3.5 x 2.8 x 1.75;
- peak wavelength: $\lambda_p = 870nm$;
- forward current: $I_F = 100mA$;
- reverse voltage: $V_R = 5V$;
- angle of half intensity: $\varphi = \pm 60^\circ$;
- LED junction temperature: $T_j = 100\text{ }^\circ\text{C}$;
- power dissipation: $P_V = 160mW$;
- operating temperature range: -40 to 85 °C

The relative radiant power is reported in subsequent figure:

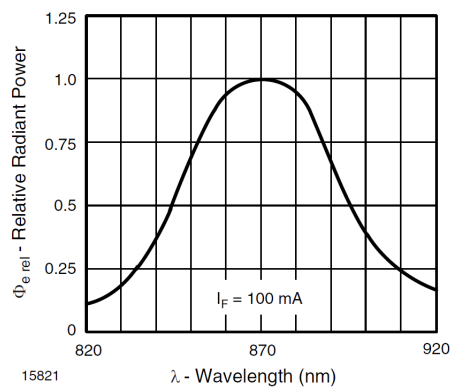


Figure 3.9: IR LED relative radiant power.

Chapter 4

Experimental Setup

The experimental phase consisted of the PPG signal acquisition, from the developed reflectance pulse oximeter. Specifically, the SpO_2 and the HR were evaluated, comparing the values obtained from the Rainbow and the values obtained from the reference device, the transmittance pulse oximeter by Nonin, Onyx II 9560, described in 2.7.3 .

The Rainbow can interface with the Personal Computer (PC) using the USB connector and the Application VD6281 Graphical User Interface (GUI). The Onyx, instead, transmits the data via Bluetooth to the acquisition platform (i.e. PC).

In the next sections, the experimental setup will be described.

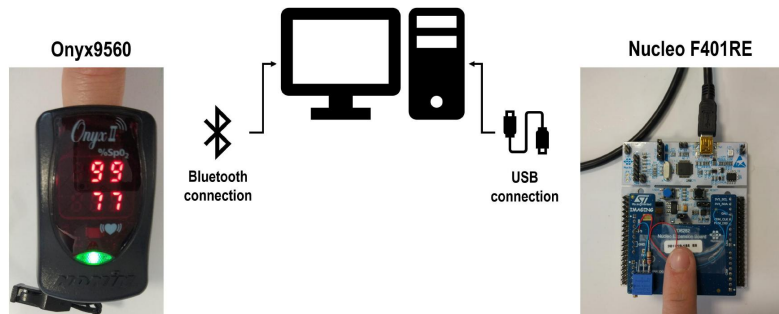


Figure 4.1: Final acquisition system, composed by the Onyx and the VD6282.

4.1 Oxygen Saturation Experiments

The presented dataset were extract from 25 healthy subjects, 10 males and 15 females, ages 24 - 35.

During the acquisition, the subject was seated on the chair, with the left finger placed on the sensor and the right finger positioned inside the Onyx.

During the acquisition, subjects alternated phases of apnoea and normal respiration, obtaining a minimum value of SpO_2 , from the reference device, equal to 94-93%.

The acquisitions duration were of about 5 minutes.

4.2 VD6281 Graphical User Interface

The VD6281 Graphical User Interface (GUI) allows the communication between the Personal Computer (PC) and the **NUCLEO-F401RE**, where the sensor is integrated.

The board is connected to the PC by means of an USB connector. Once the communication between the sensor and the recording system begins, the VD6281 GUI presents the following view:

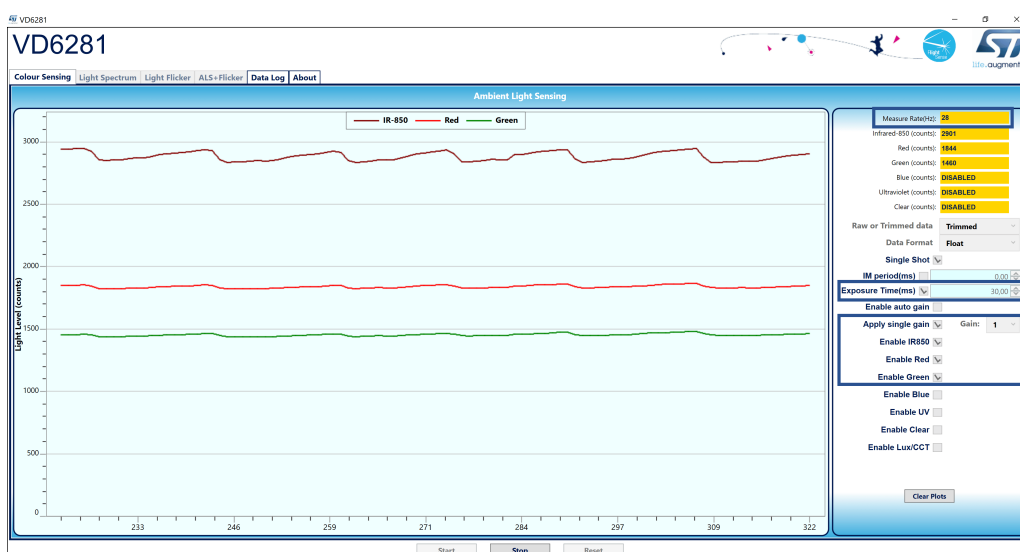


Figure 4.2: VD6281 GUI.

The parameters to set for the acquisition are:

1. the **number of channels** to enable: in this work, the chosen channels were the Green, the Red and the IR (only for the last acquisitions);
2. the **gain**: each channel presents an independent value of gain, to amplify the light amplitude. In the present work, the gain was fixed to 1 for all the channels, so as not to altered the PPG signals morphology and values;
3. the **exposure time**: the time interval in which the sensor channels are sensitive to the light, measured in ms. The higher the exposure time, the higher the light amplitude detected. However, if the exposure time is fixed too large, the **measure rate** (i.e. the sampling frequency) will be lower, consequently the number of the samples acquired will be small.

Because the PPG frequency ranges goes from 0.5 to 8 Hz, the exposure time set in the present work was of about 30 ms, resulting in an effective frequency sampling of 20 Hz (obtained after the pre-processing step);

4. activation of **data log**, to memorize the acquire signal.

The App generates an Excel file, containing the data of the enabled channels in columns. The ones considered in the present project, to extract the signals, are:

1. the **timestamp**, the temporal axis of the signal, reporting the corresponding time instants in which the light sample are perceived;
2. the **infrared**, reporting the light intensity detected at the IR wavelength;
3. the **green**, reporting the light intensity detected at the green wavelength;
4. the **red**, reporting the light intensity detected at the red wavelength;

count	error	timestamp_ms	dataLogCount	infrared	red	green	blue	ultraviolet	clear	infraredI	redRaw	greenRaw	blueRaw	ultravioletRaw	clearRaw	x
2	806	0	103	0	147.7305	353.3477	350.5039	0	0	0	137.0273	373.793	337.3281	0	0	-1
3	807	0	156	1	147.8281	353.7632	351.1172	0	0	0	137.1272	374.2519	337.918	0	0	-1
4	808	0	209	2	147.8125	353.6133	350.7656	0	0	0	137.1016	374.0742	337.582	0	0	-1
5	809	0	261	3	147.779	353.6836	351.1172	0	0	0	137.0839	374.1484	337.918	0	0	-1
6	810	0	310	4	147.7813	354.0532	351.3789	0	0	0	137.0762	374.2555	338.1719	0	0	-1
7	811	0	359	5	147.7852	353.7578	351.1016	0	0	0	137.0781	374.2266	337.9023	0	0	-1
8	812	0	407	6	147.7734	353.6445	350.9961	0	0	0	137.0664	374.1055	337.8008	0	0	-1
9	813	0	459	7	147.7891	353.6172	351.0664	0	0	0	137.0762	374.0764	337.8711	0	0	-1
10	814	0	511	8	147.7891	353.75	351.2773	0	0	0	137.082	374.2188	338.0742	0	0	-1
11	815	0	561	9	147.7656	353.6055	350.8516	0	0	0	137.0586	374.0625	337.6641	0	0	-1
12	816	0	614	10	147.7031	352.8667	350.1043	0	0	0	137.3736	364.7366	336.6867	0	0	-1
13	817	0	665	11	147.7578	351.8438	348.7539	0	0	0	137.0508	372.1592	335.6445	0	0	-1
14	818	0	716	12	147.8203	351.9844	349.0313	0	0	0	137.1094	372.3477	335.9102	0	0	-1
15	819	0	767	13	147.8136	353.1281	350.4961	0	0	0	137.2448	373.7655	337.3203	0	0	-1
16	820	0	815	14	148.3008	353.957	351.1758	0	0	0	137.5547	374.4375	337.9766	0	0	-1
17	821	0	861	15	150.8847	354.4378	351.4367	0	0	0	138.0431	376.1433	338.418	0	0	-1

Figure 4.3: File excel generated by the VD6281 application. The underline cells are the correspondent extracted to obtain the final signals.

4.3 BT OnyxII9560 Client

The BT OnyxII9560 Client is the Nonin user Application, used to interface the PC with the Onyx device. The application window is shown in figure:

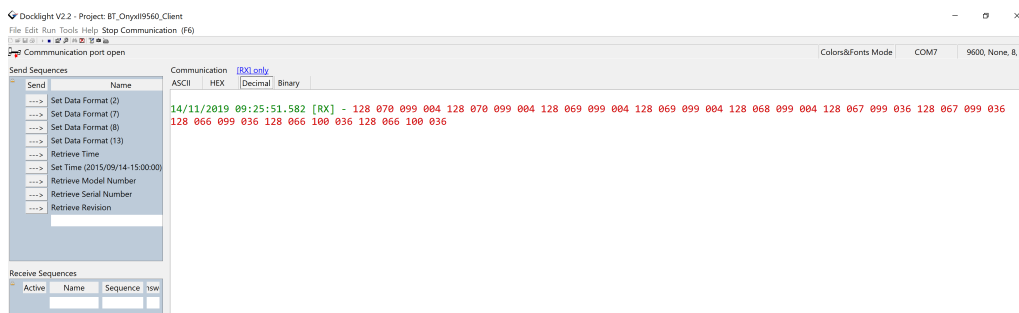


Figure 4.4: BT OnyxII9560 Client.

The Onyx communicates with the PC by means of Bluetooth. The data log is enabled to memorized the SpO₂ and HR data and the data transmission starts.

The application generates a file .txt, imported to Matlab[®], where the data are processed in comparison with the ones elaborated with the Rainbow.

The device estimates the SpO₂ and the HR every 1 second, for that reason the same timing was fixed to elaborate the Rainbow data.

Chapter 5

Developed Algorithm

The described algorithm was realized to estimate the SpO_2 and the HR by means of the sensor VD6281, called *Rainbow* in the next sections.

In the first part, the approach employed for the assessment of the SpO_2 was based on a calibration-free method. The parameter, indeed, was calculated applying exclusively the Lambert-Beer relation. For the present study, the scattering effects were neglected.

In the second part of the project, the sensor was afterwards calibrated, based on the R parameter, obtained from the developed algorithm, and the experimental formulas mentioned in (2.32).

Typically, the coefficients of the SpO_2/R relationships are experimentally evaluated. The procedure consist of an invasive spectrometric analysis, operating directly on the blood samples.

In this preliminary study, the calibration was made acquiring simultaneously the PPG signal from the *Rainbow* and a reference device, the Onyx pulse oximeter 9560.

The R value was calculated by the ratio between the AC and DC components extracted from the PPG signal. The experimental relation of the R ratio and the SpO_2 was appraised, using the coefficients of the linear and quadratic regressions, resulting from the scatter plot of the R ratio and the correspondent Onyx SpO_2 .

To estimate the SpO_2 , the red and green wavelengths were considered and a white LED, with a good spectral response at the chosen λ , was used. In this way, the *Rainbow* regarded channels were the red and the green.

Two PPG signals are acquired from the *Rainbow* and thereafter the processing passages are realized on both of them.

The signals are gathered and offline analysed in Matlab[®] environment. The algorithm steps were developed for real-time application, thus the signal is processed considering one sample per time.

The main steps to compute the SpO_2 are:

1. estimation of the signal sampling frequency;
2. identification of the extinction coefficients, given the wavelengths of interest;
3. selection of the system buffer length, consisting in the total number of samples to acquire before starting the analysis;
4. selection of the time interval to analyze the buffer, when it is completely loaded;
5. PPG signals processing, consisting in the filtering of the Rainbow signals, to obtain the AC and DC components from both the rainbow signals;
6. peaks and minima detection from the AC components, again considering both the signals. The detection begins when the number of the data corresponds to the system buffer length and it is effectuated every set "time interval";
7. estimation of R_{green} and R_{red} ratios;
8. estimation of the total R ratio and consequently, of the SpO_2 ;
9. estimation of the heart rate.

The HR is computed as the distances in samples between two consecutive peaks.

The algorithm firstly acquires a fixed number of samples, from the red and green channels. For the present work, the chosen system buffer length is 300 samples, corresponding to about 15 s of acquisition. When the buffer is completely loaded, the HR and SpO_2 values are transmitted in output every 1s (selected time interval).

The collected signals are poorly affected by motion artifacts, except for the presence of respiratory components. These latter are deleted by the AC filtering operations.

The aim is to set a code that could be implemented in real-time.

In figure 5.1, the flowchart of the algorithm is reported.

Finally, another Rainbow version was calibrated, the sensor VD6282.

At the system, composed by the Rainbow VD6282 and the white LED, an infrared LED was connected, to additionally validate the Rainbow system and the developed algorithm. Other measures were made, both with the white LED and the IR LED, gathering the PPG signal from the red, green and IR channels of the Rainbow.

The SpO_2 from the Onyx and the red-IR Rainbow and the one from the Onyx and the red-green Rainbow were, finally, compared.

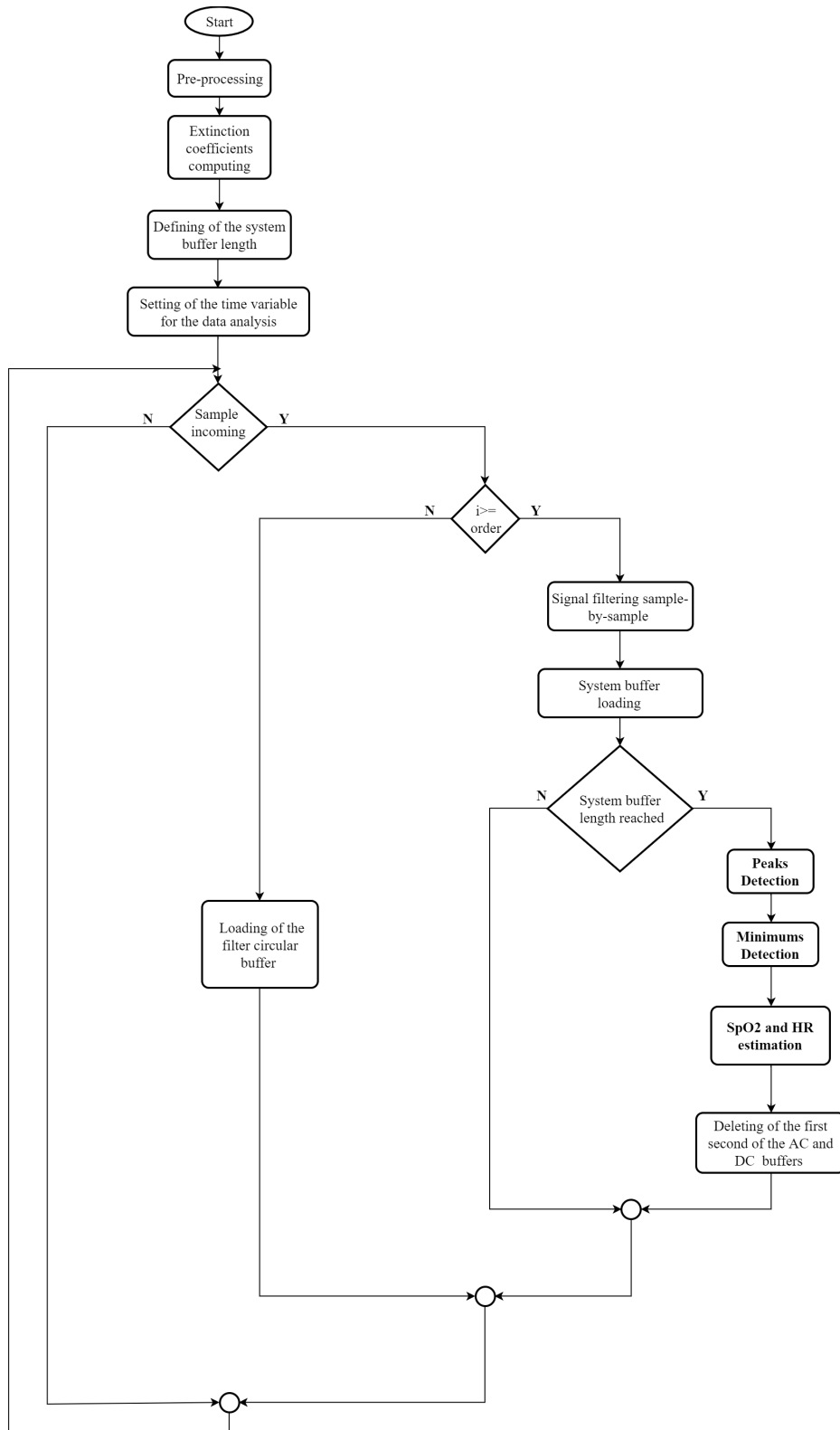


Figure 5.1: Flow chart of the implemented algorithm.

5.1 Pre-processing

The pre-processing phase helps excluding the signal samples that are not useful for the final computation of the SpO₂ and the HR.

The presence of these data is due to the initial instability of the sampling frequency. Indeed, it is lower in the first few seconds and becomes stable after about two minutes, from the beginning of the acquisition.

The instability of the sampling frequency is correlated to the hardware of the acquisition system.

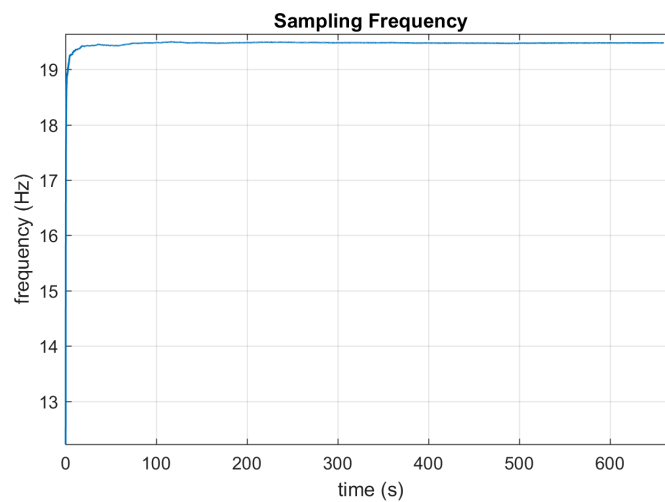


Figure 5.2: Initial transient of the sampling frequency

To remove the data corresponding to the initial transient of the sampling frequency, the following steps were implemented:

1. before starting the true acquisition, the green and red signals from the VD6281 channels are acquired, without having any interaction with the sensor, for a time interval of about two minutes;
2. during this time interval, the sampling frequency is expected to stabilize;
3. after this time interval, the real acquisition begins and the signals are collected by the sensor.
4. the acquired data are analyzed offline, using Matlab[®] and the time axis of the acquisition is extracted (i.e. timestemp);
5. the sampling frequency axis is obtain, considering the number of samples acquired

at the corresponding second:

$$f_s(i) = \frac{i}{timestamp(i)} \quad (5.1)$$

where, i is the i -th sample and $timestamp(i)$ is the corresponding instant of acquisition.

- the samples, positioned in correspondence of the frequency values lower than the mean value of f_s , are deleted.

This threshold value was chosen because the frequency begin to be stable when its value is equal or higher than the average frequency.

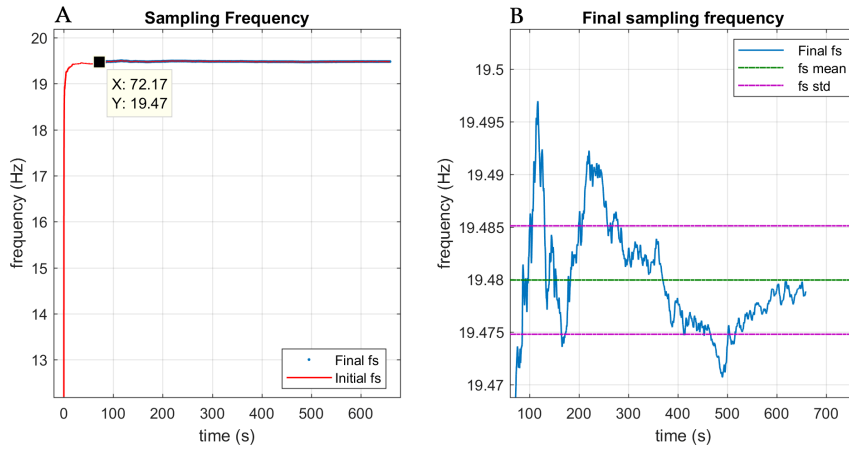


Figure 5.3: A) in red, the initial sampling frequency and in blue, the new sampling frequency values considered. B) Zoom of the new sampling frequency, with the mean value and the standard deviation.

Figure 5.3A) represents together the frequency values and the marker-point, correspondent to the first point of the sampling frequency after the pre-processing. In figure 5.3B), the mean and the standard deviation are reported as reference of the resulting oscillations of the new sampling frequency.

The sampling frequency, considered during the algorithm phases, is the mean value of the final frequency values estimated.

5.2 Extinction Coefficient Identification

The extinction coefficients were calculated using the effective extinction coefficients relations, taken in consideration in the article by De Kock et al. [56].

Specifically, this method was considered because LEDs does not emit a monochromatic light beam and in the same way, each Rainbow channel has a bell shape normalized spectral response.

The wavelengths considered for this work were red (i.e. 620-700 nm) and green (i.e. 491-560 nm). Accordingly, in the Rainbow the red and green channels were taken into account and a white LED only was utilized for the final measuring system.

As mentioned in [28], at the green wavelength, light is absorbed nearly to the surface and suffers less attenuation, compared to the penetration of the IR light beam. Additionally, at the red and the green wavelengths, the hemoglobin spectra are:

- relatively flat;
- closer to the isosbestic point;
- the values of the extinction coefficients are fairly different each other.

Thus, the contribution of the HbO₂ and the Hb are maximized.

Finally, the hardware was extremely simplified, because the Rainbow is sensitive only to the visible spectrum and these two wavelengths were a good compromise between the Rainbow spectral response and the light-tissues interactions.

The final measuring system presents two consecutive optics elements (i.e. LED and Rainbow). Therefore, the contribution of the LED characteristic and the contribution of the Rainbow characteristics needed to be taken into account, for the same wavelengths. In particular, the effective extinction coefficients were obtained by: the normalized characteristic of the white LED, the normalized spectral response of the Rainbow green channel and the normalized spectral response of the Rainbow red channel.

The coefficients were calculated as the mean value of the product between the normalized light intensity and the extinction coefficient:

$$\frac{\sum_{\lambda=\lambda_1}^{\lambda_N} I_{norm}(\lambda) \cdot \epsilon(\lambda)}{N} \quad (5.2)$$

Where, I_{norm} is the normalized light intensity, ϵ is the extinction coefficient, each taken at the corresponding wavelength of the LED (or Rainbow) characteristic, λ_1 and λ_N are the first and the last wavelength of the normalized characteristics.

The resulting extinction coefficients were:

1. ϵ_{Hbw} and ϵ_{HbO2w} , for the white LED;

2. ϵ_{Hbg} and ϵ_{HbO2g} , for the Rainbow VD6281 green channel;
3. ϵ_{Hbr} and ϵ_{HbO2r} , for the Rainbow VD6281 red channel;

The common wavelengths range was at first determined from the intersection among the white LED characteristic and the Rainbow characteristics. The resulting interval comprised the wavelengths from 400 to 750 nm and consequently the values of the I_{norm} were derived from the normalized spectra, for each λ .

The normalized spectra obtained were reported in figure 5.4:

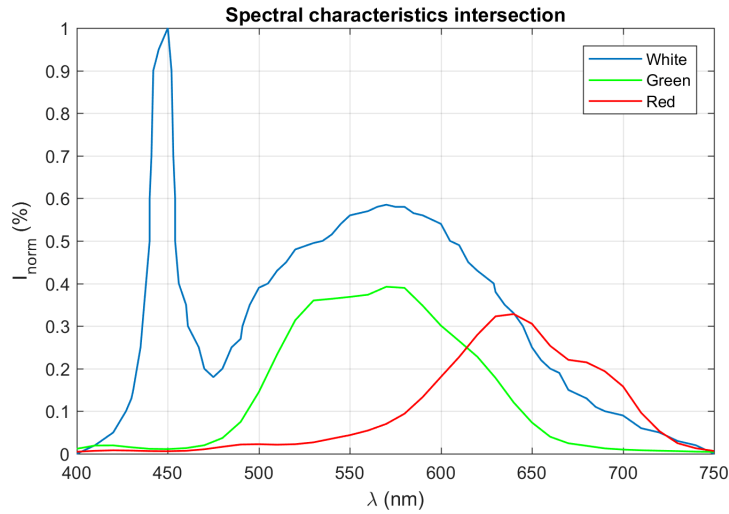


Figure 5.4: Spectral intersection among the white LED and the VD6281 green and red characteristics.

The effective extinction coefficients were found in accordance with the following procedure, firstly described for the white LED:

1. extinction coefficients for the white LED were extracted, starting from $\epsilon_{Hb}(400 \text{ nm})$ and $\epsilon_{HbO_2}(400 \text{ nm})$ up to $\epsilon_{Hb}(750 \text{ nm})$ and $\epsilon_{HbO_2}(750 \text{ nm})$;
2. two vectors of Hb and HbO₂ extinction coefficients were obtained, for all the considered wavelengths.
3. each coefficient was multiplied with the corresponding I_{norm} and the resulting vector was averaged, attained the effective extinction coefficients for the two hemoglobin species (i.e. ϵ_{Hbw} and ϵ_{HbO2w}).

In the same way, the effective extinction coefficients were calculated for the green (i.e. ϵ_{Hbg} and ϵ_{HbO2g}) and the red (i.e. ϵ_{Hbr} and ϵ_{HbO2r}) characteristics.

Finally, the values considered for the SpO₂ estimation were determined as the product between the pairs:

- ϵ_{Hbw} and ϵ_{Hbg} , ϵ_{HbO2w} and ϵ_{HbO2g} , obtaining the overall extinction coefficient of the Hb and HbO₂ for the green wavelength, given the characteristic of the white LED and the one of the Rainbow green channel;
- ϵ_{Hbr} and ϵ_{Hbr} , ϵ_{HbO2w} and ϵ_{HbO2r} , obtaining the overall extinction coefficient of the Hb and HbO₂ for the red wavelength, given the characteristic of the white LED and the one of the Rainbow red channel;

The extinction coefficients evaluated in this work were found from the articles by Zijlstra [82] and the website of Scott Prahl [83].

Prahl estimated the HbO₂ and Hb extinction coefficients, in the wavelengths range from 250 to 1000 nm. Zijlstra et al. determined the same parameters from 450 to 1000 nm. The authors obtained the molar extinction coefficients expressed as $cm^{-1}/(moles/liter)$. The acquisition modality are described in the previously mentioned articles.

Being the SpO₂ expression depends on the ϵ , the minimum alteration on their values can caused large variation in the final SpO₂ amplitude. In the present work, the extinction coefficients from both Prahl and Zijlstra were utilized for the SpO₂ calculation, evaluating the ones that returned the most reasonably saturation results.

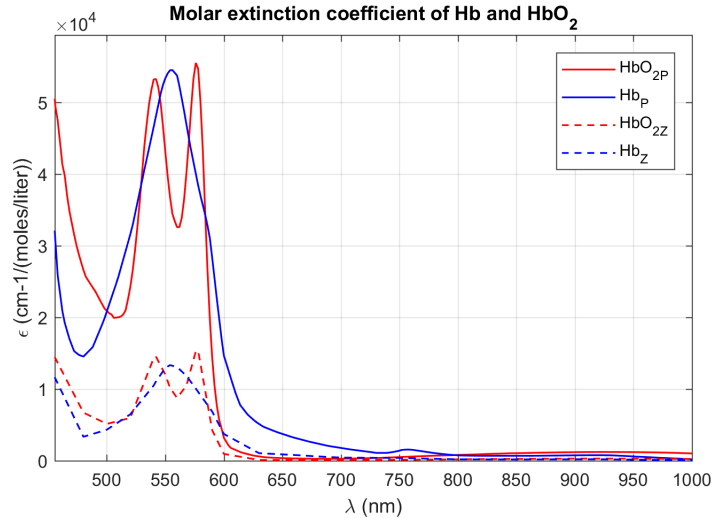


Figure 5.5: Experimental hemoglobin extinction coefficient obtained by Prahl and Zijlstra.

To obtain the extinction coefficients at each wavelength included in the hemoglobin spectra, comprised the ones not contained in the LED and Rainbow spectral responses, two approaches were considered.

The first applied method, to estimate the missing value of a certain extinction coefficient at a specific λ , consisted of the data interpolation of the normalized spectral

responses of the LED and the Rainbow, using the "interp1" Matlab[®] function.

Specifically:

- the spectral responses wavelengths, of the LED and of the Rainbow, defined the range of λ to consider in the extinction coefficients spectra;
- the extinction coefficients inside the λ range were extracted;
- to compute the final effective extinction coefficients, the values of the I_{norm} were interpolated for the wavelengths that are not present in the spectral characteristic of the LED (or Rainbow), obtaining the interpolated spectral characteristics. The "pchip" interpolation was utilized, because it preserves the shape of the function, by performing a cubic interpolation among the adjacent points.

Using this strategy, filling the spectral responses with the wavelengths of the extinction coefficients spectra, all the experimental extinction coefficients were considered and a better estimation of the ones was done.

On the other hand, the second approach consisted of the extinction coefficients interpolation, directly on the hemoglobin spectra. The λ range is defined, considering the common wavelengths values between the LED and Rainbow characteristics.

The corresponding extinction coefficients are extracted from the hemoglobin spectra and, in correspondence of the wavelength missing value, the ϵ were interpolated. The same Matlab[®] function and the same interpolation modality were employed.

This second method gives more importance to the spectral response of optical components (i.e. LED and Rainbow) than the first one, which gives more importance to the hemoglobin absorption spectra.

The comparison between the two approaches will be reported 6.

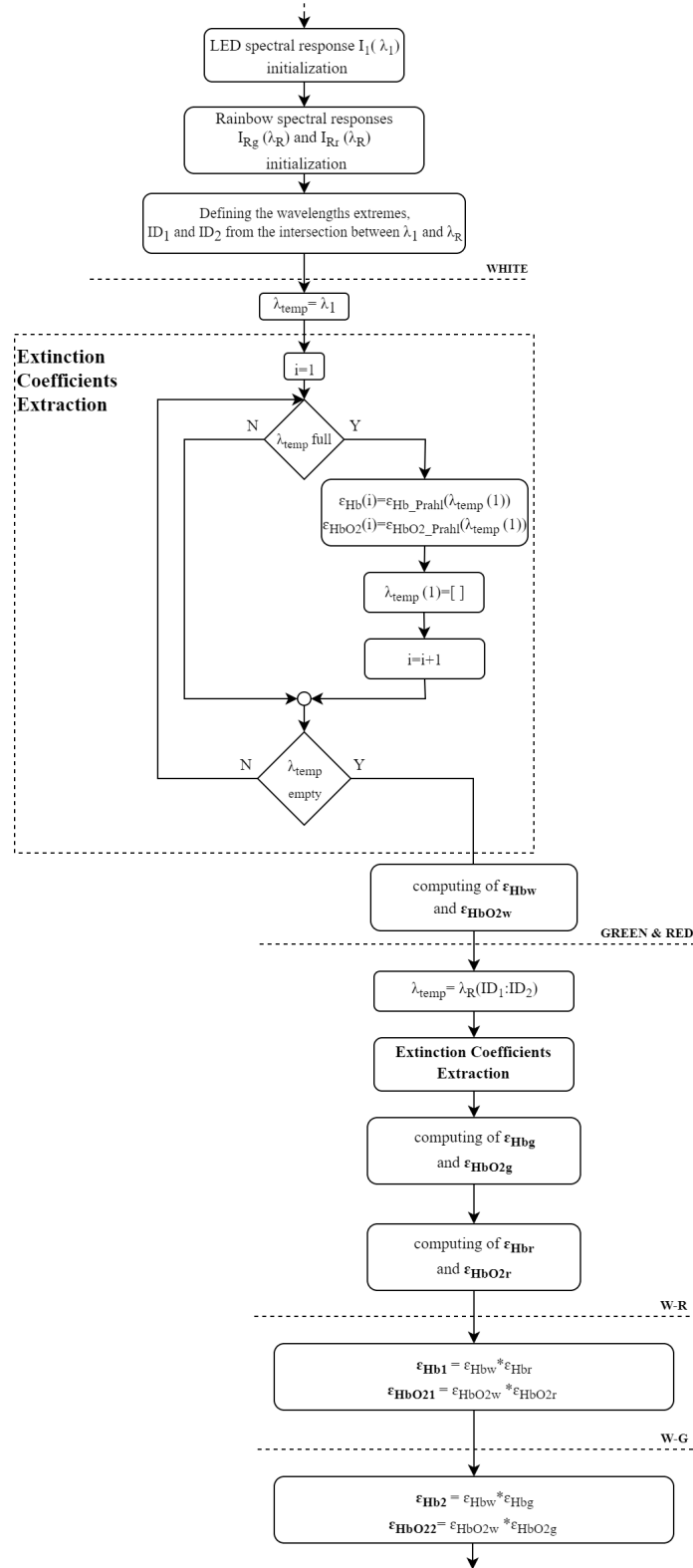


Figure 5.6: Representation of the effective extinction coefficients estimation. The W-R and W-G are the resulting overall extinction coefficients

5.2.1 VD6282 extinction coefficients evaluation

In the final part of this project, the updated version of the VD6281 was integrated in the system, the VD6282. To investigate also the Rainbow performance using the typical pulse oximeter wavelengths (i.e. red and IR), an IR LED was integrated in the measuring system. The effective extinction coefficients were computed, using the same procedure described above and considering the intersection between:

- the normalized intensity of the IR LED and the Rainbow VD6282 IR spectral response, for the IR wavelength;
- the normalized intensity of the white LED and the Rainbow VD6282 red spectral response, for the red wavelength.

Because the spectral sensor response is different than the VD6281 one, the effective extinction coefficients were recalculated also for the white LED and the red and green wavelengths.

The resulting wavelengths ranges were:

- 400-750 nm, considering the wavelength intersection between the white LED normalized intensity with the VD6282 spectral response;
- 820-920 nm, considering the wavelength intersection between the IR LED normalized intensity with the VD6282 spectral response.

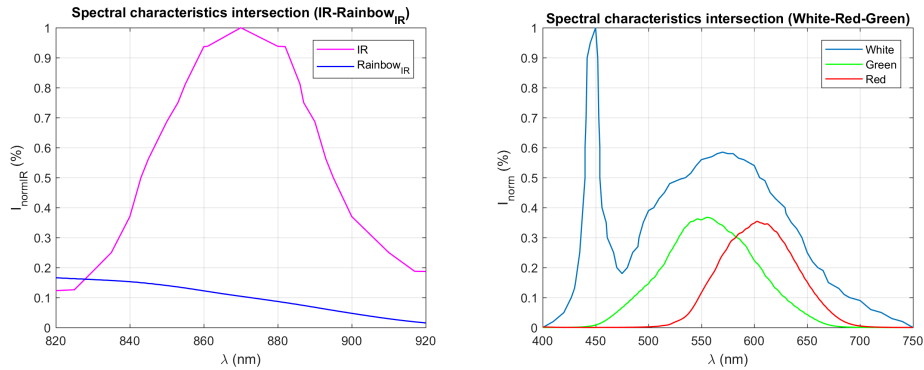


Figure 5.7: From left to right: In magenta the normalized intensity of the IR LED and in blue the VD6282 IR spectral response. In blue the normalized intensity of the white LED, in green and red the VD6282 green and red spectral responses.

The final extinction coefficients were calculated using the two methods.

5.3 Filter Design

The second phase of the algorithm consist of two filters implementation. They were employed to obtain the AC and DC signal components, necessary to compute the R parameter, ratio of the ratios between the alternate and continuous components of the signal, at the selected wavelengths. The filters designed in this work are applied in cascade at both the channels, i.e. green and red.

The implemented filters are the Finite Impulse Response (FIR) filters, with the order equal to 100. The FIR filter is a digital filter type, characterized by a finite duration of the impulse response.

Digital filters take a numerical input sequence $x(n)$ and produces a specific output $y(n)$, resulting from the convolution between the input sequence $x(n)$ and the system impulse response $h(n)$:

$$y(n) = x(n) * h(n - k) = \sum_{k=1}^N x(k) \cdot h(n - k) \quad (5.3)$$

In the Z-domain, the filter transfer function is polynomial and defined as:

$$H(z) = \frac{Y(z)}{X(z)} = \frac{N(z)}{D(z)} = \frac{b(1)z^0 + \dots + b(nb + 1)z^{-nb}}{1z^0 + \dots + a(na + 1)z^{-na}} \quad (5.4)$$

Where, $N(z)$ and $D(z)$ are the polynomials of na and nb order, composed by the a and b coefficients of the blocks present in the filter structure.

$H(z)$ is characterized by zeros and poles: the first can cancel the numerator (i.e. b) while the seconds can cancel the denominator (i.e. a).

FIR filters are defined as all-zero, non-recursive and moving average, they have order $na = 0$ at the denominator, thus $D(z) = 1$.

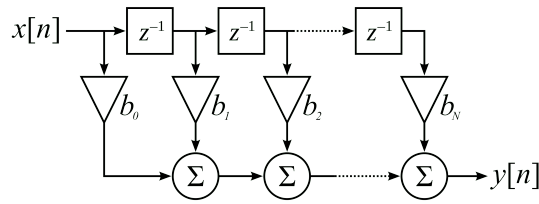


Figure 5.8: FIR filter design [84]

The FIR filter design is very advantageous for the real-time applications. Indeed, the FIR filter preserves the morphology of the biomedical signals, thanks to the linear phase of its transfer function and its stability.

Using the Infinite Impulse Response (IIR) filters the same results cannot be obtained, since their transfer function does not have a linear phase and they may not be stable. Indeed,

to maintain the signal morphology unaltered, the IIR filter is applied two times at the signal (i.e. forward-and-backward filtering). By doing so, the phase response is nullified and the amplitude response is aligned. The described procedure is not implementable in real-time but after the total signal acquisition, offline.

The major disadvantage of applying a FIR filter is that it requires high filter orders to achieve good filtering outputs, with respect to the order selected for the IIR filters. This results in:

- an increase in the computational time, since a greater number of filter banks to reach the set order is needed;
- a greater effect of the initial transient equal to the filter order, so the first sample properly filtered will be the (order+1)-th sample;
- a greater delay introduced by the transient in the filter, equal to order/2;

However, all the mentioned problems can be resolved, adopting appropriate algorithmic solutions.

For the present project, the chosen filters are:

- a band pass FIR filter (BPF), with cut-off frequency at 0.5 Hz and 5 Hz, to get the AC component;
- a low pass FIR filter (LPF), with a cut-off frequency at 0.05 Hz, to get the DC component.

As described in 1.3.2, the PPG frequency band is comprised between 0.01 - 8 Hz.

Regarding the BPF, the cut-off frequency was fixed by evaluating all the frequency content of the red and green signals acquired from 25 healthy subjects, during normal breathing phases and brief apnoea. Precisely:

1. the Fast Fourier Transform was computed, for each green and red signals of the 30 trials;
2. the Single-Sided Amplitude spectrum was obtained;
3. consulting the plot of (2), the higher frequency contributions were derived.

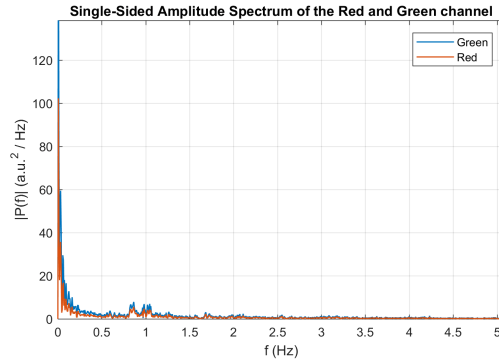


Figure 5.9: Single-Sided Amplitude Spectrum of the Red and Green channel of the Trial1.

All the analysed signal presented a frequency content of about 1-2 Hz, equivalent to 60-120 bpm, physiological values of the HR for subjects at normal conditions. To take into consideration higher HR, the upper cut-off frequency was set to 5 Hz, corresponding to 300 bpm. For this application, the lower cut-off frequency was established at 0.5 Hz, since the HR variations are included [35]. The resulting transfer function of the BPF is represented in the figure below:

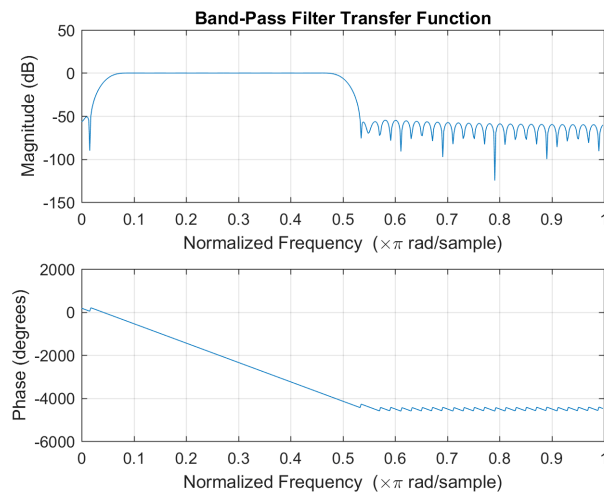


Figure 5.10: Magnitude and phase of the Band-Pass Filter transfer function, considering the cut-off frequency 0.5 and 5 Hz.

The LPF frequency was taken at 0.05 Hz, given that the LF band of the PPG signal goes from 0.04 to 0.15 Hz. Consequently, it was possible to extrapolate only the DC component, at 0.05 Hz. The resulting transfer function is:

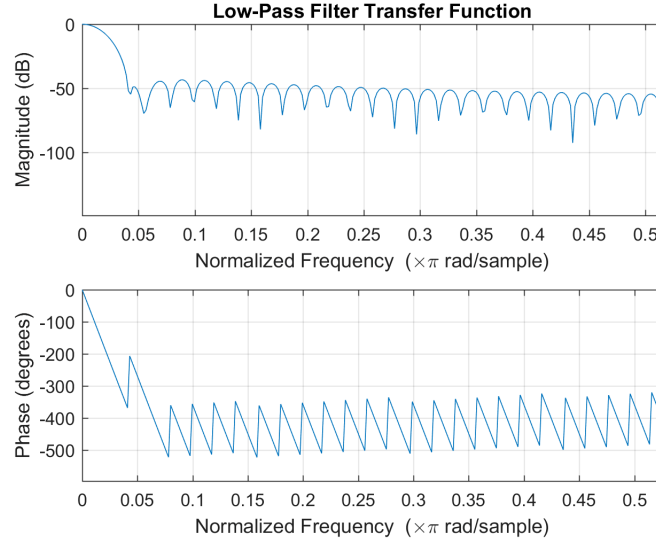


Figure 5.11: Magnitude and phase of the Low-Pass Filter transfer function, considering the cut-off frequency 0.05.

In figure 5.11 and 5.10 the frequency axes are normalized at the Nyquist frequency. The selected filters order for this work was 100, a good compromise between the computational time, the transitory losses and the introduced delay.

The designed BPF and LPF are based on a circular buffer loading. The filtered samples, indeed, are not collected until the circular buffer of the filter is not completely filled, which occurs at the iteration equal to the filter order. Thereby, the final obtained SpO₂ and HR data are not influenced by the initial transient.

When the buffer is completely charged, the filtered sample are acquired and stored. The band-pass filtered sample is equivalent to:

$$AC_{SIGNAL}(i) = \sum_{k=1}^{length_b} b_{AC}(k) \cdot buffer_c((length_b - k) + 1) \quad (5.5)$$

While the low-pass filtered sample is equivalent to:

$$DC_{SIGNAL}(i) = \sum_{k=1}^{length_b} b_{DC}(k) \cdot buffer_c((length_b - k) + 1) \quad (5.6)$$

In equations (5.5) and (5.6), $AC_{SIGNAL}(i)$ and $DC_{SIGNAL}(i)$ are the samples of the current iteration i -th, filtered from the BPF and LPF respectively. b_{AC} and b_{DC} are the filters coefficients of the BPF and LPF, respectively. Finally, the $buffer_c$ is the circular buffer contained the sampled acquired, that determines the amplitude of the i -th sample to filter, multiplying the correspondent FIR coefficient of the BPF and LPF. Its length is

equivalent to the filters order (i.e. $length_b$).

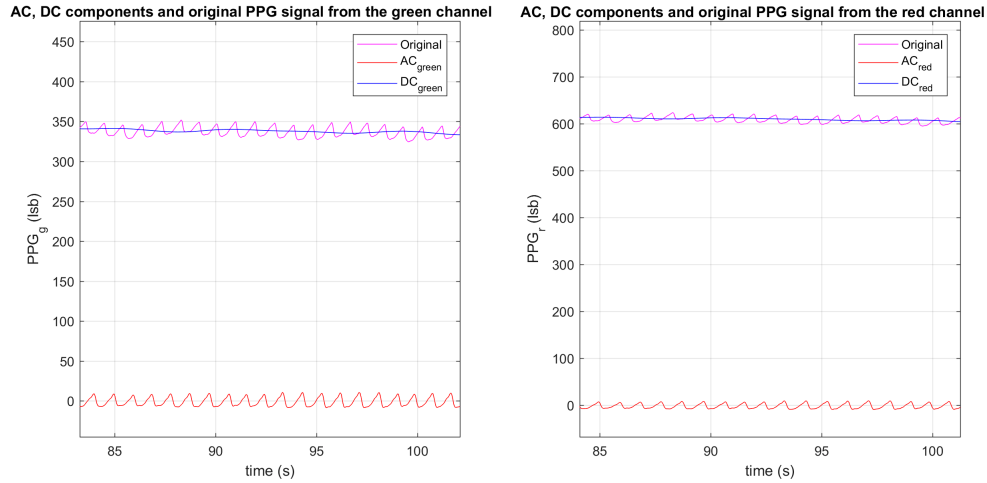


Figure 5.12: filtered Red and Green signals. Considering both the figure, the red waveform is the AC component, the blue is the DC component and the magenta is the original PPG signal.

When the filtering of the current sample is finished, the oldest sample of the circular buffer is eliminated, scaling the samples of the buffer by one location (the second sample became the first and so on). Thus, the incoming sample acquired is placed in the free position of the buffer (i.e. in the end) and the filtering process continues.

5.4 Peaks and minima detection

During the filtering phase, a certain number of filtered samples is stored in the system buffer. It is completely loaded if the number of the accumulated samples is equivalent to the selected length of the system buffer. When this happens, the process of peaks and minima detection begins and the SpO₂ can be calculated. The HR is derived by the distance between consecutive peaks.

The algorithm for the peaks and minima research has to be accurate, due to the physiological importance of the SpO₂ values. It is applied to the signals received in output from both the red and green channels.

The system buffer length is indicated in input of the algorithm, in this work it is fixed at 300 samples. The samples of the green and red signal are stored separately, particularly:

- the filtered green data by the BPF are stored in the defined buffer AC_g ;
- the filtered green data by the LPF are stored in the defined buffer DC_g ;
- the filtered red data by the BPF are stored in the defined buffer AC_r ;
- the filtered red data by the LPF are stored in the defined buffer DC_r .

When the vectors are full, they are investigated, for each initially established time interval. Thus, given the sampling frequency of the signal (i.e. f_s) and " n_{samp} " samples, the buffers are analysed, grouping together " $f_s \cdot n_{samp}$ " samples.

For this project, the time interval was set at 1s.

To describe the algorithm steps, the considered length of the system buffer and the time interval will be of 300 samples and 1s, respectively.

The peaks and minimum detection is realized on the AC_g and AC_r buffers, i.e. the AC components of the red and green signals. Their values are firstly scaled between 0 and 1, to simplify the signals content, implementing the min-max scaling:

$$AC_{gsca} = (AC_g - \min(AC_g)) / (\max(AC_g) - \min(AC_g)); \quad (5.7)$$

$$AC_{rsca} = (AC_r - \min(AC_r)) / (\max(AC_r) - \min(AC_r)); \quad (5.8)$$

where AC_{gsca} and AC_{rsca} are the re-scaled resulting green and red signals, while $\min(AC_g)$ and $\max(AC_g)$ and $\min(AC_r)$ and $\max(AC_r)$ are the absolute maximum and minimum values of the green and red signals, respectively.

Considering " i " as the algorithm iterations, it is composed of two main parts:

1. the analysis of the AC buffers for the first time, i.e. $i = length_{buffer} + order$;

$i = length_{buffer} + order$), the AC buffers are analysed from the 1-st second to the N-th second of the acquired samples.

The peaks detection is made, beginning from the 2-nd sample of the selected second.

Because of the PPG morphology, the current sample is a peak if it is contemporary higher than the previous and the next samples. If this condition is proved, the j-th sample and its position are memorized.

When at least two peaks are detected, another condition has to be verified, to evaluate if the stored peaks are signal real peaks. Indeed, the real peaks are near to the dicrotic notch or the other signal alterations, not completely deleted by the filtering. For this reason, these could be regarded erroneously as peaks.

The next requisite to be examined is based on the peaks position: considering a maximum HR of 180 bpm, corresponding to 3Hz in frequency, two consecutive peaks cannot be distant less than $f_s/3Hz$ samples. If the condition is true, the false peak to be deleted is the one with the lower amplitude. In figure 5.15, the flow chart of the peaks detection approach is reported. The procedure is effectuated both for the red and green signal.

At the end of the peaks detection, the minima are researched. The principle is determined based on the PPG morphology: the minimum is localized as the lowest value between two peaks, consequently samples included from one peak and the successive are considered. The correspondences maximum-minimum are obtained and the AC amplitudes are computed as the difference between consecutive peaks and minima. At this point, the R values and the SpO₂ can be estimated and memorized.

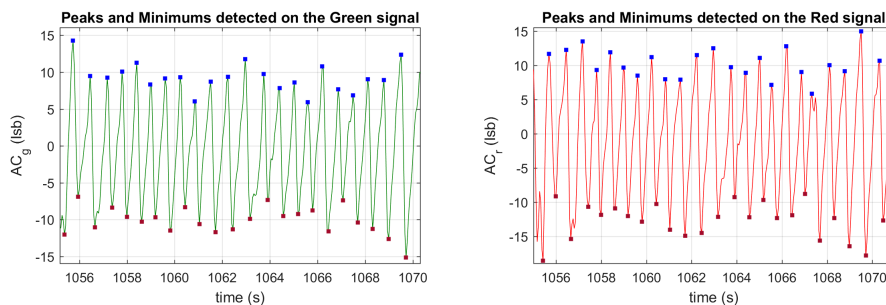


Figure 5.14: Detected peaks and minima on the green and red signals using the developed algorithm.

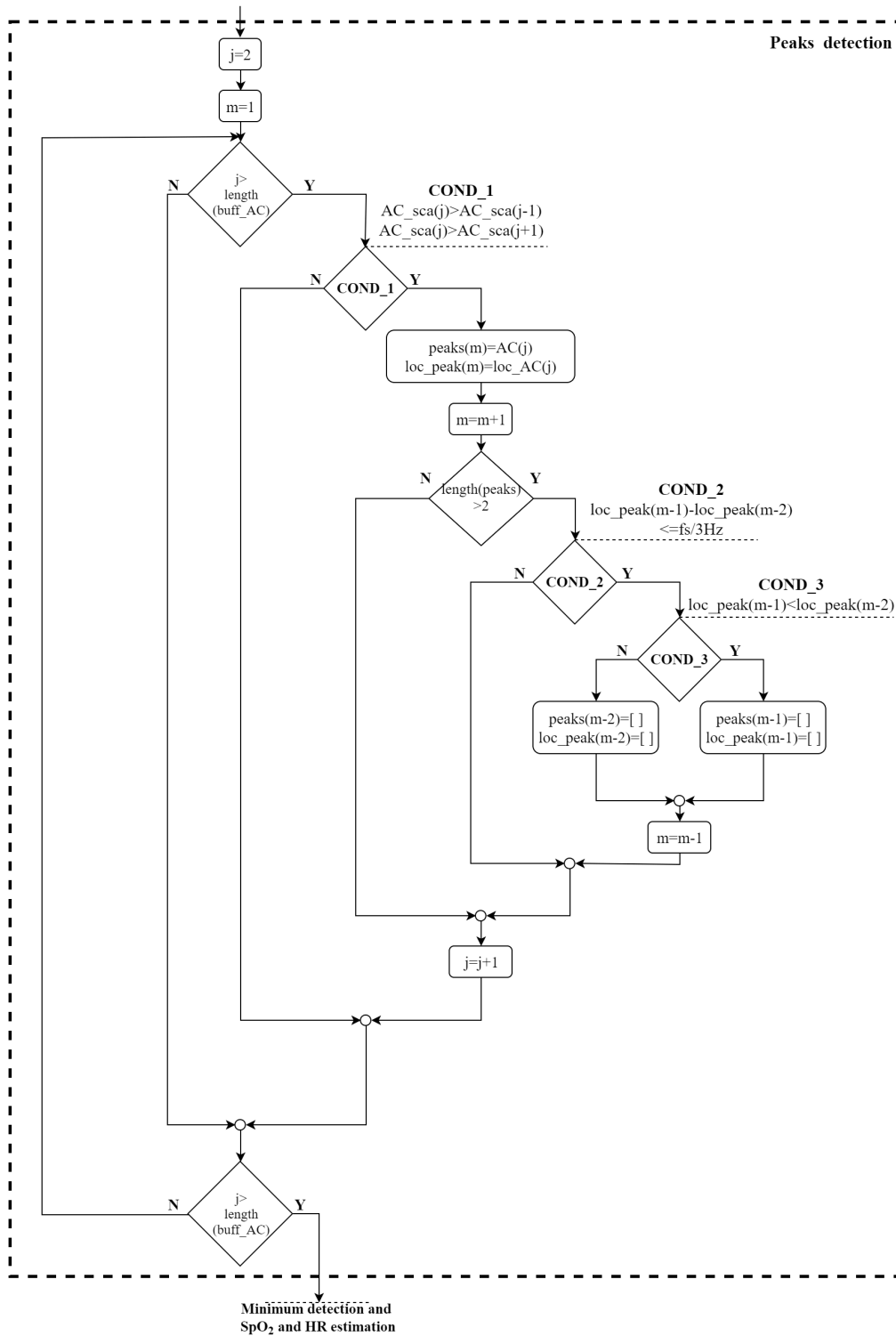


Figure 5.15: Peaks detection algorithm.

All the samples of the current seconds were therefore analysed and the next second

can be investigate, comprehending also the samples of the previous seconds.

In this way, the information contained in the first second are expanded by the ones present in the 2-nd time interval and so on, until the end of the AC buffers, when the resulting SpO₂ will contain the complete information.

In figure 5.16, the buffer analysis is graphically reported.

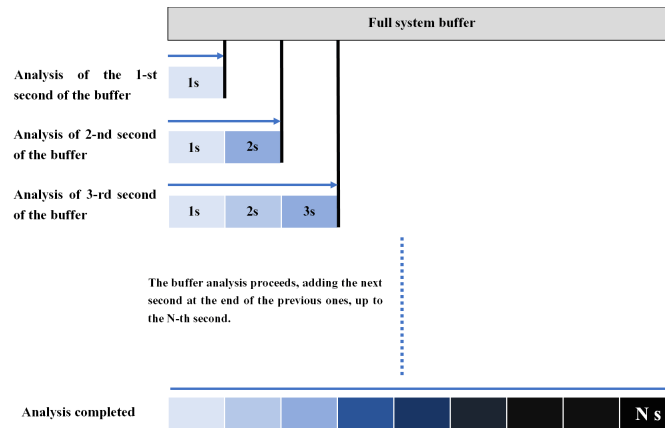


Figure 5.16: Representation of the first buffer analysis, second-by-second.

When the first analysis of the buffer is completed, the algorithm has to proceed with the signal acquisition and filtering.

In the next iterations (i.e. $i > length_{buffer} + order$) the first second of the buffer is deleted and the new second, (N+1)-th, will be located at the end of the buffer.

After one second of acquisition and filtering, the buffer will be already full, and the peaks and minima detection restarts.

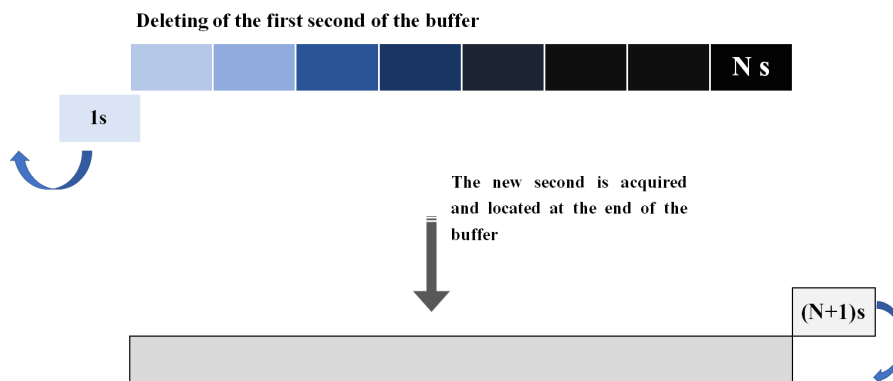


Figure 5.17: Deleting of the oldest buffer second and arriving of a new second.

As long as new samples incoming, the buffer loading continues according to this procedure, updating the system buffer content with the most recent second.

5.5 Oxygen Saturation and Heart Rate estimation

The SpO₂ and HR are obtained immediately after the peaks and minima detection.

The SpO₂ is calculated from the Lambert-Beer equation, as a function of the effective extinction coefficients, attained in 5.2, and the R parameter. The R ratio, at this point, can be estimated as:

$$\frac{(AC_g/DC_g)}{(AC_r/DC_r)} \quad (5.9)$$

Where, AC_g and DC_g are the AC and DC components of the green signal, while AC_r and DC_r are the ones of the red signal.

To compute the R ratio, the ratios between the components of the signal are separately obtained. Therefore, the R_g and the R_r result from the following steps:

1. calculation of the AC amplitudes for both the channels, as the difference between consecutive measured peaks and minima;
2. taking the samples on the DC component, in correspondence of the positions interval between the peak and the minimum;

In this way, the R_g and R_r are evaluated as:

$$R_g(k) = \frac{peak_g(k) - min_g(k)}{mean(DC_g(loc_{peak_g}(k) : loc_{min_g}(k)))} \quad (5.10)$$

$$R_r(k) = \frac{peak_r(k) - min_r(k)}{mean(DC_r(loc_{peak_r}(k) : loc_{min_r}(k)))} \quad (5.11)$$

Where, *peak* and *min* are the values of the k-th peak and minimum, while the denominator is the mean value of the DC component, considering the positions interval comprised between the k-th peak and minimum.

The total R ratio is:

$$R = \frac{mean(R_r)}{mean(R_g)} \quad (5.12)$$

Equivalent to the average R ratio in the considered second.

When the R ratio is attained, the SpO₂ relation is completed and by means of the Lambert-Beer relation, the SpO₂ of the current second is estimated.

The HR is computed after 10s of acquisition, because a certain number of peaks are requested to evaluate a trustworthy cardiac frequency. The signal used to the HR implementation is taken from the green channel, because it better perceives the HR variations than the red signal.

The HR is equivalent to:

$$H_R(k) = \frac{fs}{locs_{peak}(k+1) - locs_{peak}(k)} \cdot 60bpm \quad (5.13)$$

From the equation (5.13), the instantaneous frequency is determined, that is the correspondent frequency for each the distances peak-to-peak.

The final HR is the mean value of the instantaneous frequency in the considered second. At the end of the SpO₂ and HR computing, their values are reported for each seconds of the acquisition.

In figure 5.18, the minima detection and the SpO₂ and HR calculation method are reported. The same steps are followed to estimate the parameter in the two color channel.

5.6 VD6281 and VD6282 Calibration

This is the last experimental phase, consisting on the VD6281 calibration first. Afterward, the calibration of the VD6282 is made in the same way.

The calibration process permits to extract the experimental relation between the R ratio and the SpO₂. Typically, this procedure is carried out using spectrometric measurements on blood samples, parallel to the pulse oximeter acquisition. In this way, the correspondences R ratio - SaO₂ are evaluated: the first is acquired using the PO to calibrate and the second is acquired from the spectrometer.

In this experimental work, the calibration is implemented on the data acquired in parallel from the sensor VD6281 and a reference device, the Onyx 9560.

The performed steps for the calibration process are:

1. calculate the R ratio, using the implemented algorithm;
2. contemporary acquire the SpO₂ and the HR from the reference device;
3. obtain the scatter plot of the SpO₂ and the R ratio, to observe the relation between the quantities;
4. from (3), the linear and quadratic experimental regression are extracted;
5. by means of the relation, the linear and quadratic coefficients are used to compute the Rainbow SpO₂.

The procedure is repeated for all the trials and the coefficients of the linear and quadratic regression are collected.

The final calibration coefficients are the mean value of the coefficients of each acquisition and they are employed for the VD6281 SpO₂ final values.

The relations types are:

$$SpO_2 = A \cdot R^2 + B \cdot R + C \quad (5.14)$$

$$SpO_2 = D \cdot R + E \quad (5.15)$$

The reported relations are the quadratic and the linear regression respectively, where A , B and C are the second degree experimental coefficients, while D and E are the resulting first degree experimental coefficients.

In the same way, the calibration of the VD6282 is realized.

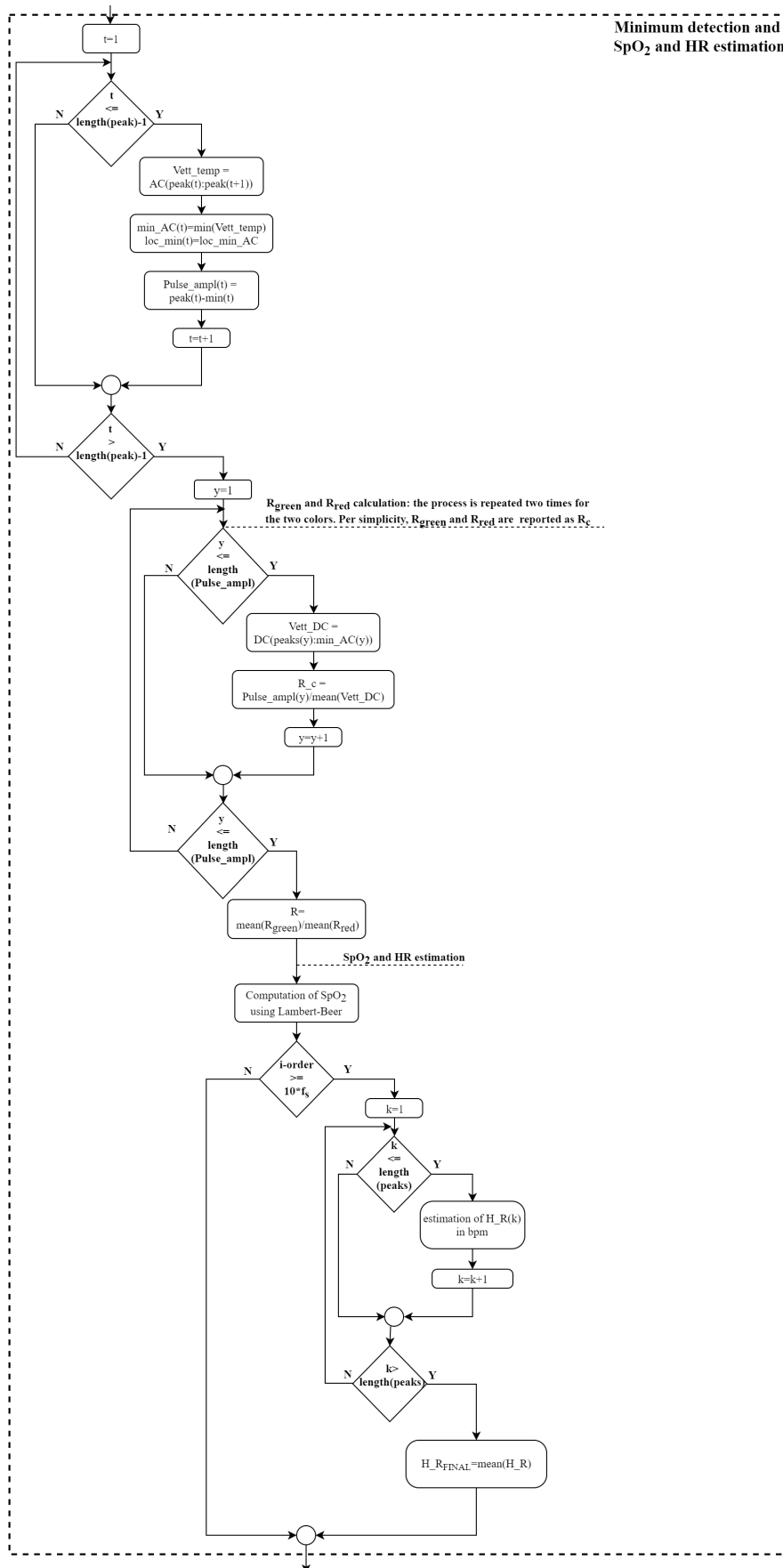


Figure 5.18: minima detection and SpO₂ and HR estimation.

Part III
Results

Chapter 6

Statistical Assessment

Statistical parameters were calculated to evaluate the algorithm performances.

The approach consisted of:

1. the offset determination between the Onyx 9560 SpO₂ and the one computed with the Lambert-Beer equation;
2. the calibration of the VD6281 and the VD6282, by means of the regression analysis;
3. the estimation of the HR and SpO₂ percentage error and the relative accuracy, given the PPG signals at the green, red and infrared wavelengths;
4. the manual validation of the peaks and minimums detection algorithm, using true positive (TP), true negative (TN), false positive (FP) and false negative (FN) parameters. The final Sensitivity (SE) and (PPV) were also computed.

Data were extracted considering the Onyx 9650 as reference device. The employed statistical methods are described briefly below.

6.1 Regression analysis

The calibrations of the pulse oximeter prototypes, where the VD6281 and VD6282 multispectral sensors were integrated, were effectuated to estimate their instrumental characteristics. The process allowed to obtain values of SpO₂ in a more correct range than the ones from the Lambert-Beer equation, based only on the R ratio and the molar extinction coefficients, at the selected wavelengths.

Generally, calibration procedure is realized considering the relation between a data set acquired from the reference calibrated device and a data set obtained from the experimental device. In the present work, the first is the Onyx 9560, while the second are the Rainbow sensors.

One of the methods employed is the regression analysis: using the scatter plot, the regression analysis permits to observe how a dependent variable Y is related to an independent variable X. The distribution of the data in the Cartesian Plane can be interpolated with a linear regression. However, if the data does not present a simple linear relation, the data interpolation can be polynomial.

In the present work, both the linear and the quadratic interpolation were extracted from the scatter plot between the Y data, i.e. the Onyx SpO₂ values, and the X data, i.e. the R ratio obtained from the algorithm.

The linear and the quadratic data interpolation are respectively:

$$Y = a \cdot X^2 + b \cdot X + c \quad (6.1)$$

$$Y = d \cdot X + e \quad (6.2)$$

Where, each coefficient (i.e. a, b, c, d and e) is obtained with the data interpolation.

In section 7.2, the scatter plot of the Onyx SpO₂ and the Rainbow R ratio are reported.

6.2 Percentage error and the relative accuracy

The percentage error is reported to appraise how much the measured value is different from the real value. It is estimated as:

$$e_i[\%] = \frac{|x_i - y_i|}{x_i} \cdot 100\% \quad (6.3)$$

Where:

- i is the i-th considered sample;
- x_i is the reference value, obtained by the Onyx (i.e. the HR or the SpO₂).
- y_i is the measured value, estimated from the Rainbow (i.e. the HR or the SpO₂);

From the (6.3), the mean relative error is computed as:

$$MRE[\%] = \frac{1}{N} \sum_{i=1}^N e_i \quad (6.4)$$

The MRE is the mean value of the percentage errors estimated for a set of measurements.

The relative accuracy is also evaluated as:

$$ACC[\%] = \frac{1}{N} \sum_{i=1}^N \frac{|x_i - |x_i - y_i||}{x_i} \cdot 100\% \quad (6.5)$$

It is a further assessment of the proximity between the experimental data and the reference data. The accuracy indicates the correspondence between the theoretical data, collected with a series of acquisitions, and the real data.

6.3 Peaks and minimums validation

The validation of the peaks and minimums algorithm is realized by manual researching of real peaks and minimums, for each of the collected signal.

Determined all the peaks and minimums, the evaluated parameters were:

- True Positive, **TP**, number of point correctly identifies as peaks or minimums.
- False Positive, **FP**, number of false detected peaks or minimums.
- True Negative, **TN**, number of data that correctly are not taken as peaks or minimums.
- False Negative, **FN**, number of data that are peaks or minimums but the algorithm does not recognize them.

Considering the described values, the Sensitivity and the Positive Predicted Value were calculated:

$$SE = \frac{TP}{TP + FN} \quad PPV = \frac{TP}{TP + FP} \quad (6.6)$$

The *sensitivity* is the percentage of the correctly identified **TP**, while the *PPV* is the probability that a sample, detected as peak (or minimum), is really a peak (or a minimum). These values influence the final HR estimation: the lower percentage of SE and PPV means that a lot of FP are detected and, consequently, the HR will increase. The parameters were evaluate because the present algorithm is more susceptible to the FP detection.

Chapter 7

SpO₂ Measurements

7.1 Extinction Coefficients Interpolation

As described in the paragraph 5.2, the first carried out evaluation was the selection of the better experimental extinction coefficients, considering the data from Prahl and Zijlstra.

The resulting SpO₂, compared with the Onyx 9560 saturations, are reported in figures 7.1 and 7.2, for two acquired signals from the VD6281 and the VD6282.

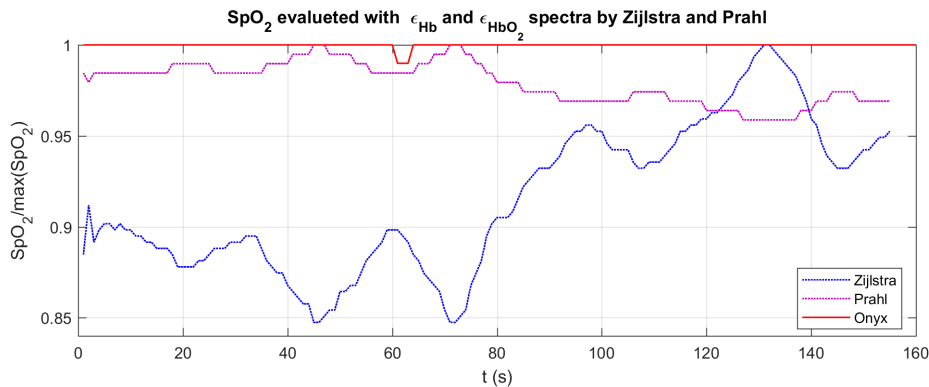


Figure 7.1: Comparison among the SpO₂ obtained by the Onyx and the one by the Prahl and Zijlstra ϵ data. SpO₂ is estimated using a signal acquired from the VD6281, in normal respiratory condition (no apnea).

In figures, the estimated SpO₂ values are re-scaled in the range [0 1], to directly compared the results.

Observing the obtained SpO₂, the Prahl extinction coefficients return in a more correctly SpO₂ trend, respect the one from the Zijlstra extinction coefficients.

Moreover, the SpO₂ computed using the Zijlstra ϵ has negative values for all the analyzed trials, while the Prahl solution presents always positive SpO₂ values, with an offset of about 100, from the reference Onyx SpO₂.

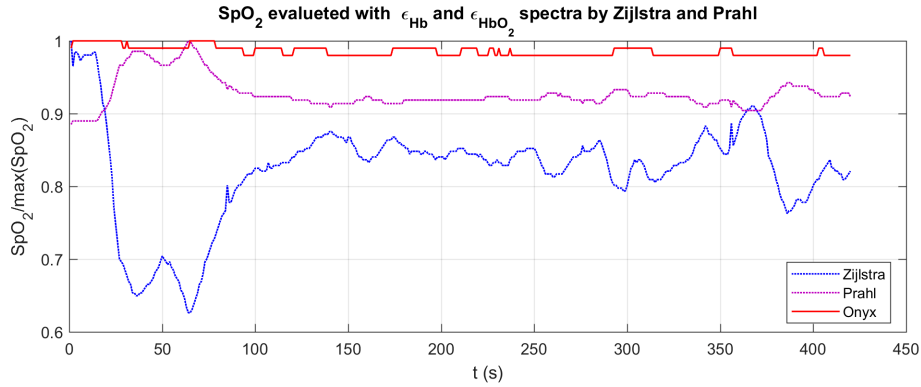


Figure 7.2: Comparison among the SpO₂ obtained by the Onyx and the one by the Prahl and Zijlstra ϵ data. SpO₂ is estimated using a signal acquired from the VD6282, in normal respiratory condition (no apnea).

Therefore, in this work, the Prahl coefficients were considered to evaluate the SpO₂. Chosen the extinction coefficients, the assessments were done considering both the implemented interpolation methods.

7.1.1 Normalized Spectral Intensity interpolation

The intensity interpolations of each spectral responses of the employed optical elements (i.e. white LED, VD6281, VD6282 and IR LED) are reported in figures 7.3, 7.4, 7.5 and 7.6.

The wavelengths range and the corresponding I_{norm} , utilized for the evaluation of the final effective extinction coefficients, results from the intersection among the hemoglobin spectra and the optical elements.

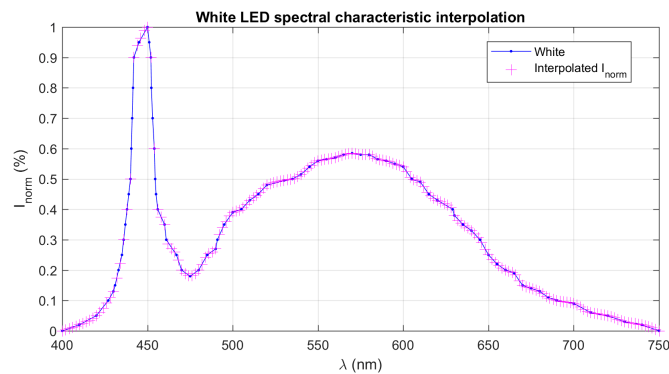


Figure 7.3: Interpolation of the normalized spectral intensity of the white LED, considering the Prahl wavelengths included in the LED wavelengths range [400-750 nm].

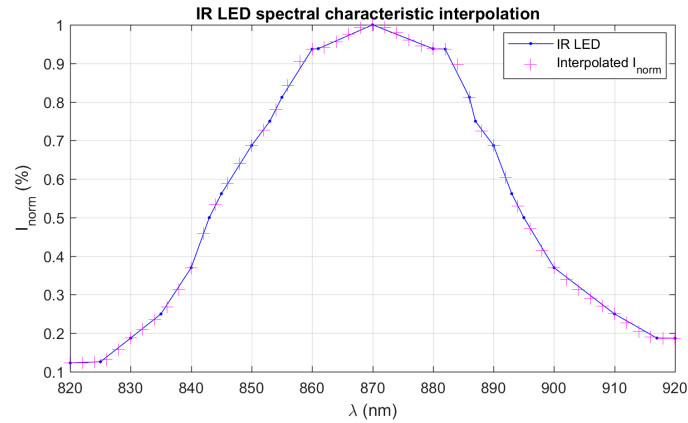


Figure 7.4: Interpolation of the normalized spectral intensity of the IR LED, considering the Prahl wavelengths included in the LED wavelengths range [820-920 nm].

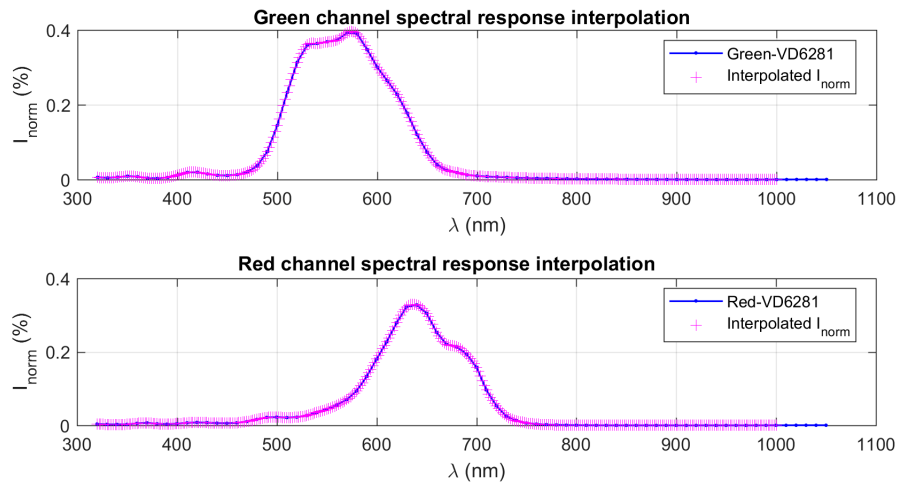


Figure 7.5: Interpolation of the normalized spectral intensity of the VD6281 green and red channels, considering the Prahl wavelengths included in the Rainbow wavelengths range [320-1050 nm].

The '+' symbols correspond to the interpolated I_{norm} . They are computed at the wavelengths values contained in the vector of the hemoglobin spectra and not necessarily present in the spectra of the optical elements, in the same range.

It have to consider that: with this interpolation method, the I_{norm} of the LED and Rainbow, at the λ values not present in the hemoglobin spectra, will be not taken into account for the final extinction coefficients estimation (\cdot symbols).

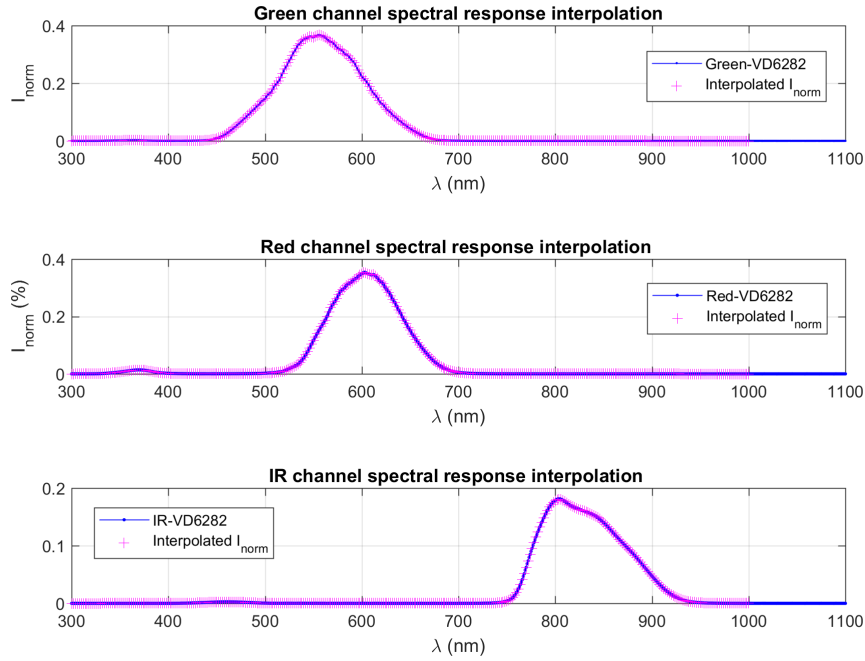


Figure 7.6: Interpolation of the normalized spectral intensity of the VD6282 green, red and IR channels, considering the Prahl wavelengths included in the Rainbow wavelengths range [320-1100 nm].

The resulting extinction coefficients, obtained for this first case, are reported in the tables below.

VD6281

	ϵ_{Hb}	ϵ_{HbO_2}
Red _{VD6281}	$1.37 \cdot 10^3$	913.29
Green _{VD6281}	$4.96 \cdot 10^3$	$4.28 \cdot 10^3$
White _{LED}	$1.98 \cdot 10^4$	$1.15 \cdot 10^4$
Overall extinction coefficients		
RED	$2.73 \cdot 10^7$	$1.05 \cdot 10^7$
GREEN	$9.84 \cdot 10^7$	$4.91 \cdot 10^7$

Table 7.1: Final effective extinction coefficients resulting from the I_{norm} interpolation of the White and the VD6281 channels.

VD6282

	ϵ_{Hb}	ϵ_{HbO_2}
Red _{VD6282}	$1.87 \cdot 10^3$	$1.38 \cdot 10^3$
Green _{VD6282}	$3.75 \cdot 10^3$	$3.30 \cdot 10^3$
IR _{VD6282}	70.65	106.66
White _{LED}	$1.98 \cdot 10^4$	$1.15 \cdot 10^4$
IR _{LED}	392.55	613.15
Overall extinction coefficients		
RED	$3.71 \cdot 10^7$	$1.59 \cdot 10^7$
IR	$2.77 \cdot 10^4$	$6.53 \cdot 10^4$
GREEN	$7.44 \cdot 10^7$	$3.79 \cdot 10^7$

Table 7.2: Final effective extinction coefficients resulting from the I_{norm} interpolation of the IR LED, the White and the VD6282 channels.

7.1.2 Hemoglobin spectra interpolation

The second method to compute the effective extinction coefficients is based on the interpolation of the hemoglobin extinction coefficients, directly on the Hb and HbO₂ spectra, considering the wavelength range of the white LED, IR LED and the Rainbow sensors (i.e. VD6281 and VD6282).

The interpolated extinction coefficients are reported in figures 7.7 and 7.8.

In this case, the wavelengths ranges were the intersection between the spectral responses of the optical elements:

- the White and VD6281 intersection includes the λ from 400 up to 750 nm, for the green and red wavelengths;
- the White and VD6282 intersection includes the λ from 400 up to 750 nm, for the green and red wavelengths;
- IR LED and the IR channel intersection includes the λ from 820 up to 920 nm, for the IR wavelength.

The extinction coefficients values, not presented in the spectra at a certain λ , were interpolated.

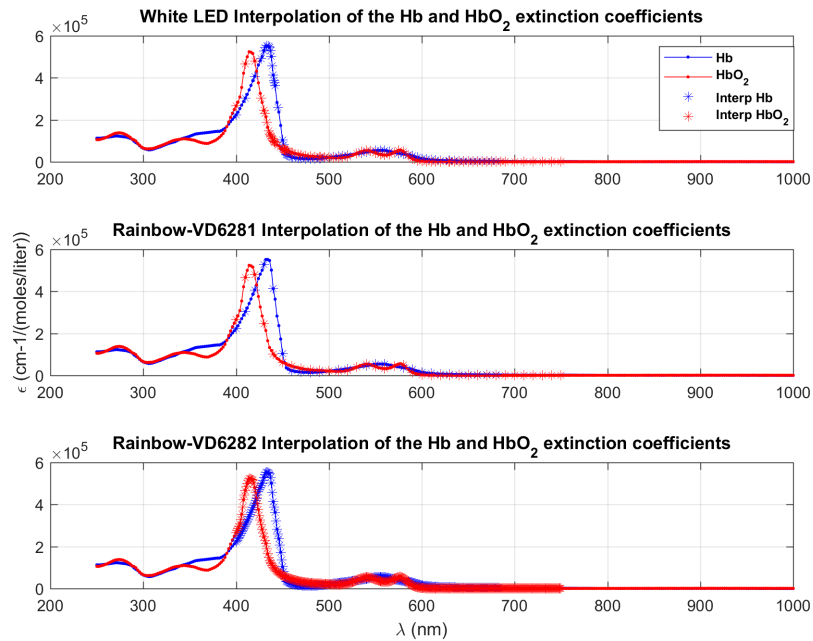


Figure 7.7: Interpolation of Hb and HbO₂ molar extinction coefficients, considering the wavelength range [400-750 nm] of the white LED, the Rainbow VD6281 and the Rainbow VD6282.

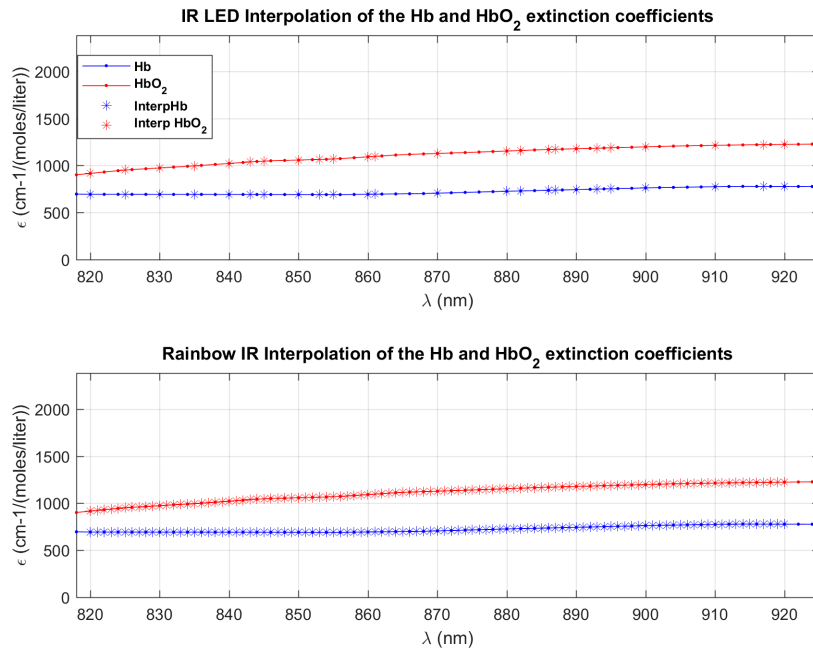


Figure 7.8: Interpolation of Hb and HbO₂ molar extinction coefficients, considering the wavelength range [820-920 nm] of the IR LED and the Rainbow VD6282.

The effective extinction coefficients are reported in the following tables.

VD6281

	ϵ_{Hb}	ϵ_{HbO_2}
Red _{VD6281}	$1.35 \cdot 10^3$	908.66
Green _{VD6281}	$4.86 \cdot 10^3$	$4.23 \cdot 10^3$
White _{LED}	$4.53 \cdot 10^4$	$1.98 \cdot 10^4$
Overall extinction coefficients		
RED	$6.12 \cdot 10^7$	$1.79 \cdot 10^7$
GREEN	$2.21 \cdot 10^8$	$8.32 \cdot 10^7$

Table 7.3: Final effective extinction coefficients of the White LED and the Rainbow VD6281, resulting from the ϵ_{Hb} and ϵ_{HbO_2} interpolation on the hemoglobin spectra.

VD6282

	ϵ_{Hb}	ϵ_{HbO_2}
Red _{VD6282}	$1.88 \cdot 10^3$	$1.31 \cdot 10^3$
Green _{VD6282}	$3.76 \cdot 10^3$	$3.31 \cdot 10^3$
IR _{VD6282}	70.72	106.87
White _{LED}	$4.55 \cdot 10^4$	$1.97 \cdot 10^4$
IR _{LED}	400.89	624.74
Overall extinction coefficients		
RED	$8.54 \cdot 10^7$	$2.73 \cdot 10^7$
GREEN	$1.71 \cdot 10^8$	$6.52 \cdot 10^8$
IR	$2.84 \cdot 10^4$	$6.68 \cdot 10^4$

Table 7.4: Final effective extinction coefficients of the White LED, the IR LED and the Rainbow VD6282, resulting from the ϵ_{Hb} and ϵ_{HbO_2} interpolation on the hemoglobin spectra.

Both the implemented interpolation methods were utilized for the SpO₂ computing and their performances were evaluated.

7.2 Offset Correction and Regression Analysis

After the extinction coefficients estimation, the SpO₂ values were computed:

1. for the 15 trials acquired with the VD6281, where the white LED and the green and red channels of the sensor were utilized, so the green and red wavelengths were considered;

2. for the 9 trials acquired with the VD6282, where the white and IR LEDs and the green, red and IR channels of the sensor were utilized, and the final green and red SpO₂ were compared with the red and IR SpO₂.

The SpO₂ was calculated by the **Lambert-Beer equation** and the interpolation obtained by the **regression analysis**.

7.2.1 Offset correction

The Lambert-Beer equation depends from the extinction coefficients and the R ratio. A first calibration procedure was apply directly on the Lambert-Beer results. Specifically, during the signal analysis, the SpO₂ resulting from the output of the Rainbow sensors, differed from the Onyx SpO₂ of a constant offset, for all the trials. The relation considered for the parameter correction is:

$$SpO_2 = SpO_{2LB} - q \quad (7.1)$$

Where, SpO_{2LB} is obtained from the Lambert-Beer relation and q is the constant offset, present on the sensor output values. Therefore, the procedure consisted in subtracting the same offset to all the Rainbow SpO₂ obtained.

For each the trials, the offset was calculated as the difference between the mean value of the Rainbow SpO₂ and the mean value of the concurrent Onyx SpO₂.

The final considered offset was the average of all the computed ones:

1. 180.87, for the SpO₂ of the VD6281, considering the I_{norm} interpolation for the ϵ assessment;
2. 93.94, for the SpO₂ of the VD6281, considering the interpolation of the ϵ_{Hb} and ϵ_{HbO_2} in the hemoglobin spectra;
3. 208, for the SpO₂ of the VD6282, considering the I_{norm} interpolation for the ϵ assessment;
4. 103, for the SpO₂ of the VD6282, considering the interpolation of the ϵ_{Hb} and ϵ_{HbO_2} in the hemoglobin spectra;

As can be noticed, for both the VD6281 and VD6282, the second interpolation method (i.e. ϵ_{Hb} interpolation) introduced a lower offset than the first one (I_{norm}).

The SpO₂ trends of the collected trials are reported, considering the two interpolation methods, firstly for the VD6281 and then for the VD6282.

VD6281

The SpO₂ reported in figures, were estimated using the extinction coefficients resulting from the I_{norm} interpolation of the optical elements, using the red and green overall extinction coefficients reported in table 7.1.

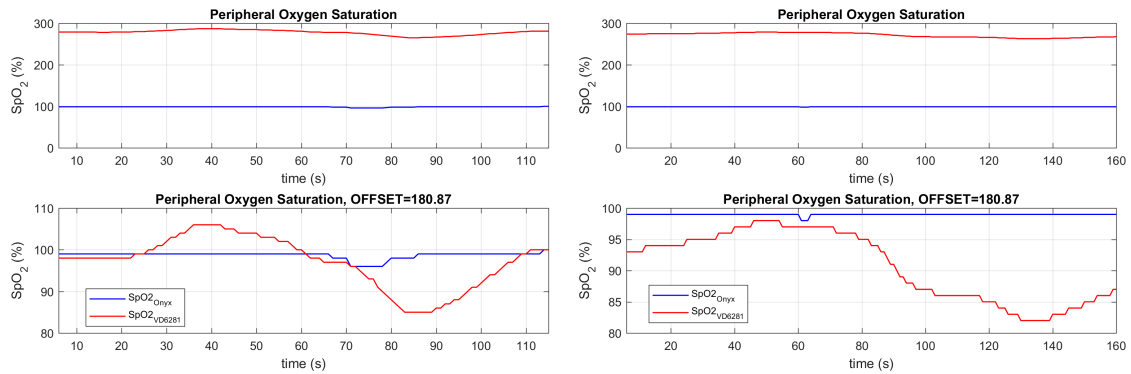


Figure 7.9: Offset correction of the trial 7 (on the left) and the trial 9 (on the right).

The MRE and the ACC, calculated for the 15 trials, are reported below.

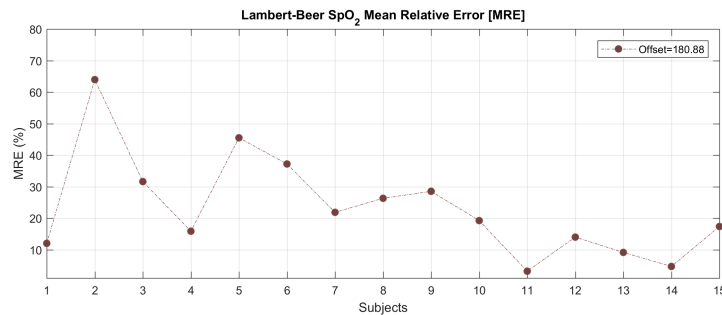


Figure 7.10: MRE of the SpO₂ estimations, using the I_{norm} interpolation method

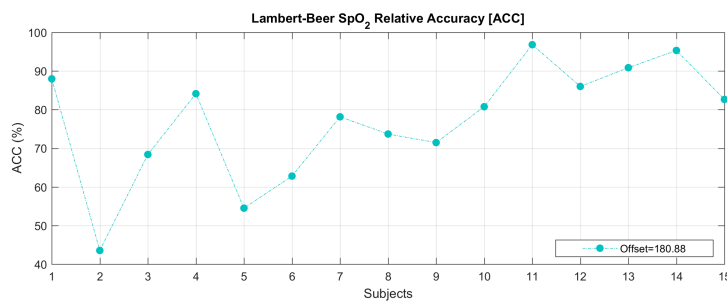


Figure 7.11: ACC of the SpO₂ estimations, using the I_{norm} interpolation method

The SpO₂ reported in the subsequent figures, were estimated using the extinction coefficients resulting from the hemoglobin spectra interpolation, using the red and green overall extinction coefficients reported in table 7.3.

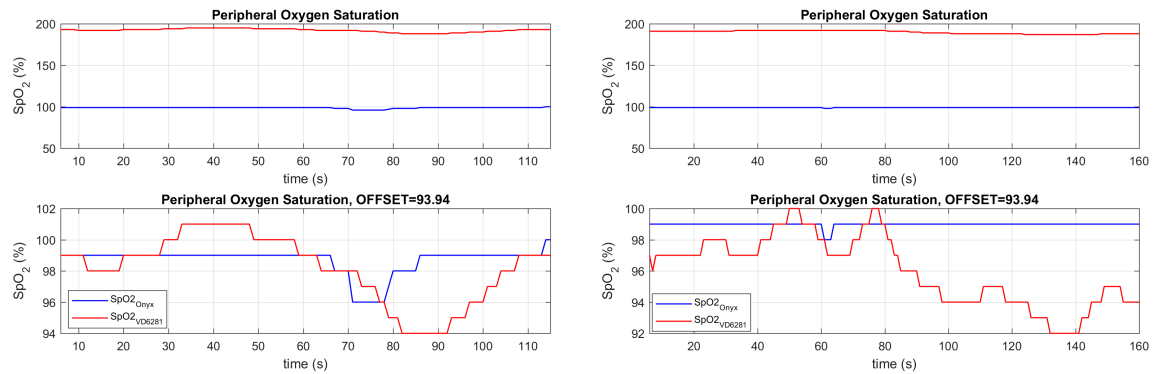


Figure 7.12: Offset correction of the trial 7 (on the left) and the trial 10 (on the right).

The MRE and the ACC, calculated for the 15 trials, are reported below.

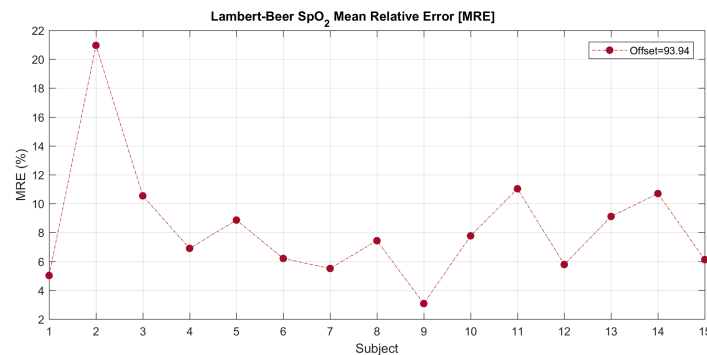


Figure 7.13: MRE of the SpO₂ estimations, using the ϵ_{Hb} and ϵ_{HbO_2} interpolation method

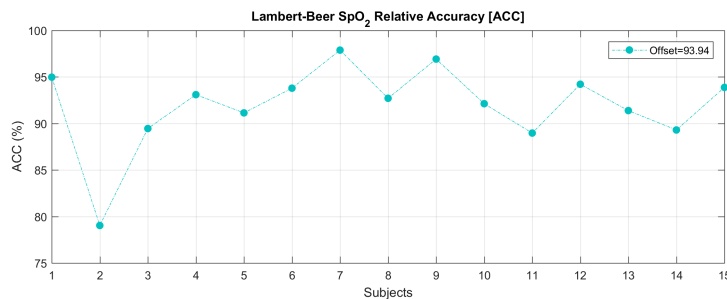


Figure 7.14: ACC of the SpO₂ estimations, using the ϵ_{Hb} and ϵ_{HbO_2} interpolation method

VD6282

The SpO₂ reported in figures, were estimated using the extinction coefficients resulting from the I_{norm} interpolation of the optical elements, using the red and green overall extinction coefficients reported in table 7.2. For these signal, also the IR SpO₂ is reported for comparison.

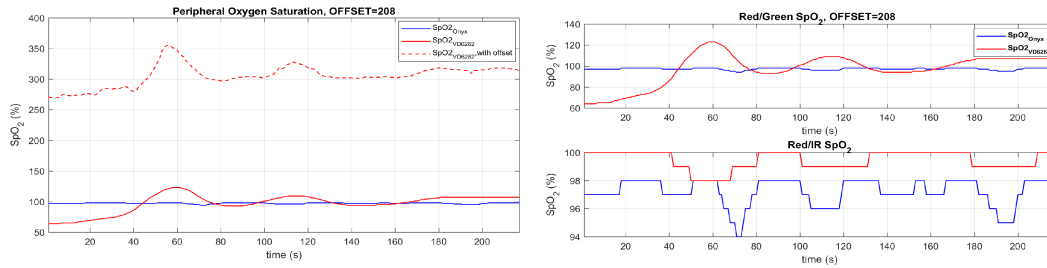


Figure 7.15: Offset correction of the trial 11 (on the left). On the right, the comparison between the same SpO₂, calculated with the red and green wavelengths and the red and IR ones, are reported.

The MRE and the ACC, calculated for the 9 trials, are reported below.

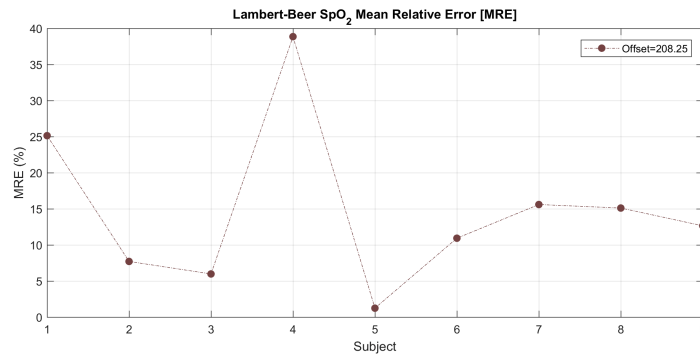


Figure 7.16: MRE of the SpO₂ estimations, using the I_{norm} interpolation method

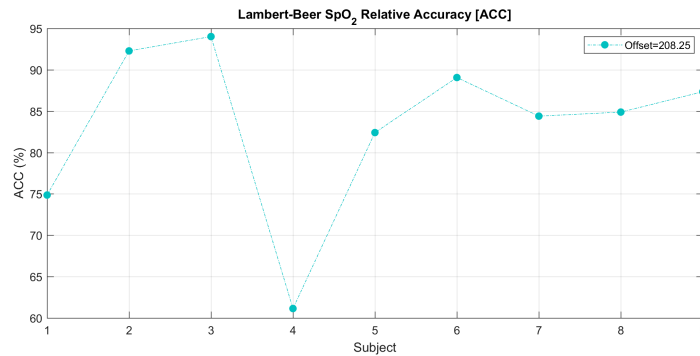


Figure 7.17: ACC of the SpO₂ estimations, using the I_{norm} interpolation method

The SpO₂ reported in the subsequent figures, were estimated using the extinction coefficients resulting from the ϵ_{Hb} and ϵ_{HbO_2} interpolation, using the red and green overall extinction coefficients reported in table 7.4. For these signal, also the IR SpO₂ is reported for comparison.

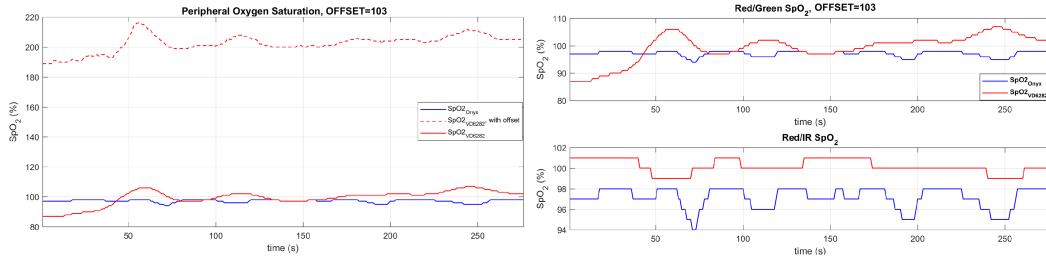


Figure 7.18: Offset correction of the trial 11 (on the left). On the right, the comparison between the same SpO₂, calculated with the red and green wavelengths and the red and IR ones, are reported.

The MRE and the ACC, calculated for the 9 trials, are reported.

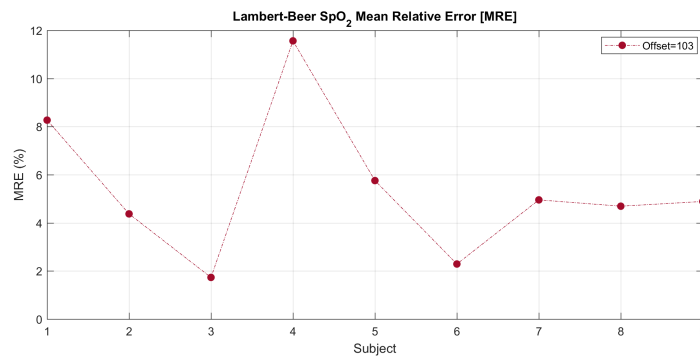


Figure 7.19: MRE of the SpO₂ estimations, using the I_{norm} interpolation method

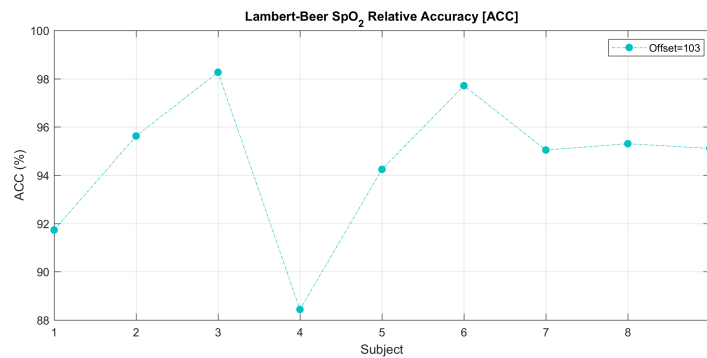


Figure 7.20: ACC of the SpO₂ estimations, using the I_{norm} interpolation method, considering the final results of both the sensors.

In the tables 7.5 and 7.6, the ACC and MRE ranges of both the sensors, relative

to the interpolation methods, are reported. It can be deduced that the SpO₂, resulting from the hemoglobin spectra interpolation, returns in more reasonable values in terms of the mean MRE ($MRE_{VD6281}=8.33\%$ and $MRE_{VD6282}=5.39\%$) and the mean ACC ($MRE_{VD6281}=91.93\%$ and $MRE_{VD6282}=93.61\%$) on the totality of the acquisitions.

MRE SpO _{2R/G}	I_{norm}		ε_{Hb} and ε_{HbO2}	
	VD6281 (%)	VD6282 (%)	VD6281 (%)	VD6282 (%)
Average	23.37	14.80	8.33	5.39
RMS	28.17	18.22	9.25	6.08
max	63.96	38.85	20.96	11.56
min	3.19	1.24	3.07	1.73

Table 7.5: Range of the MRE for the two interpolation methods, considering the final results of both the sensors.

ACC SpO _{2R/G}	I_{norm}		ε_{Hb} and ε_{HbO2}	
	VD6281 (%)	VD6282 (%)	VD6281 (%)	VD6282 (%)
Average	77.13	83.38	91.93	94.61
RMS	78.49	83.92	92.02	94.65
max	96.81	94.02	97.89	98.27
min	43.54	61.15	79.04	88.44

Table 7.6: Range of the ACC for the two interpolation methods, considering the final results of both the sensors.

The SpO₂, obtained from the extinction coefficient relation, does not return trustworthy value, also after the offset correction. This aspect will be recalled in the conclusion part of the present work.

7.2.2 Regression Analysis

By means of the regression analysis, the two sensors were calibrated. The SpO₂ was obtained by the interpolation of the R values and the Onyx SpO₂.

A scatter plot was extrapolated, by setting the R ratio on the x-axis and the Onyx SpO₂ on the y-axis. Observing the disposition of the data in the Cartesian Plane, the **linear** and **quadratic** relations were extracted for each signals. The final used x^2 , x and q coefficients, to compute the Rainbow SpO₂, were their average values.

The operation was done both for the VD6281 and the VD6282.

Furthermore, the regression method is independent from the extinction coefficients, because it depends only from the R value that is the ratio of the DC and AC components, of the green and red signals.

VD6281

The linear and quadratic relations, obtained from the regression analysis, are reported for the VD6281:

QUADRATIC	x2	x1	q	LINEAR	x1	q
Trial1	81	-77	120		6.1	94
Trial2	-250	210	52		5.6	95
Trial3	-3.4	4.8	97		0.89	98
Trial4	640	-570	220		21	97
Trial5	-130	150	52		2.2	96
Trial6	180	-190	150		-0.86	99
Trial7	360	-380	200		-9.1	100
Trial8	-200	210	42		9	93
Trial9	33	-33	110		0,083	99
Trial10	1300	-1200	400		-0.84	97
Trial11	310	-380	220		-0.82	98
Trial12	-1.1	-2	99		-3.2	100
Trial13	-44	49	98		-1.1	98
Trial14	-17	22	91		1.5	97
Trial15	70	-77	120		-2.2	100
Average Coefficients	155,23	-150.88	138.07		1.8	97.4

Table 7.7: Regression relations resulting from the quadratic and linear interpolations between the R ratio and the Onyx SpO₂

In the present work, the linear relation between the R ratio and the Onyx SpO₂ did not able to follow all the saturation variations. Using the $x1$ and q coefficients, indeed, the SpO₂ trend was completely lost.

Therefore, the quadratic relation was chosen as the better correspondence between the R value and the Onyx SpO₂. The final quadratic equation utilized for the present study was:

$$SpO_2 = 155.23 \cdot R^2 - 150.88 \cdot R + 138.07 \quad (7.2)$$

Some resulting SpO₂ are subsequently reported, together with their scatter plot.

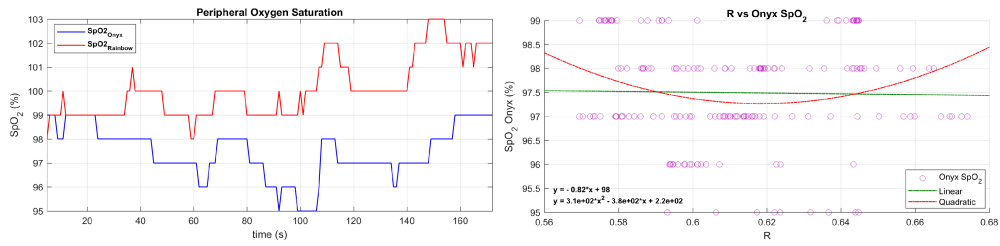


Figure 7.21: From left to right: the resulting SpO₂ and the relative scatter plot are reported

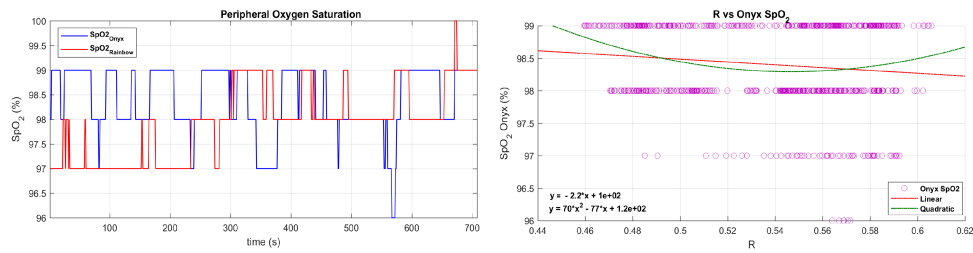


Figure 7.22: From left to right: the resulting SpO₂ and the relative scatter plot are reported

The MRE and the ACC computed for the 15 trials are reported, for the SpO₂ resulting from the quadratic regression interpolation.

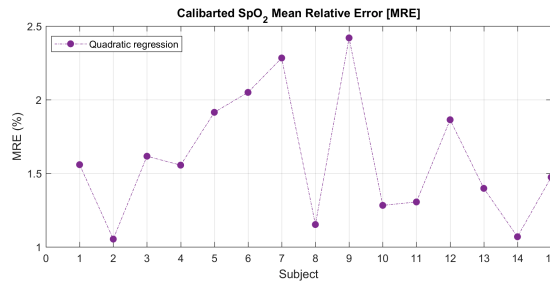


Figure 7.23: MRE of the SpO₂ estimations, using the quadratic regression interpolation.

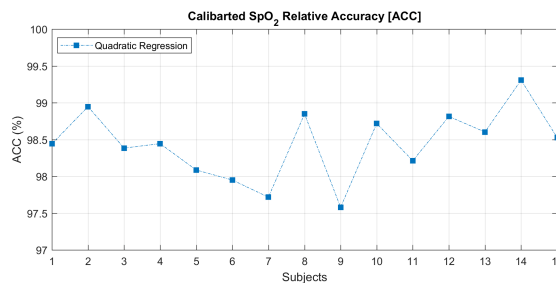


Figure 7.24: ACC of the SpO₂ estimations, using the quadratic regression interpolation.

The table with the MRE and ACC ranges is reported:

VD6281 SpO _{2R/G}	MRE (%)	ACC (%)
Average	1.32	98.76
RMS	1.65	95.07
max	2.74	99.61
min	0.58	97.26

Table 7.8: MRE and ACC range for the VD6281

Some ranges of the obtained SpO₂ values, implementing the regression analysis, are reported in the table below.

Rainbow									
Max	98	97	104	98	97	98	97	97	99
Min	97	96	96	96	96.27	96	96	96	96
Mean	97.14	96.69	98.51	96.92	96.27	96.86	96.52	96.71	97.5
Onyx									
Max	99	99	98	100	100	99	99	98	99
Min	93	94	94	98	96	95	98	90	96
Mean	97.41	97.81	97.12	99	98.69	97.77	98.98	96.54	98.4

Table 7.9: SpO₂ ranges for the VD6281, compared with the respective Onyx values.

VD6282

The linear and quadratic relations, obtained from the regression analysis, are reported for the VD6282 in table 7.10. Also in this case, the quadratic relation better approximates the SpO₂ values.

The IR SpO₂ is reported to compare the final SpO₂ with the one obtained with the red and green wavelengths.

QUADRATIC	x2	x1	q	LINEAR	x1	q
Trial1	230	-370	250		-3.6	100
Trial2	-0.15	7.1	92		6.9	92
Trial3	390	-590	320		-7.3	100
Trial4	-75	110	60		0.8	98
Trial5	-2.6	4.6	96		0.58	98
Trial6	-200	290	-4,2		-12	110
Trial7	240	-370	240		-13	110
Tria8	220	-340	230		-105	99
Trial9	-120	190	21		5.5	93
Average Coefficients	75.80	-118.7	144.97		-14.124444	100

Table 7.10: Regression relations resulting from the quadratic and linear interpolations between the R ratio and the Onyx SpO₂

The final quadratic equation utilized for the present study was:

$$SpO_2 = 75.80 \cdot R^2 - 118.7 \cdot R + 144.97 \quad (7.3)$$

The SpO₂ trend is reported below, for the same signal in Red/Green λ and Red/IR λ :

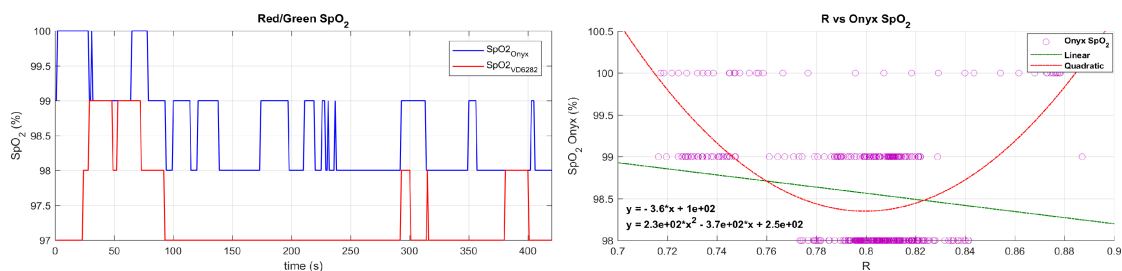


Figure 7.25: From left to right: the resulting SpO₂ and the relative scatter plot are reported

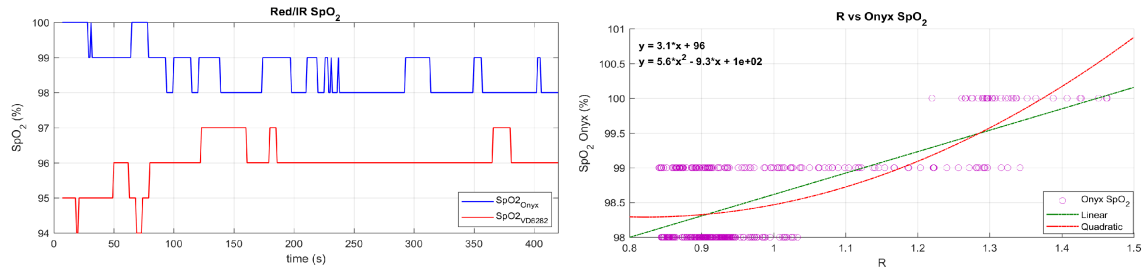


Figure 7.26: From left to right: the resulting SpO₂ and the relative scatter plot are reported

In figure 7.26, the SpO₂, resulting from the regression analysis at the red and IR, is reported. As it is shown, the SpO₂ / R relation has more linear than the Red-Green case.

The MRE and the ACC computed for the 9 trials are reported, for the SpO₂ resulting from the quadratic regression interpolation.

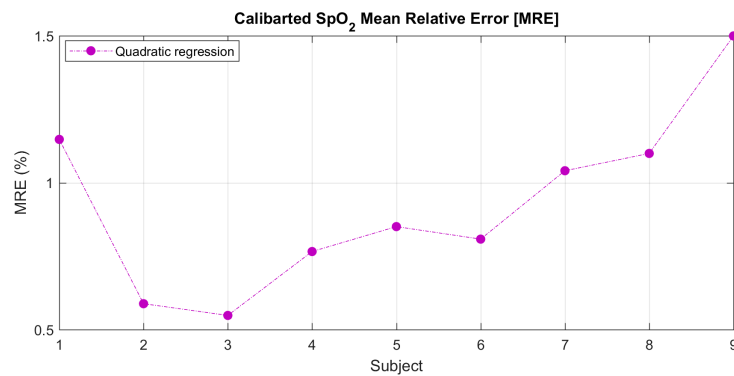


Figure 7.27: MRE of the SpO₂ estimations, using the quadratic regression interpolation.

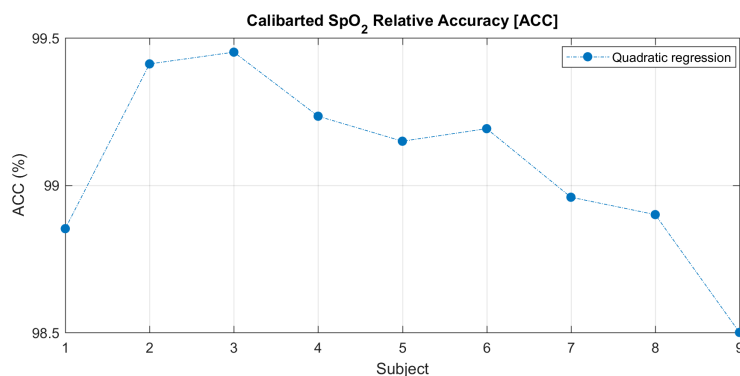


Figure 7.28: ACC of the SpO₂ estimations, using the quadratic regression interpolation.

The resulting MRE and ACC ranges are reported below:

VD6282 SpO _{2R/G}	MRE (%)	ACC (%)
Average	0.92	99.07
RMS	0.97	99.1
max	1.49	99.45
min	0.55	98.50

Table 7.11: MRE and ACC ranges for the VD6282.

Some ranges of the obtained SpO₂ values, implementing the regression analysis, are reported in the table below.

Rainbow					
Max	100	101	102	99	99
Min	98	98	98	98	98
Mean	98.25	98.59	98.38	98.45	98.41
Onyx					
Max	100	99	100	100	94
Min	98	97	97	94	98
Mean	98.56	98.29	99.22	98.79	97.14

Table 7.12: SpO₂ ranges for the VD6281, compared with the respective Onyx values.

Chapter 8

HR Measurements

The HR assessment is realized by the comparison between the HR computed by the algorithm and the HR acquired by the reference device, the Onyx 9560.

The HR was estimated considering:

- peaks and minimums detected from the red and green PPG (for the VD6281);
- peaks and minimums detected from the red, green and IR PPG (for the VD6282).

In this way, the best performance was chosen to compute the final HR.

The HR are reported, comparing the different trends obtained with the red, green and IR. Moreover, also the Sensitivity and PPV are reported, to evaluate the peaks and minimums detection algorithm performances.

VD6281

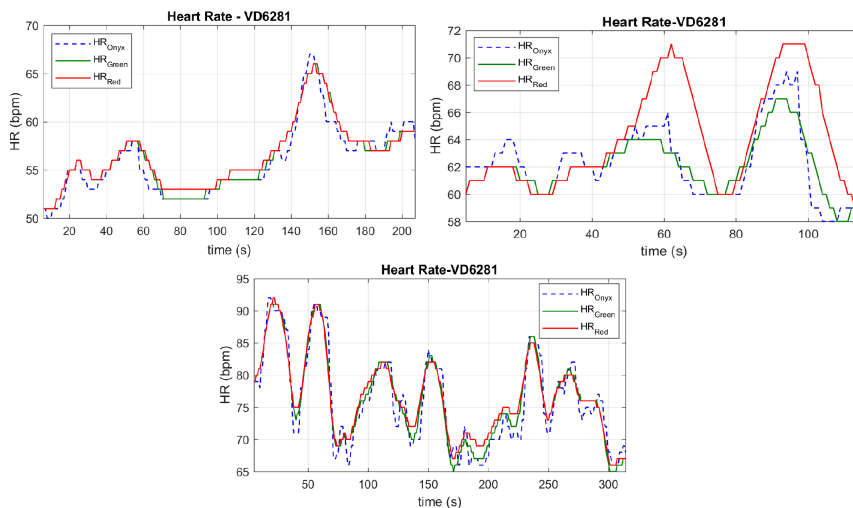


Figure 8.1: HR comparison: three different trials are reported, acquired from the red and green channel.

The HR estimated from the green PPG better approximates the actual value of the heart rate than the one from the red PPG. It is explained by the subsequent parameters. The MRE and ACC are reported for the red and green PPG.

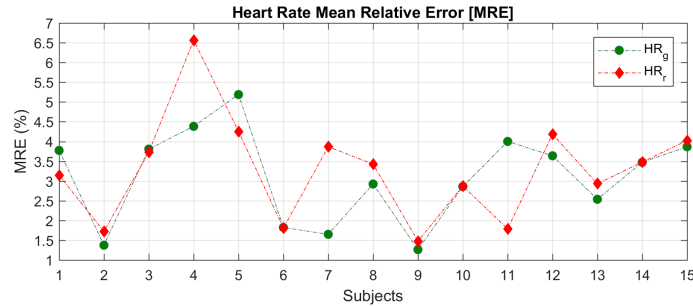


Figure 8.2: MRE of the HR estimations, computed on the 15 trials, considering the red and green channels.

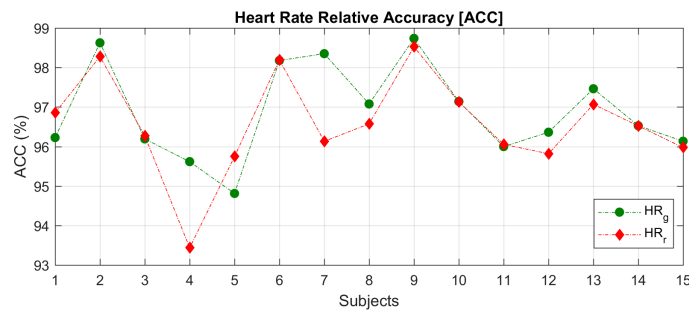


Figure 8.3: ACC of the HR estimations, computed on the 15 trials, considering the red and green channels.

In the table below, the range of the MRE and ACC are also reported.

	MRE (%)		ACC (%)	
	HR _g	HR _r	HR _g	HR _r
Average	3.10	3.29	96.90	96.57
RMS	3.30	3.52	96.9	95.97
max	5.19	6.57	98.74	98.5
min	1.26	1.48	94.81	93.44

Table 8.1: Range of the MRE and ACC, considering all the analyzed trials.

The green channel returns the best performances, in terms of average MRE (3,10 %) and ACC (96%) on the total trials.

Finally, the sensitivity and the PPV of the minimums and peaks detection are reported.

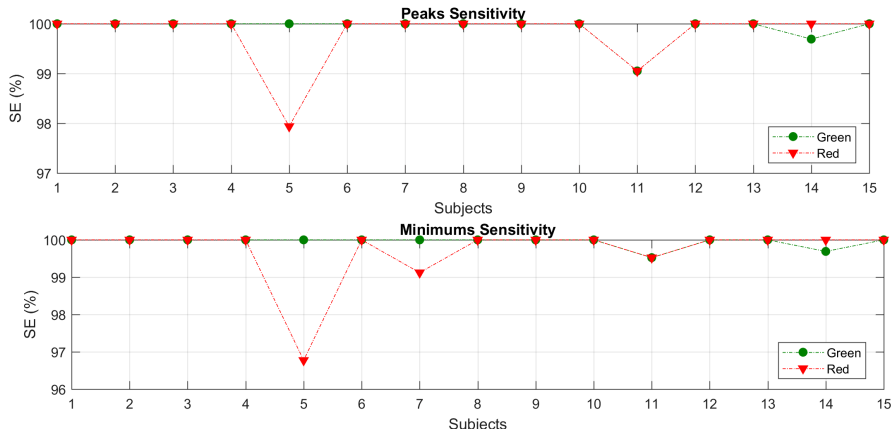


Figure 8.4: HR sensitivity for the red and green PPG.

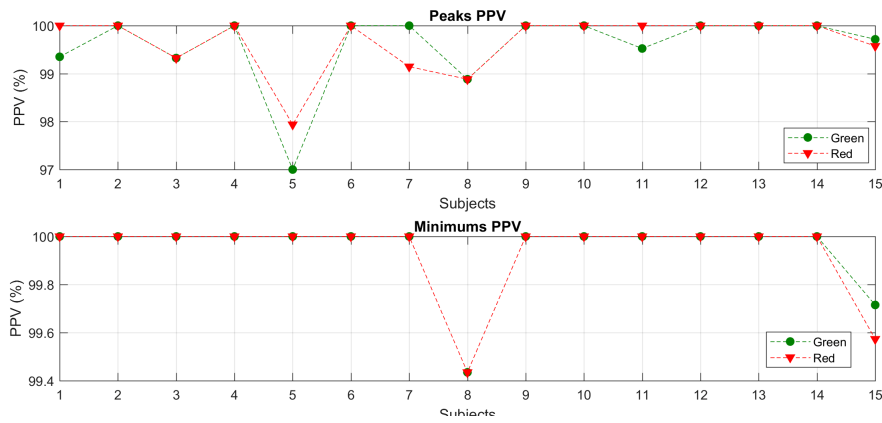


Figure 8.5: HR PPV for the red and green PPG.

VD6282

The same parameters were evaluated for the VD6282. They are reported below.

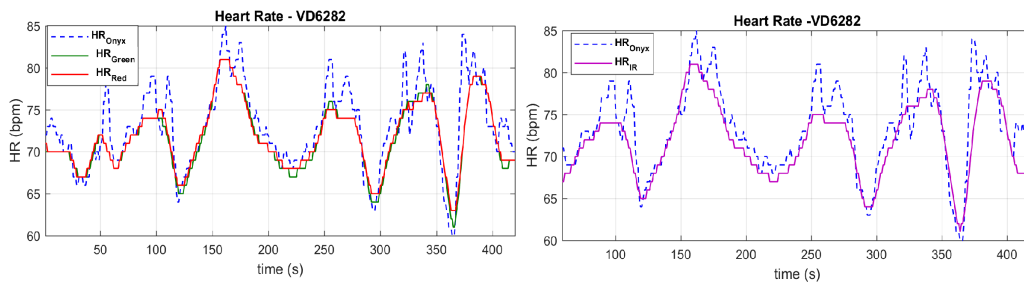


Figure 8.6: HR comparison: on the left the HR detected from the red and green PPG. On the right, the HR detected from the IR channel.

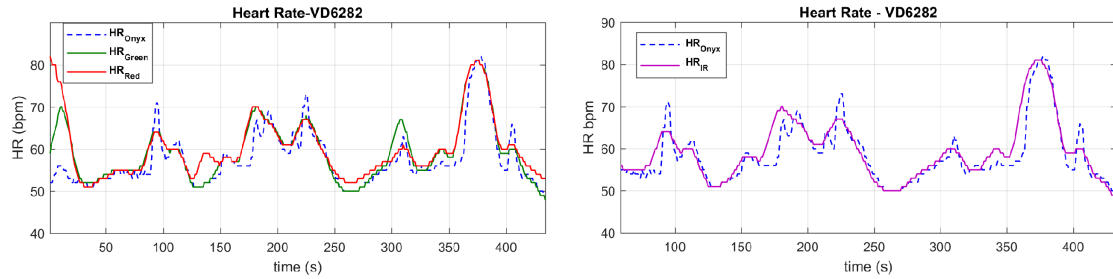


Figure 8.7: HR comparison: on the left the HR detected from the red and green PPG. On the right, the HR detected from the IR channel.

The MRE and ACC are reported for the red, green and IR PPG.

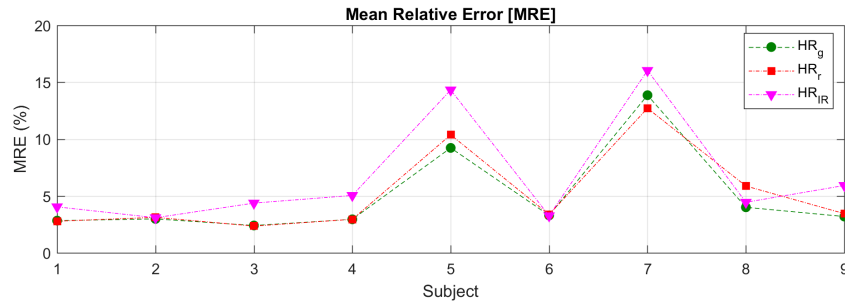


Figure 8.8: MRE of the HR estimations, computed on the 9 trials, considering the red, green and IR channels.

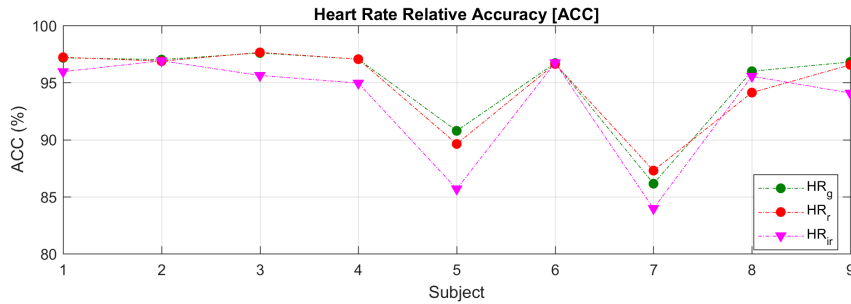


Figure 8.9: ACC of the HR estimations, computed on the 9 trials, considering the red, green and IR channels.

In the table below, the range of the MRE and ACC are also reported.

	MRE (%)			ACC (%)		
	HR_g	HR_r	HR_{IR}	HR_g	HR_r	HR_{IR}
Average	4.97	5.22	6.73	95.03	94.78	93.27
RMS	6.2	6.32	8.16	95.1	94.84	93.38
max	13.86	12.72	16.04	97.59	97.64	96.91
min	2.41	2.36	3.09	86.14	87.28	83.96

Table 8.2: Range of the MRE and ACC, considering all the analyzed trials.

As for the previous case, the green channel presents the best performances in terms of the average MRE (4.9 %) and ACC (95.02%) on the total trials considered.

The sensitivity and the PPV of the minimums and peaks detection are reported.

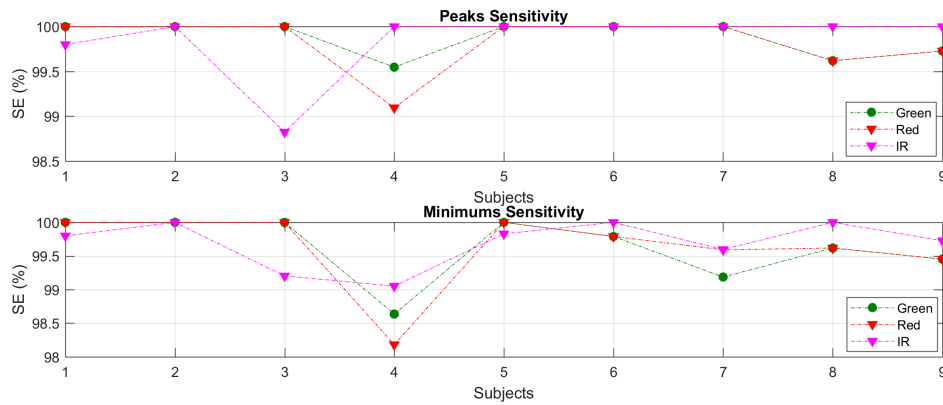


Figure 8.10: HR sensitivity for the red, green and IR PPG.

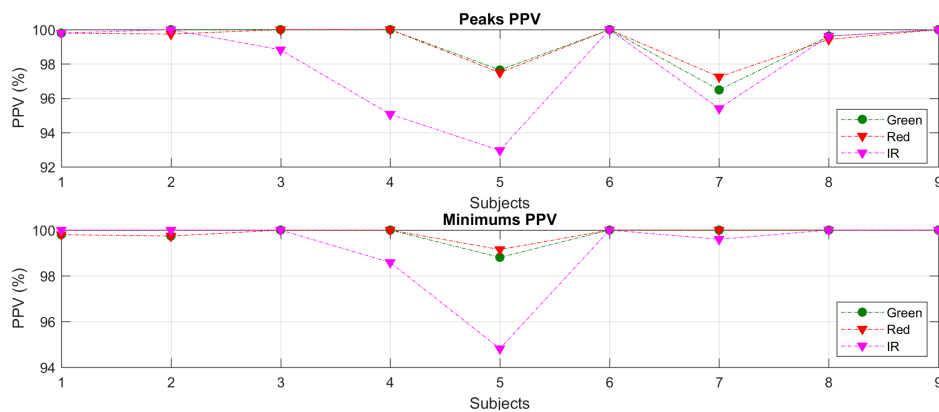


Figure 8.11: HR PPV for the red, green and IR PPG.

Part IV

Conclusions & Future Works

The present thesis describes the developing of a reflective prototype pulse oximeter. The final system is composed of the white LED and the multispectral sensor (the VD6281 before and the VD6282 later).

The innovation of the application is the simplification of the pulse oximeter hardware. Typically, indeed, the pulse oximeter is realized with two LEDs (i.e. red and IR).

Furthermore, thanks to the sensor size, the Rainbow is realized also for wearable application, in future prospective.

The first analysed item was the wavelength selection. In standard pulse oximeter, red and IR wavelengths are chosen because the light arrives at enough depth in tissues, to perceive the peripheral blood variations. However, at these wavelengths they are more sensitive to the motion artifact [28].

The green wavelength was considered as a good alternative to the IR one, as it is more motion resistant [28]. Moreover, the green wavelength is absorbed quickly on the surface, thus the PPG signal is less affected by the scattering effects of the surrounding tissues. On the other hand, the green signal has less information respect the IR ones.

The extinction coefficients are subsequently determined. The choice to compute the effective extinction coefficients was effectuated to consider the total optical information contained in the utilized component, given their real spectral responses.

As show in tables 7.1 and 7.2 (for the I_{norm} interpolation method) and in tables 7.3 and 7.4 (for the hemoglobin spectra interpolation method), the resulting coefficients are very different from each other, considering the ϵ_{Hb} and ϵ_{HbO_2} pairs, at the green and red wavelengths.

The SpO_2 , obtained with the Lambert-Beer approach, initially presents a constant offset from the real SpO_2 acquisition. The reason of the data offset is probably due to the overestimation introduced with the considered ϵ , at the wavelengths contained in the spectral responses of the utilized optical elements. Furthermore, the interpolation of the extinction coefficients introduced additional error on the final considered ϵ .

The higher MRE of the I_{norm} interpolation, reported in table 7.5 (i.e. **VD6281**=23.37% and **VD6282**=14.80%), is due to the larger number of wavelengths considered with this approach, consequence of the higher offset introduced at the final values (i.e. **VD6281**=181 and **VD6282**=208).

The hemoglobin spectra interpolation method instead, returns in SpO_2 values with an MRE relatively lower (i.e. **VD6281**=8.33% and **VD6282**=5.39%), because less $\epsilon(\lambda)$ are extracted and a more precise information about the optical elements are considered, taking in consideration not interpolated values of the normalized spectral responses. The offset introduced in this case, indeed, is lower than the previous one (i.e. **VD6281**=93.93 and **VD6282**=103).

Using the regression analysis, the final obtained SpO₂ is more similar to the Onyx SpO₂ trend. In this case, indeed, the measures are not influenced by the experimental extinction coefficients but only to the signal features, depending from the R ratio. While the linear regression interpolation does not follow all the SpO₂ variation, the quadratic one better performs the real parameter evolution. The resulting MRE of the sensor is lower than the Lambert-Beer method (i.e. **VD6281**=1.32% and **VD6282**=0.76) and also the ACC returns in good percentage values (i.e. **VD6281**=98.76% and **VD6282**=99.07%). The ranges of some of the SpO₂ obtained with the regression analysis is reported in tables 7.9 and 7.12. From these values, it can be noticed that the resulting SpO₂ has similar ranges, in terms of mean values assumed by the parameter. The VD6282 sensor version presents better performances, considering the reference Onyx SpO₂ ranges for the same signals.

The final accuracy rating, in terms of root mean square, is estimated for the regression analysis from the **VD6281** and **VD6282** errors. They are of about 2% for the VD6281 and of about 1% for the VD6282. These values are promising for the future development application of the sensor.

The HR returns good algorithm performances for both the sensors, as can be seen in tables 8.1 and 8.2. Comparing the green, red and IR performances, the MRE and the ACC of the green PPG is the lowest and the highest respectively, for both the sensor (i.e. **VD6281**: MRE_g=3.10% and ACC_g=97%; **VD6282**: MRE_g=4.97% and ACC_g=95.03%). The best performances are reported also for the peaks detection. Considering the graph 8.4 and 8.11, the green channel presents the best values for the PPV and the SE.

The future development for the present work are:

- improve the performances of the extinction coefficients evaluation, to obtain physiological value of SpO₂, using the Lambert-Beer equation;
- compare the Rainbow performances by means of spectrometers measurements, using the CO-oximeter as reference, the standard device utilized for the pulse oximeter calibration;
- exploit the multispectral characteristics of the Rainbow sensor to compute all the hemoglobin concentration in the blood (i.e. metHb and COHb);
- improve the sensitivity of the sensor for lower saturation level;
- improve the algorithm performances, specifically the peaks and minimums detection, considering also motion situation;

Bibliography

- [1] M. Abo-Zahhad, S. M. Ahmed, and O. Elnahas, "A wireless emergency telemedicine system for patients monitoring and diagnosis," *International journal of telemedicine and applications*, vol. 2014, p. 4, 2014.
- [2] O. Albahri, A. Albahri, K. Mohammed, A. Zaidan, B. Zaidan, M. Hashim, and O. H. Salman, "Systematic review of real-time remote health monitoring system in triage and priority-based sensor technology: Taxonomy, open challenges, motivation and recommendations," *Journal of medical systems*, vol. 42, no. 5, p. 80, 2018.
- [3] Y. Mendelson, "Pulse oximetry: theory and applications for noninvasive monitoring." *Clinical chemistry*, vol. 38, no. 9, pp. 1601–1607, 1992.
- [4] J. G. Webster, *Encyclopedia of medical devices and instrumentation*. John Wiley & Sons, Inc., 1990.
- [5] S. Palanivel Rajan, "Review and investigations on future research directions of mobile based telecare system for cardiac surveillance," *Journal of applied research and technology*, vol. 13, no. 4, pp. 454–460, 2015.
- [6] M. C. Suman and K. Prathyusha, "Wireless ecg system based on arm lpc 2103 processor," *International Journal of Electronics and Communication Technology*, vol. 3, pp. 115–119, 2012.
- [7] J. O'Donoghue and J. Herbert, "Profile based sensor data acquisition in a ubiquitous medical environment," in *Fourth Annual IEEE International Conference on Pervasive Computing and Communications Workshops (PERCOMW'06)*. IEEE, 2006, pp. 5–pp.
- [8] J. Kumekawa, "Emerging trends in telehealth," *Business briefing: Next generation healthcare*, pp. 62–64, 2000.
- [9] S. A. CLARK, "Normal oxygen transport," *Design of Pulse Oximeters*, pp. 13–20, 1997.

- [10] D. G. G. W. D. M. Pignocchino, "L'organizzazione dell'apparato cardiovascolare," *La nuova biologia.blu, il corpo umano plus*, 2016.
- [11] G. I. f. Q. Cologne and E. in Health Care (IQWiG), "How does the blood circulatory system work?" *InformedHealth.org [Internet]*, 2019.
- [12] B. the learning App. (2019) Human circulatory system. [Online]. Available: <https://byjus.com/biology/human-circulatory-system-transportation/>
- [13] D. G. G. W. D. M. Pignocchino, "Il ciclo cardiaco: il cuore si contrae ritmicamente e spontaneamente," *biologia.blu*, 2016.
- [14] B. G. S. Writer. (2018) What is a normal heart rate? [Online]. Available: <https://www.livescience.com/42081-normal-heart-rate.html>
- [15] H. C. H. M. R. B. David Sadava, David M. Hillis, "L'apparato respiratorio," *La nuova biologia.blu, il corpo umano plus*, 2016.
- [16] A. ScienceNetLinks. (2019) Mechanics of respiration. [Online]. Available: <http://sciencenetlinks.com/student-teacher-sheets/mechanics-respiration/>
- [17] Zanichelli, "Gli scambi gassosi," *Idee per insegnare la biologia*, 2012.
- [18] B. Den. (2019) Hemoglobin: Structure, function and its properties. [Online]. Available: <https://www.biochemden.com/hemoglobin/>
- [19] K. Minolta, "Basic understanding of the pulse oximeter. how to read spo2," *Konica Minolta Sensing, Inc. Ramsey*, 2006.
- [20] anupbiochemist@gmail.com. (2018) Oxyhemoglobin dissociation curve. [Online]. Available: <http://www.biosciencenotes.com/oxyhemoglobin-dissociation-curve/>
- [21] J. Allen, "Photoplethysmography and its application in clinical physiological measurement," *Physiological measurement*, vol. 28, no. 3, p. R1, 2007.
- [22] A. A. Alian and K. H. Shelley, "Photoplethysmography: Analysis of the pulse oximeter waveform," in *Monitoring technologies in acute care environments*. Springer, 2014, pp. 165–178.
- [23] A. Kamal, J. Harness, G. Irving, and A. Mearns, "Skin photoplethysmography a review," *Computer methods and programs in biomedicine*, vol. 28, no. 4, pp. 257–269, 1989.

- [24] P. Kyriacou, K. Budidha, and T. Y. Abay, “Optical techniques for blood and tissue oxygenation,” *Encyclopedia of Biomedical Engineering*, ed R. Narayan (Oxford: Elsevier), pp. 461–472, 2019.
- [25] J. Weinman, A. Hayat, and G. Raviv, “Reflection photoplethysmography of arterial-blood-volume pulses,” *Medical and Biological Engineering and Computing*, vol. 15, no. 1, pp. 22–31, 1977.
- [26] D. Clayton, R. Webb, A. Ralston, D. Duthie, and W. Runciman, “Pulse oximeter probes a comparison between finger, nose, ear and forehead probes under conditions of poor perfusion,” *Anaesthesia*, vol. 46, no. 4, pp. 260–265, 1991.
- [27] S. K. Longmore, G. Y. Lui, G. Naik, P. P. Breen, B. Jalaludin, and G. D. Gargiulo, “A comparison of reflective photoplethysmography for detection of heart rate, blood oxygen saturation, and respiration rate at various anatomical locations,” *Sensors*, vol. 19, no. 8, p. 1874, 2019.
- [28] S. Alharbi, S. Hu, D. Mulvaney, L. Barrett, L. Yan, P. Blanos, Y. Elsahar, and S. Adema, “Oxygen saturation measurements from green and orange illuminations of multi-wavelength optoelectronic patch sensors,” *Sensors*, vol. 19, no. 1, p. 118, 2019.
- [29] A. Gorczewska, “Influence of sensor design and optical properties of tissue on the photoplethysmographic signal,” 2015.
- [30] M. Van Gemert, S. L. Jacques, H. Sterenborg, and W. Star, “Skin optics,” *IEEE Transactions on biomedical engineering*, vol. 36, no. 12, pp. 1146–1154, 1989.
- [31] P. D. Mannheim, “The light–tissue interaction of pulse oximetry,” *Anesthesia & Analgesia*, vol. 105, no. 6, pp. S10–S17, 2007.
- [32] G. Joseph, A. Joseph, G. Titus, R. M. Thomas, and D. Jose, “Photoplethysmogram (ppg) signal analysis and wavelet de-noising,” *2014 Annual International Conference on Emerging Research Areas: Magnetics, Machines and Drives (AICERA/iCMMD)*, pp. 1–5, 2014.
- [33] R. Sahni, “Noninvasive monitoring by photoplethysmography,” *Clinics in perinatology*, vol. 39, no. 3, pp. 573–583, 2012.
- [34] A. A. Kamshilin and N. B. Margaryants, “Origin of photoplethysmographic waveform at green light,” *Physics Procedia*, vol. 86, pp. 72–80, 2017.
- [35] P. M. Middleton, C. H. Tang, G. S. Chan, S. Bishop, A. V. Savkin, and N. H. Lovell, “Peripheral photoplethysmography variability analysis of sepsis patients,” *Medical & biological engineering & computing*, vol. 49, no. 3, pp. 337–347, 2011.

- [36] R. Gupta, S. Ahluwalia, and S. Randhawa, "Design and development of pulse oximeter," in *Proceedings of the First Regional Conference, IEEE Engineering in Medicine and Biology Society and 14th Conference of the Biomedical Engineering Society of India. An International Meet.* IEEE, 1995, pp. 1–13.
- [37] T. Ysehak Abay, "Reflectance photoplethysmography for non-invasive monitoring of tissue perfusion," Ph.D. dissertation, City, University of London, 2016.
- [38] H. Harini, L. Krithika, M. Shalini, S. Swaminathan, and N. M. Mohan, "Design and implementation of a calibration-free pulse oximeter," in *The 15th International Conference on Biomedical Engineering.* Springer, 2014, pp. 100–103.
- [39] G. Ma, W. Zhu, J. Zhong, T. Tong, J. Zhang, and L. Wang, "Wearable ear blood oxygen saturation and pulse measurement system based on ppg," in *2018 IEEE SmartWorld, Ubiquitous Intelligence & Computing, Advanced & Trusted Computing, Scalable Computing & Communications, Cloud & Big Data Computing, Internet of People and Smart City Innovation (SmartWorld/SCALCOM/UIC/ATC/CB-DCOM/IOP/SCI).* IEEE, 2018, pp. 111–116.
- [40] D. N. Townsend, "Pulse oximetry," *Medical Electronics*, pp. 42–54, 2001.
- [41] C. M. Alexander, L. E. Teller, and J. B. Gross, "Principles of pulse oximetry: theoretical and practical considerations," *Anesthesia & Analgesia*, vol. 68, no. 3, pp. 368–376, 1989.
- [42] D. J. Sebald, "Motivation of pulse oximetry," in *Design of Pulse Oximeters.* CRC Press, 1997, pp. 26–33.
- [43] S. M. Kennedy, "An introduction to pulse oximeters: Equations and theory," *University of Wisconsin-Madison*, vol. 20, 2015.
- [44] O. Wieben, "Light absorbance in pulse oximetry," in *Design of pulse oximeters.* CRC Press, 1997, pp. 53–68.
- [45] G. Zonios, U. Shankar, and V. K. Iyer, "Pulse oximetry theory and calibration for low saturations," *IEEE Transactions on biomedical engineering*, vol. 51, no. 5, pp. 818–822, 2004.
- [46] G. Mook, O. van Assendelft, and W. Zijlstra, "Wavelength dependency of the spectrophotometric determination of blood oxygen saturation," *Clinica chimica acta*, vol. 26, no. 1, pp. 170–173, 1969.

- [47] A. Shepherd, J. Kiel, and G. Riedel, "Evaluation of light-emitting diodes for whole blood oximetry," *IEEE transactions on biomedical engineering*, no. 11, pp. 723–725, 1984.
- [48] U. o. P. Research Centre E. Piaggio. (2019) Proprieta' fisiche dei tessuti. [Online]. Available: <http://www.centropiaggio.unipi.it/sites/default/files/course/material/3.pdf>
- [49] Z. Xiong and B. S. Kodali, *Pulse oximetry and capnography*. Cambridge University Press, 2011, pp. 186–190.
- [50] A. Bashkatov, E. Genina, V. Kochubey, and V. Tuchin, "Optical properties of human skin, subcutaneous and mucous tissues in the wavelength range from 400 to 2000 nm," *Journal of Physics D: Applied Physics*, vol. 38, no. 15, p. 2543, 2005.
- [51] Y. Maeda, M. Sekine, and T. Tamura, "The advantages of wearable green reflected photoplethysmography," *Journal of medical systems*, vol. 35, no. 5, pp. 829–834, 2011.
- [52] E. D. Chan, M. M. Chan, and M. M. Chan, "Pulse oximetry: understanding its basic principles facilitates appreciation of its limitations," *Respiratory medicine*, vol. 107, no. 6, pp. 789–799, 2013.
- [53] V. Vizbara, "Comparison of green, blue and infrared light in wrist and forehead photoplethysmography," *BIOMEDICAL ENGINEERING 2016*, vol. 17, no. 1, 2013.
- [54] E. Thimsen, B. Sadtler, and M. Y. Berezin, "Shortwave-infrared (swir) emitters for biological imaging: a review of challenges and opportunities," *Nanophotonics*, vol. 6, no. 5, pp. 1043–1054, 2017.
- [55] P. D. Mannheimer, J. Cascini, M. E. Fein, and S. L. Nierlich, "Wavelength selection for low-saturation pulse oximetry," *IEEE transactions on biomedical engineering*, vol. 44, no. 3, pp. 148–158, 1997.
- [56] J. De Kock, K. Reynolds, L. Tarassenko, and J. Moyles, "The effect of varying led intensity on pulse oximeter accuracy," *Journal of medical engineering & technology*, vol. 15, no. 3, pp. 111–115, 1991.
- [57] F. Lorenzelli, "Principi di saturimetria e funzionamento del pulsossimetro," Ph.D. dissertation, Alma Mater Studiorum Universita' di Bologna, 2017.
- [58] O. Yossef Hay, M. Cohen, I. Nitzan, Y. Kasirer, S. Shahroor-karni, Y. Yitzhaky, S. Engelberg, and M. Nitzan, "Pulse oximetry with two infrared wavelengths without calibration in extracted arterial blood," *Sensors*, vol. 18, no. 10, p. 3457, 2018.

- [59] M. Nitzan, A. Romem, and R. Koppel, "Pulse oximetry: fundamentals and technology update," *Medical Devices (Auckland, NZ)*, vol. 7, p. 231, 2014.
- [60] S. L. Christian Baumgartner, Theresa Rienmüller. (2019) Biomedical sensor systems: Laboratory. [Online]. Available: https://www.tugraz.at/fileadmin/user_upload/Institute/HCE/Pulse_Oximetry.pdf
- [61] J. S. Schowalter, "Calibration," in *Design of pulse oximeters*. CRC Press, 1997, pp. 172–188.
- [62] M. Nitzan, S. Noach, E. Tobal, Y. Adar, Y. Miller, E. Shalom, and S. Engelberg, "Calibration free pulse oximetry based on two wavelengths in the infrared a preliminary study," *Sensors*, vol. 14, no. 4, pp. 7420–7434, 2014.
- [63] S. Chugh and J. Kaur, "Low cost calibration free pulse oximeter," in *2015 Annual IEEE India Conference (INDICON)*. IEEE, 2015, pp. 1–5.
- [64] Amperordirect. (2019) What is perfusion index (pi). [Online]. Available: <https://www.amperordirect.com/pc/help-pulse-oximeter/z-what-is-pi.html>
- [65] Masimo. (2019) Masimo signal extraction technology. [Online]. Available: <https://www.masimo.com/technology/co-oximetry/set/>
- [66] ——. (2019) Pvi. [Online]. Available: <http://www.masimo.com/technology/co-oximetry/pvi/>
- [67] P. S. Addison, J. N. Watson, M. L. Mestek, J. P. Ochs, A. A. Uribe, and S. D. Bergese, "Pulse oximetry-derived respiratory rate in general care floor patients," *Journal of clinical monitoring and computing*, vol. 29, no. 1, pp. 113–120, 2015.
- [68] D. A. Ayres, "Pulse oximetry and co-oximetry," *Advanced monitoring and procedures for small animal emergency and critical care*, pp. 274–285, 2012.
- [69] E. Mack, "Co-oximetry," *Pediatrics in review*, vol. 28, no. 2, pp. 73–4, 2007.
- [70] R. S. H. A. Stolbach, "Respiratory principles," in *TOXICOLOGIC EMERGENCIES*. Mc Graw Hill education, ch. 21.
- [71] lifebox. (2019) Handheld pulse oximeter model: Ahmx. [Online]. Available: http://lifebox.org/wp-content/uploads/lifebox_pulse_oximeter_specifications2.pdf
- [72] Masimo. (2019) Mightysat rx fingertip pulse oximeter. [Online]. Available: <https://www.masimo.com/products/monitors/spot-check/mightysatrx/>

- [73] Nonin. (2019) Wristox2 model 3150 with usb wrist - worn pulse oximeter. [Online]. Available: <https://www.nonin.com/products/3150-usb/>
- [74] N. Shah, H. B. Ragaswamy, K. Govindugari, and L. Estanol, "Performance of three new-generation pulse oximeters during motion and low perfusion in volunteers," *Journal of clinical anesthesia*, vol. 24, no. 5, pp. 385–391, 2012.
- [75] V. medical. (2019) Vyntus walk mobile exercise testing. [Online]. Available: <https://intl.vyaire.com/products/vyntus-walk-mobile-exercise-testing>
- [76] Nonin. (2019) Onyx ii 9550 military fingertip pulse oximeter. [Online]. Available: <https://www.nonin.com/products/9550/>
- [77] Philips. (2019) Pulse oximeter. [Online]. Available: <https://www.usa.philips.com/healthcare/solutions/breathing-and-respiratory-care/pulse-oximetry>
- [78] ——. (2019) Wristox2 wrist-worn pulse oximeter. [Online]. Available: <https://www.usa.philips.com/healthcare/product/HC1078606/wrist0x2-pulse-oximeter>
- [79] Garmin. (2019) fenix 5x plus. [Online]. Available: <https://www.garmin.co.in/products/wearables/fenix-5x-plus-black/>
- [80] ——. (2019) Pulse oximeter technology. [Online]. Available: <https://www.garmin.co.in/garmin-technology/pulse-ox/>
- [81] G. R. reports. (2018) Pulse oximeters market size, share and trends analysis report by type (fingertip, handheld), by end use (hospitals and healthcare facilities, homecare), by region, and segment forecasts, 2019 - 2025. [Online]. Available: <https://www.grandviewresearch.com/industry-analysis/pulse-oximeter-market>
- [82] W. Zijlstra, A. Buursma, and W. Meeuwssen-Van der Roest, "Absorption spectra of human fetal and adult oxyhemoglobin, de-oxyhemoglobin, carboxyhemoglobin, and methemoglobin." *Clinical chemistry*, vol. 37, no. 9, pp. 1633–1638, 1991.
- [83] S. Prahl. (1998) Tabulated molar extinction coefficient for hemoglobin in water. [Online]. Available: <https://omlc.org/spectra/hemoglobin/summary.html>
- [84] Wikipedia. (2019) Finite impulse response. [Online]. Available: https://it.wikipedia.org/wiki/Finite_impulse_response